# MINIATURIZED FIBER MODAL INTERFEROMETERS AND THEIR APPLICATIONS AS FIBER SENSORS

**DONG BO**

**NATIONAL UNIVERSITY OF SINGAPORE**
**2015**

# MINIATURIZED FIBER MODAL INTERFEROMETERS AND THEIR APPLICATIONS AS FIBER SENSORS

**DONG BO**
(*Ph.D,Nankai University,China*)

**A THESIS SUBMITTED**
**FOR THE DEGREE OF DOCTOR OF PHILOSOPHY**

**DEPARTMENT OF ELECTRICAL AND**
**COMPUTER ENGINEERING**
**NATIONAL UNIVERSITY OF SINGAPORE**

**2015**

# DECLARATION

I hereby declare that the thesis is my original work and it has been written by me in its entirety. I have duly acknowledged all the sources of information which have been used in the thesis.

This thesis has also not been submitted for any degree in any university previously.

**DONG BO**
**3 August 2015**

# Acknowledgements

First of all, I would like to express my greatest gratitude to my supervisor Prof. Yu Changyuan for his invaluable guidance and kind support throughout my Ph.D study. His broad knowledge and clear thought inspired me; his patient guidance and continuous encouragement drove me. Without his supervision and constant help, this dissertation would not have been possible.

It is a wonderful experience to reenter the university to learn novel knowledge from my supervisor and his group members. Many thanks to fellow researchers Dr. Yu Yi, Dr. Hu Qikai, Dr.Wang Qian, Dr. Liu Huanghuang, Dr. Xu Zhuoran, Dr. Zhou Jingjing, Dr.Li Xiang, Dr.ZhaoYunshan, and many others for their help in my research and study.

I would like to thank the colleagues and students from Institute for Infocomm Research, National university of Singapore, and Nanyang Technological Univeristy who have helped me both in study and life in Singapore, including Dr. Wang Yixin, Dr. Gong Yandong, Dr.Xu Zhaowen, Dr.Yang Xiufeng, Dr.Huang Qirui, Dr.Sun Ying, Dr. Cao Shengjiao, Dr. Zhang Banghong, Mr.Ng Junhong, Dr. Dong Hui, Dr.Hu Juanjuan, Dr. Chen Zhihao, Dr.Hao Jianzhong, Mr. Varghese Paulos, Dr Zhou Luying, Dr Cheng Xiaofei, Dr. Wu Min, Dr Cao Jianneng, Mr. Peng Yuqi, Ms. Ge Yao, Mr.Shen Zhanyu, and many others for their help in my research and life.

I would like to thank Prof. Nan-kuang Chen from National United University, Taiwan, for his providing us the tapered active fiber samples.

I would like to thank my closest friends for their emotional support.

Most of all, I am grateful to my wife, who always supports me in my life. I am very grateful to my parents-in-law who have helped me take care of my family.

Last but not least, I would like to express my sincere appreciation to my parents and my brother for their love and encouragement.

# Table of Contents

# Summary

Fiber in-line miniaturized modal interferometers (MMIs) have attracted much attention due to their inherent advantages, such as simple and compact structure, small size, low cost, and easy fabrication, especially, they have wide applications in fiber filters and fiber sensors. In this thesis, four types of MMIs, based on dual single mode fiber (SMF) down-tapers, dual SMF up-tapers, Er-Yb codoped phosphosilicate fiber (EYPF), and ethanol-filled photonic bandgap fiber (PBF), are proposed and demonstrated. Their applications as fiber sensors are investigated theoretically and experimentally. The main findings and contributions are summarized as follows:

Firstly, to address the limitations being in face of the current MMIs, especially, for the SMF based MMIs, such as low extinction ratio (ER) and poor fabrication reproducibility, two types of SMF based MMIs, with a high ER and good fabrication reproducibility, are proposed and demonstrated.

The first type is a high ER SMF based down-taper MMI. It can be fabricated by using an arc discharge method. It is sensitive to both temperature and ambient refractive index (RI). If adopting a fiber Bragg grating (FBG) as the temperature reference, simultaneous measurement of temperature and RI can be achieved, which shows a better performance than the other dual parameters measurement method.

The second type is a high ER dual cladding modes (DCMs) fiber up-taper MMI. It is almost like an LPG-type device, also with a deep resonance dip within C and L bands. It can be fabricated automatically by adopting a suitable “overlap” parameter of a commercial

splicer. Compared to the fiber down-taper MMI, this type of MMI is more robust since the fiber down-taper MMI is more fragile. As a fiber sensor, it can be used for temperature, strain, RI, micro-displacement, ultrasound, and dual parameters (strain and temperature) measurements with better performances.

Thirdly, the intensity and wavelength dependent thermal characteristics of the EYPF based down-taper MMI are investigated. Without an additional optical pump, it can be used as a high sensitivity temperature sensor. After introducing into the additional optical pump, its thermal sensitivity is reduced. This suggests that the introduced optical pump can be used to control its thermal sensitivity and improve its stability.

Fourthly, the fully and partially ethanol-filled PBF based MMIs and their applications as temperature sensors are investigated. Since the ethanol-filled PBFs can support more high order cladding modes, they are much easier to construct the core-cladding MMIs without using the other special splicing techniques. The effective RI difference between the core and cladding modes can be greatly improved. Moreover, the thermal sensitivity of the PBF based MMI can be greatly improved by filling the ethanol into the air core and/or air claddings of the PBF, and it can be adjusted by selectively filling the air core and/or air claddings of the PBF with ethanol.

# List of Figures

# List of Abbreviations

| | |
|---|---|
| BBS | Broadband Source |
| BPM | Beam Propagation Method |
| CCFC | Cured Carbon Fiber Composite |
| DBR | Distributed Bragg Reflector |
| DCF | Double Cladding Fiber |
| DCMs | Dual Cladding Modes |
| ER | Extinction Ratio |
| EYPF | Er-Yb Codoped Phosphosilicate Fiber |
| EDF | Er-Doped Fiber |
| FAS | Fiber Acoustic Sensor |
| FBG | Fiber Bragg Grating |
| FDTD | Finite-Difference-Time-Domain |
| FFT | Fast Fourier Transform |
| FPI | Fabry-Perot Interferometer |
| HCF | Hollow Core Fiber |
| HBFLM | High-Birefringence-Fiber Loop Mirror |
| LD | Laser Diode |
| LPG | Long Period Grating |
| MZI | Mach-Zehnder Interferometer |
| MCI | Michelson Interferometer |
| MDM | Mode Division Multiplexing |
| MMF | Multimode Fiber |
| MMI | Miniaturized Modal Interferometers |
| MFD | Mode Field Diameter |
| NA | Numerical Aperture |
| NDE | Non-Destructive Evaluation |

| | |
|---|---|
| OSA | Optical Spectrum Analyzer |
| OSC | Oscilloscope |
| PBF | Photonic Bandgap Fiber |
| PCF | Photonic Crystal Fiber |
| PMF | Polarization Maintaining Fiber |
| PMFLM | Polarization Maintaining Fiber Loop Mirror |
| PMPCF | Polarization Maintaining PCF |
| PD | Photo-Detector |
| PZT | Piezoelectric Transducers |
| RI | Refractive Index |
| SI | Sagnac Interferometer |
| SMF | Single Mode Fibers |
| SSB | Simple-Supported Beam |
| STCF | Suspended Twin Core Fiber |
| SEM | Scanning Electron Microscope |
| TCF | Thin Core Fiber |
| TIR | Total Internal Reflection |
| WDM | Wavelength Division Multiplexer |

# Chapter 1

# Introduction

## 1.1 Background

Fiber interferometer is the key device in fiber communication, fiber laser, and fiber sensor. In fiber communication, it is used as a fiber filter for optical signal processing. Connecting it in a fiber laser cavity, it is used to tune and select the laser frequency. Especially, it has wide applications in fiber sensing for the measurement of strain, temperature, vibration, displacement, bending, refractive index (RI), ultrasound, etc. The typical traditional fiber interferometers include Fabry-Perot interferometer (FPI), Mach-Zehnder interferometer (MZI), Michelson interferometer (MCI), and Sagnac interferometer (SI).

To construct an FPI, two parallel separated mirrors with a certain distance are required. The light is transmitted and reflected between the two mirrors

(Mirror 1 and 2) and construct multiple interferences, as shown in Figure 1.1. Its phase is dependent on the cavity length of the FPI. To obtain a high extinction ratio (ER) FPI, the mirrors need to be deposited high reflectivity films. The intensity of the output light can be given by

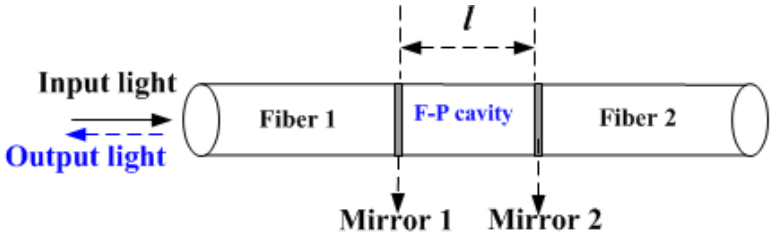


Figure 1.1 Schematic structure of the FPI

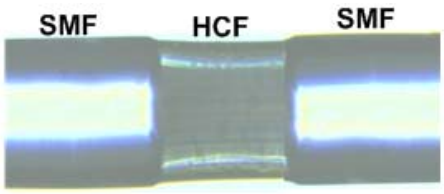


Figure 1.2 Photograph of the HCF based FPI [5]

$$I_{out} = I_{in} \frac{T^2}{(1-R)^2} \left[ \frac{1}{1 + FSin^2(\Delta\varphi/2)} \right] , \tag{1.1}$$

where $I_{in}$ and $I_{out}$ are the intensities of the input light and output light, $R$ and $T$ are the reflectivity and transmittivity of the mirror, $F = 4R/(1-R)^2$ is the fineness, and $\Delta\varphi$ is the phase difference between two adjacent light beams and it can be given by

$$\Delta\varphi = \frac{4\pi nl\cos\theta}{\lambda_0} , \tag{1.2}$$

where $n$ is the RI of the medium in the cavity, $l$ is the cavity length, $\theta$ is the refraction angle of the input light in the cavity, and $\lambda_0$ is the wavelength of the light in vacuum. Although the FPI can be constructed by sandwiching a short section of hollow core fiber (HCF) between two single mode fibers (SMFs) [1–10], but its ER is lower, as shown in Figure 1.2.

Figure 1.3 shows the schematic configuration of the MZI. The light illuminated by the laser is divided into two paths via the first 3-dB coupler. After the two-path light beams meet at the second 3-dB coupler, they re-couple with each other, then they are divided into two paths via the second 3-dB coupler, and detected by photo-detectors 1(PD1) and 2(PD2). As can be seen, it consists of two independent arms connected between two 3-dB fiber couplers. The interference occurs due to the re-coupling of the two separated light in the second coupler. Its phase is dependent on the length difference between the two arms. When it is used as a sensor, one arm is served as the sensing arm and the other one is used as the reference arm [10]. The light intensity detected by the PD1 and PD2 can be given by

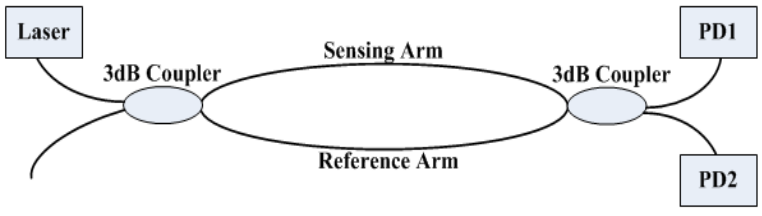


Figure 1.3 Schematic configuration of the MZI

$$I_1 = \frac{I_{in}}{2}(1+\alpha\cos\Delta\varphi), \tag{1.3}$$

$$I_2 = \frac{I_{in}}{2}(1-\alpha\cos\Delta\varphi), \tag{1.4}$$

where $I_{in}$ is the intensity of the input light, $I_1$ and $I_2$ are the intensities of the output light detected by PD1 and PD2, respectively; $\alpha$ is the coupling coefficient, $\Delta\varphi$ is the phase difference between the sensing arm and reference arm, and it can be expressed as

$$\Delta\varphi = \frac{2\pi n(l_1 - l_2)}{\lambda_0}, \tag{1.5}$$

where $n$ is the RI of the fiber core, and $l_1$ and $l_2$ are the lengths of the sensing arm and reference arm, respectively.

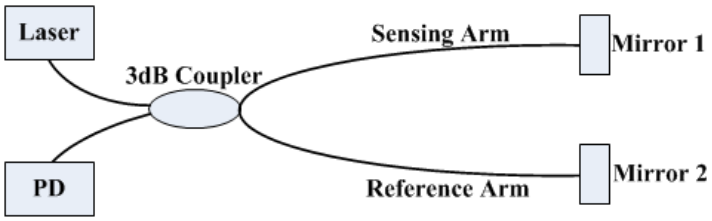


Figure 1.4 Schematic configuration of the MCI

Figure 1.4 shows the schematic configuration of the MCI. The principle of the MCI is similar to that of the MZI [11]. The main difference is that the MCI uses only one 3-dB coupler to separate and re-couple the reflected light by the two fiber end mirrors. The light intensity detected by the PD can be given by

$$I_{out} = I_{in}(1-\alpha\cos\Delta\varphi), \tag{1.6}$$

where $I_{in}$ and $I_{out}$ are the light intensities of the input light and output light, $\alpha$ is the coupling coefficient，$\Delta\varphi$ is the phase difference between the sensing arm and reference arm and it can be expressed as

$$\Delta\varphi = \frac{4\pi n(l_1 - l_2)}{\lambda_0}, \tag{1.7}$$

where $n$ is the RI of the fiber core, and $l_1$ and $l_2$ are the lengths of the sensing arm and reference arm, respectively.

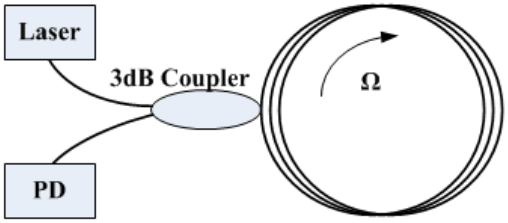


Figure 1.5 Schematic configuration of the SI

For the SI, it consists of a fiber loop with a 3dB coupler. The light is split into two counter-propagating beams via the same coupler, as show in Figure 1.5. For the SMF based SI, when the closed optical path keeps static, there is no optical path difference between the two counter-propagating beams in the fiber loop. When the closed optical path rotates clockwisely at a speed of $\Omega$ with respect to the inertial space, a corresponding optical path difference between the two counter-propagating beams is induced, and it can be given by

$$\Delta L = \frac{4A\Omega}{c}, \tag{1.8}$$

where $A$ is the area of the closed optical path, $c$ is the speed of the light in vacuum. For the $N$-turn closed optical loops, the corresponding phase difference between the two counter-propagating beams can be expressed as,

$$\Delta\varphi = \frac{8\pi NA}{\lambda c}\Omega . \tag{1.9}$$

To introduce a phase difference between the two counter-propagating beams, a section of polarization maintaining fiber (PMF) is generally connected into the fiber loop [12-15], as shown in Figure 1.6.

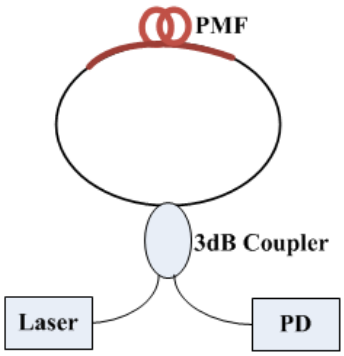


Figure 1.6 Schematic configuration of the PMF based SI

The transmitted light intensity detected by the PD can be expressed as

$$I_{out} = I_{in}\sin^2\theta[\cos\frac{\pi l(n_e - n_o)}{\lambda}]^2 , \tag{1.10}$$

where $I_{in}$ and $I_{out}$ are the intensities of the input light and output light, $\theta$ is the angle between the fast and slow axes of the input and output planes, $n_o$ and $n_e$ are the RIs of the ordinary light and extraordinary light, respectively, $l$ is the length of the PMF and $\lambda$ is the operation wavelength. To get a high

ER, one polarization controller is generally connected into the fiber loop to control the polarization state of the light propagating in the fiber loop.

It should be noted that the above-mentioned MZI, MCI and SI have some limitations, such as big volume, complicated structure, and susceptibility to ambient influences. For example, the fabrications of the MZI and MCI are generally complicated. To reduce the noise influence from the optical source, their two arms need to be designed to have the same length. Compared to the MZI and MCI, the two arms in the SI are in the same fiber, hence the SI has a relatively higher stability. However, to construct an SI, a 3 dB coupler, a polarization controller, and a section of PMF are generally needed, hence it has a relatively big footprint. Fortunately, in recent years, fiber in-line miniaturized modal interferometers (MMIs), with the length range from a few millimeters to a few centimeters, have attracted much interest due to their inherent advantages of simple and compact structure, small size, low cost, and easy fabrication. Especially, they are more stable compared to the above mentioned traditional MZI, MCI and SI, and they have been widely used as fiber filters and sensors [16-46].

## 1.2 Literature Review

The modal interferences in the MMI are due to the coupling between the core mode and excited cladding modes in one fiber. The phase difference between the core mode and the *m-th* cladding mode can be given by

$$\varphi = \frac{2\pi}{\lambda}(n_{co} - n_{cl}^{m})L, \tag{1.11}$$

where $n_{co}$ and $n_{cl}^{m}$ are the effective RIs of the core mode and *m-th* cladding mode, and $L$ is the length of the MMI. The key technique of constructing the MMI is to excite the cladding modes and let the cladding modes re-couple with the core mode in one fiber. So far, several types of MMIs have been proposed based on different fabrication techniques, and they are summarized as follows:

The first type is splicing a section of SMF between two short sections of multimode fibers (MMFs) [16] or double cladding fibers (DCFs) [17], as shown in Figures 1.7 and 1.8, respectively. The maximum ER of the DCF MMI is only around 13.5 dB [17]. Due to the modal field diameter (MFD) mismatch between the SMF and MMF or DCF, the cladding modes are effectively excited to propagate along the cladding of the SMF. After the cladding modes meet the core mode at the second splice joint, corresponding interferences occur. Note that it is not simple to construct such MMIs since four-time fusion splices need to be involved.

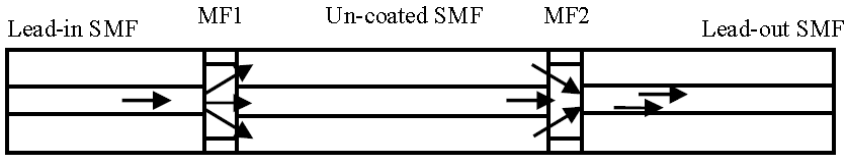


Figure 1.7 Schematic configuration of the MMF-SMF-MMF based MMI[16]

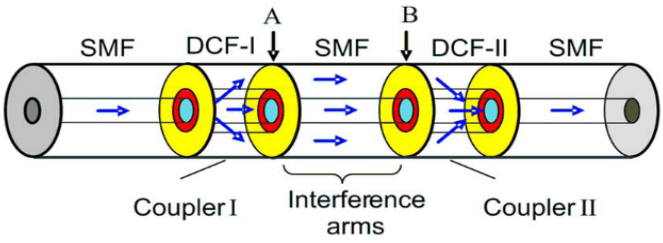


Figure 1.8 Schematic configuration of the DCF-SMF-DCF based MMI[17]

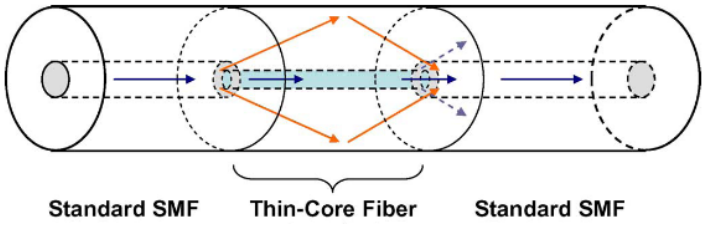


Figure 1.9 Schematic configuration of the SMF-TCF-SMF based MMI[18]

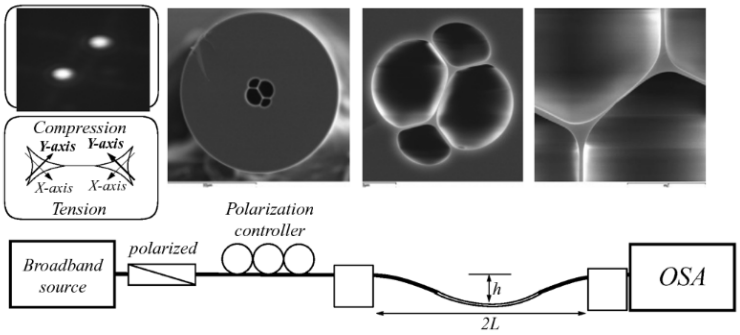


Figure 1.10 Schematic configuration of the SMF-STCF-SMF based MMI[19]

The second type is connecting a short section of thin core fiber (TCF) [18] or suspended twin core fiber (STCF) [19, 20] between the SMFs, as shown in Figures 1.9 and 1.10, respectively. The maximum ER of the STCF MMI [19] is only around 10 dB. For the TCF based MMI, due to the MFD mismatch between the TCF and SMF, the cladding modes can be effectively

excited. For the STCF based MMI, a polarization controller has to be adopted to control the polarization state of the light in the STCF. This increases the complexity of the STCF based MMI.

The third type is constructing two fiber down-tapers [21-26], two fiber bitapers [27,28], or two peanut-shape structures [29,30] in one optical fiber, as shown in Figures 1.11, 1.12 and 1.13, respectively. The maximum ER of the peanut shape MMI [30] is around 12 dB while that of down-taper MMI [24] is only around 4 dB. After introducing the tapered or peanut-shape splice joint, the MFD mismatch between the SMF and the tapered fiber or peanut-shape fiber is enlarged accordingly. This helps to excite the cladding modes to propagate along the cladding of the central fiber between the two fiber down-tapers [21-26], two fiber bitapers [27,28] or two peanut-shape structures [29,30]. To construct the fiber down-taper or peanut-shape splice joint [21], two normal cleaved ends need to be discharged firstly to get sphere shape. This increases the fabrication difficulty since the sphere shape induced by the discharge cannot be controlled. In addition, to get the bitaper splice joint, the manual operation program of a fiber splicer machine has to be applied. Hence, the reproducibility of fabricating the two fiber bitapers based MMI is not good.

The fourth type is core-offsetting one fiber splice joint [31-35] in an MMI, as shown in Figure 1.14. The maximum ER of the PMPCF MMI [34] is only around 7 dB. By introducing a core-offset between one SMF and the other

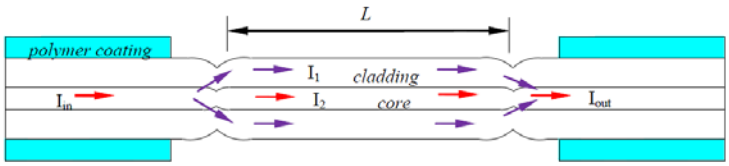


Figure 1.11 Schematic configuration of the two fiber down-tapers based MMI [21]

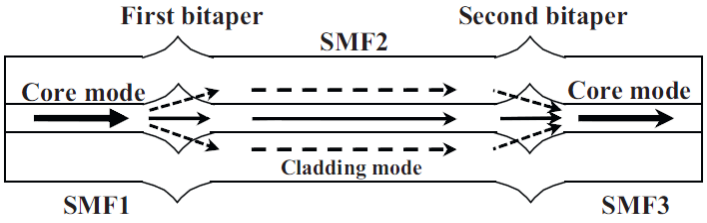


Figure 1.12 Schematic configuration of the two fiber bitapers based MMI [28]

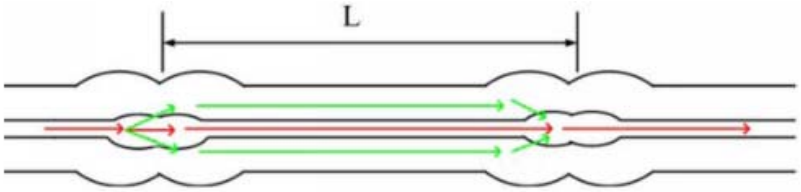


Figure 1.13 Schematic configuration of the two peanut-shape structures based MMI [30]

SMF [31, 32], MMF [33], or photonic crystal fiber (PCF) [34-36], the cladding modes can be effectively excited. As can be seen, due to the core-offset, the core mode and the cladding modes propagating along the MMI become unsymmetrical, which induces the corresponding polarization characteristics of the MMI. Moreover, to introduce the core-offset, the manual splicing method has to be applied, which increases the complexity and difficulty of fabricating such MMIs. This leads to the poor reproducibility to fabricate such MMIs.

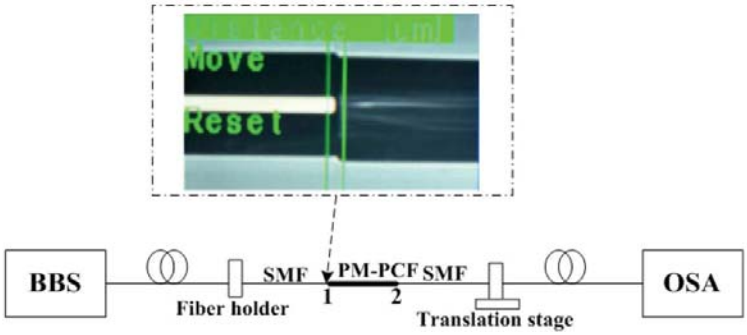


Figure 1.14 Schematic configuration of the one core-offset splice joint based MMI [34]

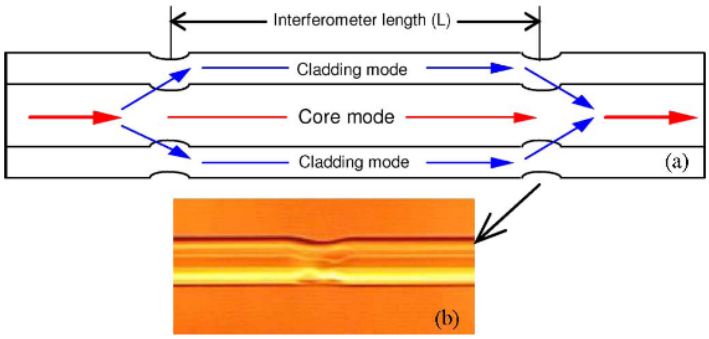


Figure 1.15 Schematic configuration of the MMI fabricated by laser irradiation points [37]

The fifth type is constructing laser irradiation points in one fiber [37–40]. Figure 1.15 (b) shows the typical photograph of the laser modification region in one SMF [37]. To construct laser irradiation points in one fiber, the $CO_2$ laser or femtosecond laser with a complex precision fabrication system has to be applied. This greatly improves the cost to fabricate such MMIs.

The sixth type is collapsing the air holes of the PCF [41-46]. J. Villatoro et.al [42] summarized the methods of constructing the collapsed PCF air holes based MMIs, as shown in Figure 1.16. One is collapsing two air hole regions

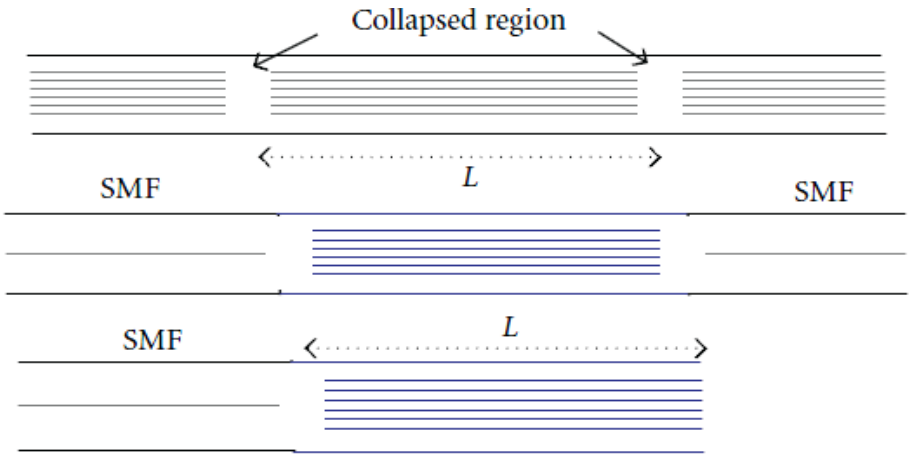


Figure 1.16 Schematic configuration of the collapsed PCF air holes based MMIs[42]

along a PCF, the second one is splicing a section of PCF between the SMFs with two collapsed air hole regions, and the third one is splicing a section of PCF with one collapsed air hole region. The maximum ER of the tapered and collapsed PCF MMIs [42] is around 11 dB. It should be noted that the MMIs based on the collapsed PCF air holes generally have a large insertion loss. Moreover, collapsing the air holes of the PCF cannot be controlled, hence such PCF based MMIs have poor fabrication reproducibility.

## 1.3 Objectives and Contributions of This Thesis

The objectives of this thesis are summarized as follows:

Firstly, based on the above literature review, the MMIs have shown the inherent advantages over the MZI, MCI and SI, especially, they have wide

applications in fiber filters and fiber sensors. Currently, they have been a hot research topic. However, most of the above-mentioned MMIs have a low ER and poor fabrication reproducibility since their fabrication methods, such as four-time fusion splices, fiber ends pre-discharge, manual splice, core-offset, and air holes collapsing, cannot guarantee their reproducibility. Hence, the two disadvantages greatly limit their practical applications. To address the limitations being in face of the current MMIs, especially for the SMF based MMIs, two types of SMF based MMIs, with a high ER and good fabrication reproducibility, are proposed and demonstrated by using a commercial splicer with optimized splicing parameters. Moreover, their applications as fiber sensors are also investigated theoretically and experimentally.

Secondly, for the active fibers, their RI is both wavelength dependent and gain dependent. Hence, the active five based MMIs experience an additional phase shift when an optical pump is introduced. This makes their thermal characteristics become more complicated. In this study, the intensity and wavelength dependent thermal characteristics of an Er-Yb codoped phosphosilicate fiber (EYPF) based MMI are investigated theoretically and experimentally.

Thirdly, for the photonic bandgap fiber (PBF) based MMIs, when they are used as temperature sensors, they have lower thermal sensitivity due to their air hole structures in the fiber core and claddings. To address this

limitation, the fully and partially ethanol-filled PBFs are proposed to construct the MMIs for temperature sensing with high thermal sensitivities.

The contributions of this thesis are summarized as follows:

Firstly, the first type of SMF based MMI, a fiber down-taper MMI, with a high ER and good fabrication reproducibility, is proposed and demonstrated. With the optimized discharge parameters of a commercial fusion splicer and a simple mechanical taper setup, it can be constructed by fabricating two adjacent fiber down-tapers along one same SMF. Its ER can reach 24 dB, and It is both sensitive to temperature and RI, with temperature and RI sensitivities of- 72.8 pm/°C and 10.299 nm/RIU. If serially connecting it to a fiber Bragg grating (FBG), simultaneous measurement of temperature and RI can be achieved by building a dual parameters measurement matrix. The temperature and RI measurement resolutions reach ±1.1°C and ± 0.009, respectively, and are better than those of the other dual parameter measurement method.

Secondly, the second type of MMI, a dual cladding modes (DCMs) fiber up-taper MMI, with a high ER and good fabrication reproducibility, is proposed and demonstrated. With a suitable "overlap" parameter of a commercial fusion splicer, high-ER DCMs fiber MMIs can be constructed automatically by fabricating two adjacent fiber up-tapers along one same SMF. It is almost like a long period grating (LPG)-type device, also with a deep resonance dip within C and L bands. Its ER can reach 27.7 dB, and It can be

used for strain, temperature, RI, micro-displacement, ultrasound, and dual parameters (strain and temperature) measurements. Due to its simultaneous responses to the acoustic pressure in wavelength shift and intermodal power coupling change, it can be used as an intensity-modulated fiber acoustic sensor with an ultrahigh sensitivity of 2.65 V/μPa. When it is used as a strain or ultrasound sensor, a pre-strain can be applied to compensate the temperature influence since it has opposite wavelength shift trends in response to temperature and strain. By embedding it into a cured carbon fiber composite based beam, it can be used as an intensity-modulated micro-displacement sensor with a high sensitivity of -0.0214 dB/μm, and its temperature-cross issue can be solved by applying a pre-displacement since it has opposite ER variation trends in response to displacement and temperature. With just one MMI, simultaneous measurement of strain and temperature can be achieved by monitoring its two resonance dips in wavelength shift response to temperature and strain. Since its two cladding modes in the MMI have different temperature and strain sensitivities, a mode division multiplexing(MDM) method can be used to realize simultaneous temperature and strain measurement with high measurement resolutions of ±0.05 C° and ±3.14 με.

Thirdly, the particular thermal characteristics of an EYPF fiber based MMI are investigated theoretically and experimentally. As can be seen, most of the above-mentioned MMIs are based on the passive fibers, such as SMF,

MMF, DCF, and PCF. However, when the MMI is constructed by the active fiber, it shows many other characteristics, especially, when an additional optical pump is introduced into the active fiber. If no additional optical pump is introduced, it can be used as a high sensitivity temperature sensor. However, once an additional optical pump is launched into the interferometer, its thermal sensitivity is reduced. Thermal sensitivities of 3.1 pm/°C and 10.3 pm/°C are reduced for the resonance dips at the short and longer wavelength ranges of the MMI under a pump power of 59.4 mW. This suggests that its thermal sensitivity can be controlled and its stability can be improved by introducing an additional optical pump.

Fourthly, the thermal performances of the fully and partially ethanol-filled PBF based MMIs are investigated theoretically and experimentally. Compared to the ethanol-filled solid core PCFs, the ethanol-filled PBFs are much easier to excite more high order cladding modes. This lets them easily construct the core-mode MMIs without using the other special splicing techniques. When the PBF based MMIs are used as temperature sensors, their thermal sensitivities are relatively lower. After filling the ethanol into the air core and/or air claddings of the PBF and splicing a short section of the ethanol-filled PBF between two SMFs, the MMI with high thermal sensitivity can be achieved. The fully and partially ethanol-filled PBF based MMIs have the thermal sensitivities of -292 pm/°C and -120 pm/°C, respectively, and they are 43.8 and 18 times bigger than that of the

unfilled one. Moreover, its thermal sensitivity can be adjusted by selectively filling the air core and/or air claddings of the PBF with ethanol.

## 1.4 Organization of This Thesis

This thesis is organized into six chapters, with this chapter (Chapter 1) being the introduction.

Chapter 2 focuses on the high ER fiber down-taper MMI and its applications as fiber sensors. Its theoretical simulation, principle and fabrication method are demonstrated firstly, then its sensing performances for temperature, RI and dual parameters (temperature and RI) measurements are investigated.

Chapter 3 focuses on investigating the particular thermal characteristics of an EYPF based down-taper MMI. The optical pump induced thermal sensitivity reduction of an EYPF based down-taper MMI is investigated theoretically and experimentally.

Chapter 4 focuses on the high ER DCMs fiber up-taper MMI and its applications as fiber sensors. The theoretical simulation, principle and fabrication method of this MMI are demonstrated firstly, then its performances as strain, temperature, RI, micro-displacement, ultrasound, and dual parameters sensors are investigated.

Chapter 5 focuses on the fully and partially ethanol-filled PBF based MMIs. Their fabrication method, principle and mode excitation simulation are

addressed firstly, then their performances as temperature sensors are investigated.

Chapter 6 summarizes the accomplishments on the research work presented in this thesis and provides some recommendations for future work.

References used in this thesis are listed at the end of the thesis.

# Chapter 2

# High ER Fiber Down-Taper MMI

In this chapter, a high ER fiber down-taper MMI based on the SMF is proposed. Its interference principle is analyzed firstly based on a beam propagating method (BPM), then its performances as temperature, RI and dual parameters (temperature and RI) sensors are investigated.

## 2.1 Introduction

As we all know, the primary requirement for the fiber filter is its high ER. For fiber sensor applications, its high ER can improve the measurement accuracy both for wavelength and intensity measurements. Moreover, the high ER filter can be used as a quasi-linear filter for low cost intensity-referenced measurement [47]. It should be noted that it is difficult to fabricate a high ER fiber down-taper MMI on the common SMF since the RI contrast between the core and cladding is small. Generally, the common SMF down-taper based

MMI is below 5 dB due to the un-optimized waist diameter of about 65 μm [24]. A high ER fiber down-taper MMI can be fabricated on the EYPF with a 50-μm waist diameter since the fiber has a high index contrast between the cladding and highly phosphorous doped core [25,26].

In this study, a novel method of fabricating the high ER SMF based down-taper MMI is proposed and demonstrated. With an arc discharging method, by optimizing the discharge parameters of a commercial splicer and designing a simple mechanical taper setup, the MMI with about 24-dB ER can be achieved by fabricating two fiber down-tapers with 20-μm waist diameter on one same SMF. Moreover, its applications for temperature, RI and dual parameters (temperature and RI) measurements are also investigated theoretically and experimentally. Experimental results show that it is highly sensitive to temperature variation. However, when it is used as an RI sensor, its sensitivity is not very high since the propagating position of the cladding mode is more close to that of the core mode. If serially connecting it to an FBG, simultaneous measurement of temperature and RI is achieved based on a dual parameter measurement matrix, and the measurement resolutions are better than those of the other dual parameters measurement method.

## 2.2 Theoretical Simulation

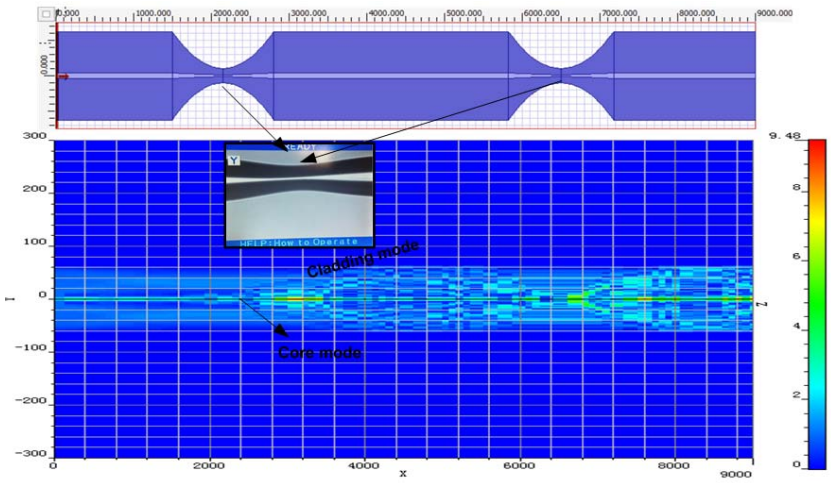


Figure 2.1 Schematic structure of the MMI and the simulated light field propagation in the MMI

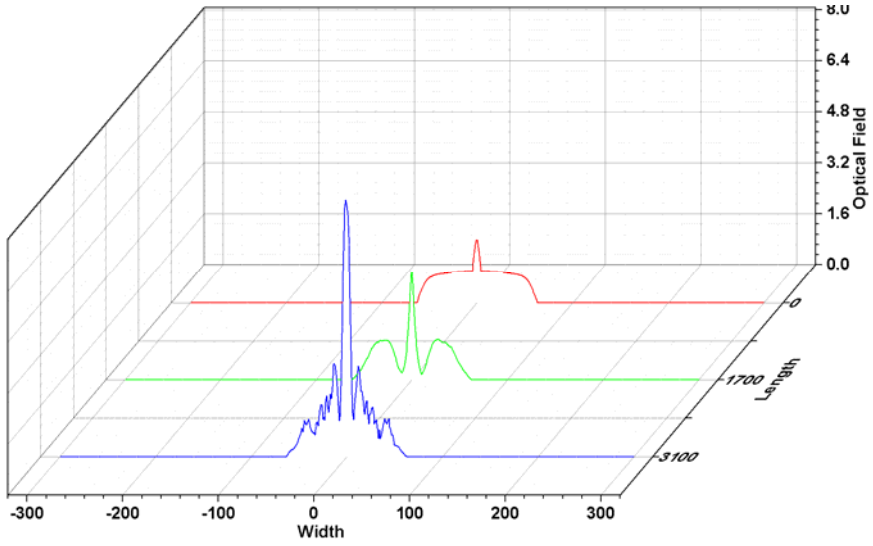


Figure 2.2 Simulated light mode propagation status when the light propagates to the first taper

Figure 2.1 shows the schematic structure of the MMI and the simulated light field propagation in the MMI. The inset in Figure 2.1 is the microscope image

of the typical fiber down-taper. The light propagation in the MMI was simulated by using a BPM method. The LP01 mode of the SMF at wavelength 1550 nm was used as the input optical field, and the minimum waist diameter and tapered length were set as 20 μm and 2.5 mm, respectively. As can be seen, when the light propagates to the first fiber down-taper, one part of the energy of the LP01 mode is effectively excited to the fiber cladding as cladding modes. After they propagate to the second fiber taper, they re-couple with the core mode. Figure 2.2 shows its light mode propagation status when the light propagates to the first fiber down-taper. It can be seen that one dominated cladding mode is excited at the output of the first fiber down-taper. When the cladding mode propagates to the second fiber down-taper, it re-couple with the core mode to construct a Mach-Zehnder interference.

## 2.3 Principle of Operation

Its phase $\varphi$ at the output ( $z = L$ ) could be given by,

$$\varphi = \frac{2\pi}{\lambda}[n_{co}L - \int_0^L n_{cl}(z)dz] \ , \tag{2.1}$$

where $n_{co}$ and $n_{cl}(z)$ are the effective RIs of the core and cladding modes, respectively, and $n_{cl}(z)$ is position dependent. Setting $\int_0^L n_{cl}(z)dz = \overline{n}_{cl}L$ , where $\overline{n}_{cl}$ is the averaged effective RI of the cladding mode and it is position dependent, then $\varphi$ can be expressed as

$$\varphi = \frac{2\pi}{\lambda}(n_{co} - \overline{n}_{cl})L \,. \tag{2.2}$$

As the phase satisfies the condition of $\varphi = (2k+1)\pi$, where $k$ is the interference order, the dip resonance wavelength of $\lambda_d$ occurs, and it could be expressed as

$$\lambda_d = \frac{2}{2k+1}(n_{co} - \overline{n_{cl}})L \,. \tag{2.3}$$

For the two-mode MMI, its ER can be given by [33]

$$ER \approx 10\lg(\frac{1+\sqrt{I_2/I_1}}{1-\sqrt{I_2/I_1}})^2 \,, \tag{2.4}$$

where $I_1$ and $I_2$ are the powers distributed in the core mode and cladding mode, respectively. With the increase of the power ratio of the two modes, the ER of the MMI increases accordingly. For a high ER MMI, it is clear that the power $I_2$ is more close to $I_1$. This means that the propagation position of the cladding mode is more close to that of the core mode in the symmetrical fiber structure, which reduces the RI sensitivity of the cladding mode to ambient RI variation, but the coupling condition between the core and cladding modes also changes accordingly. This leads to a corresponding dip wavelength shift of $\Delta\lambda_{dr}$, and it can be given by

$$\frac{\Delta\lambda_{dr}}{\lambda_d} = (\alpha_r + \beta_r)\Delta n_r \,, \tag{2.5}$$

where $\alpha_r = \frac{1}{L}\frac{dL}{dn_r}$ is a constant that describes the RI variation induced length variation of the MMI, and $\beta_r = \frac{1}{n_{co} - \overline{n_{cl}}}\frac{d(n_{co} - \overline{n_{cl}})}{dn_r}$ is a constant that describes the RI variation induced effective RI difference of the two modes, and $\Delta n_r$ is the value of the ambient RI variation.

Since the core and cladding modes propagate in different waveguide structures of the MMI, the temperature variation must affect the two modes in different manners. The thermo-optic coefficients of the core and cladding modes are denoted by $\xi_{co}$ and $\xi_{cl}$, respectively. The temperature induced effective RI variation can be given by

$$\Delta(n_{co} - \overline{n_{cl}}) = (\xi_{co} n_{co} - \xi_{cl}\overline{n_{cl}})\Delta T\,, \tag{2.6}$$

and the temperature induced length variation of the MMI can be given by

$$\Delta L = \alpha_d L \Delta T\,, \tag{2.7}$$

where $\alpha_d = \frac{1}{L}\frac{dL}{dT}$ is the thermal-expansion coefficient of the MMI. Hence the dip wavelength shift of $\Delta\lambda_{dt}$ due to temperature variation can be expressed as,

$$\frac{\Delta\lambda_{dt}}{\lambda_d} = (\alpha_d + \xi_d)\Delta T\,, \tag{2.8}$$

where $\xi_d = \dfrac{\xi_{co} n_{co} - \xi_{cl} \overline{n_{cl}}}{n_{co} - \overline{n_{cl}}}$, is a constant that describes the thermal-induced variation of the effective RI difference of the two modes.

According to Eqs.2.5 and 2.8, the MMI is both RI and temperature sensitive. Hence, if using the MMI as an RI sensor, the temperature influence has to be eliminated. Fortunately, an FBG is only sensitive to the temperature variation while independent to the RI variation since the light only propagates along the core of the FBG. By serially connecting them to construct an MMI-FBG structure, the temperature influence on the MMI can be effectively eliminated by building a dual parameter measurement matrix. The temperature variation induced Bragg wavelength shift of $\Delta\lambda_b$ of the FBG can be given by

$$\frac{\Delta\lambda_b}{\lambda_b} = (\alpha_b + \xi_b)\Delta T , \tag{2.9}$$

where $\alpha_b = \dfrac{1}{L_b}\dfrac{dL_b}{dT}$ and $\xi_b = \dfrac{1}{n_b}\dfrac{dn_b}{dT}$ are the thermal-expansion and thermal-optic coefficients of the FBG, and $n_b$ and $L_b$ are the effective core RI and length of the FBG.

When the ambient RI and temperature change, the measurement matrix for the RI and temperature can be given by

$$\begin{bmatrix} \Delta\lambda_d \\ \Delta\lambda_b \end{bmatrix} = \begin{bmatrix} K_{dt} & K_{dr} \\ K_{bt} & K_{br} \end{bmatrix} \begin{bmatrix} \Delta T \\ \Delta n_r \end{bmatrix}, \tag{2.10}$$

where $K_{bt} = \alpha_b + \xi_b$ , $K_{dt} = \alpha_d + \xi_d$ , $K_{br} = 0$ , $K_{dr} = \alpha_r + \beta_r$ . Under a given wavelength measurement errors of $\delta(\Delta\lambda_d)$ and $\delta(\Delta\lambda_b)$, the resolutions of the measured temperature and RI could be given by

$$\begin{bmatrix} \delta(\Delta T) \\ \delta(\Delta n_r) \end{bmatrix} = \pm \frac{1}{|D|} \begin{bmatrix} |K_{dr}| & |K_{br}| \\ |K_{dt}| & |K_{bt}| \end{bmatrix} \begin{bmatrix} |\delta(\Delta\lambda_b)| \\ |\delta(\Delta\lambda_d)| \end{bmatrix}, \tag{2.11}$$

where $D = |K_{dt}K_{br} - K_{dr}K_{bt}|$ is the absolute value of the determinant of the coefficient matrix. Under a given measurement resolution, a bigger value of D is desirable for a higher sensing resolution. Obviously, if the two items of $K_{dt}K_{br}$ and $K_{dr}K_{bt}$ have the opposite signs, or one of them is far bigger than the other item, a bigger value of D can be achieved. This leads to high measurement resolutions in temperature and RI. Here, since the FBG is independent to the RI variation, $K_{bc} = 0$ and $D = |K_{dr}K_{bt}|$, the sensor is potential for a high measurement resolution.

## 2.4 Fabrication of the MMI

Generally, there are two heating techniques to fabricate the fiber down-taper, point flame and discharge. Compared to the point flame heating, the discharge heating using a commercial splicer is easier, more robust and repeatable since it can be automatically controlled by setting suitable discharge parameters. Compared to the commonly used discharge method, the arc discharge can produce a low level of heating and it is desirable for tapering a fusion splice.

To introduce the fiber down-tapers on the fiber, a commercial splicer (Fujikura FSM-40S) was applied to produce the arc discharge to heat the fiber. The MMI is constructed on a short-length SMF with two adjacent down-tapers.

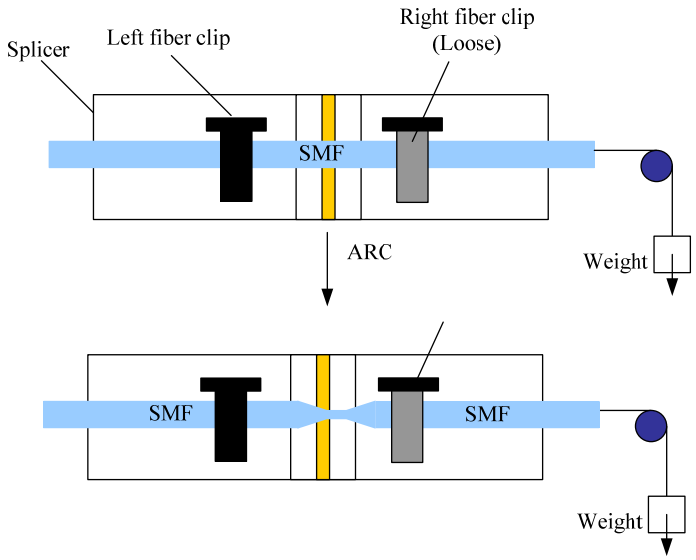


Figure 2.3 Fabrication process for the fiber down-taper MMI

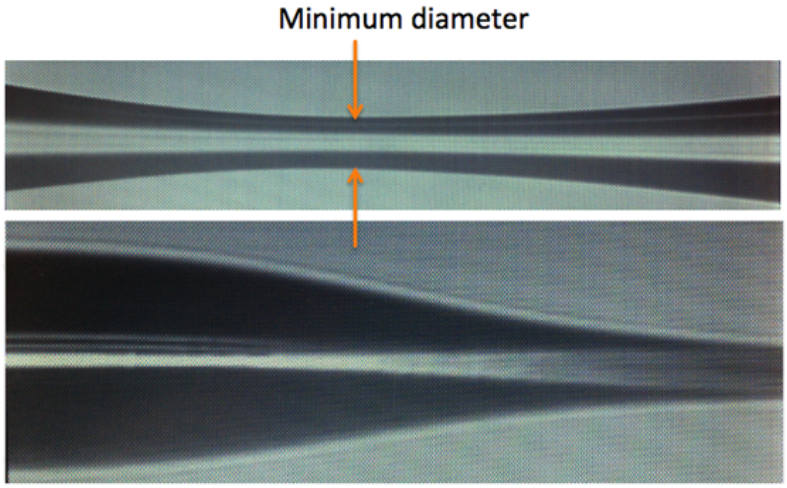


Figure 2.4 Typical microscope image of the fiber down-taper

Figure 2.3 shows the fabrication process for the fiber down-taper on the SMF. The left side of the fiber was fixed by the left fiber clip, and the right side of the fiber was loosely hold by the right fiber clip and pulled by a weight through a smooth supporting axle. When the arc discharge heating was applied to the central part of the SMF, it was automatically down-tapered. The tapered fiber transition and waist diameters can be controlled by changing the applied weight via a pulley. By optimizing the parameters of the arc discharge power and the applied weight, a high ER MMI can be fabricated.

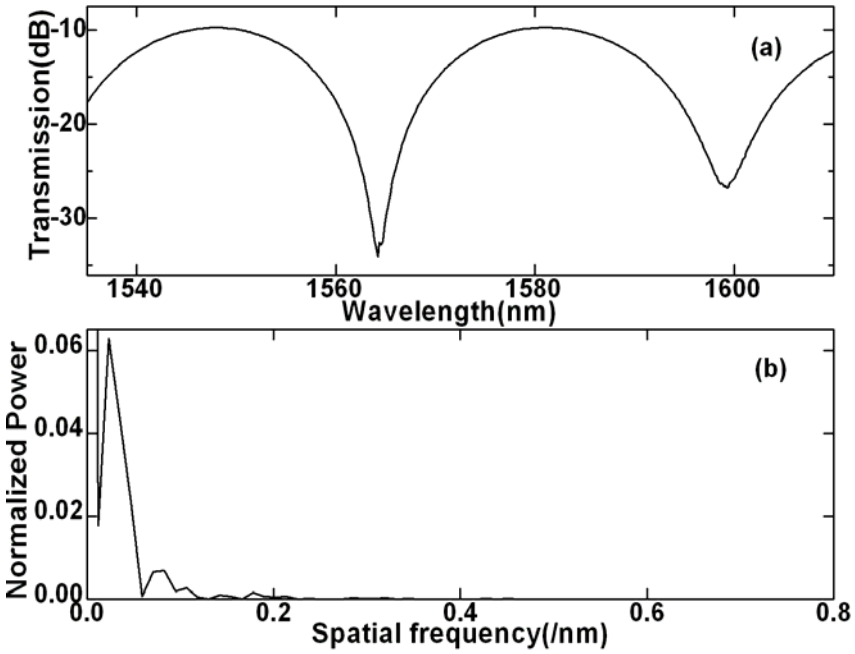


Figure 2.5 Transmission spectrum of the MMI and its corresponding spatial frequency spectrum

Figure 2.4 shows the typical microscope image of the fiber down-taper. To obtain the MMI with a high ER of more than 20 dB and low insertion loss, repeat experiments were performed by optimizing the parameters of the arc

discharge power, arc time and the applied weight. Under the arc discharge power and arc time of 52 bit (default arc power unit: bit) and 200 ms, if applying a weight of 25.7 g, the MMI with more than 20-dB ER and low insertion loss can be achieved. The fiber down-taper has a waist diameter of ~20 μm. Figure 2.5 (a) shows the typical transmission spectrum of the MMI with a length of ~2 cm and a central un-tapered length of ~ 1.5 cm. As can be seen, its ER reaches 24 dB. To determine the number and power distribution of the interference modes, the wavelength spectrum in Figure 2.5 (a) was Fourier transformed to obtain the spatial frequency of the interference fringes, as shown in Figure 2.5 (b). It is clear a dominated cladding mode is excited, which agrees well to the simulated results.

We also investigated the MMIs with the same length of ~2 cm and central un-tapered length of ~1.5 cm under the waist diameters of 35 and 10 μm. Figure 2.6 shows their typical transmission spectra. The ER of the MMI under 10-μm waist diameter reaches 22 dB while it is less than 10 dB under 35-μm waist diameter. Compared to the MMI under 20-μm waist diameter with 24-dB ER, although the ER of the MMI under 10-μm waist diameter reaches 22 dB, its insertion loss is too high and the dip loss is as low as -55 dB. Moreover, it has many noise jitters. Hence, the optimized MMI under 20-μm waist diameter is the best choice for the fiber sensor and filter.

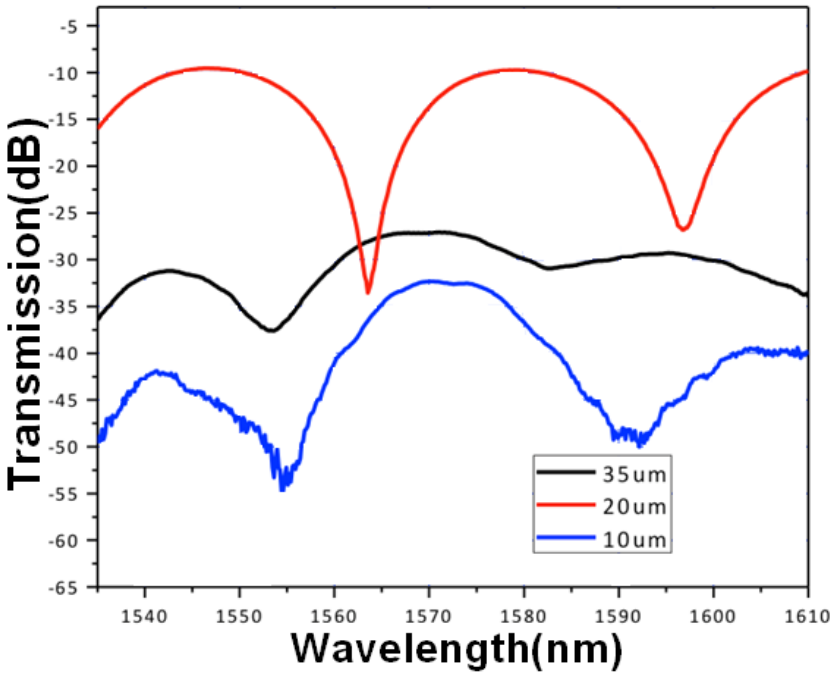


Figure 2.6 Transmission spectra of the MMI under different taper waist diameters

## 2.5 RI and Temperature Sensing

To compare the temperature and RI sensing performances of the MMI, an FBG was serially connected to the MMI as the reference, and its central wavelength, 3-dB bandwidth, and length are 1534.102nm, 0.2 nm, and 10 mm, respectively. The schematic configuration of the experimental setup is shown in Figure 2.7. It should be noted that the core-cladding MMI is highly bending sensitive. To avoid the bending effect, the MMI was fixed on a U-shape metal slab during the experiment. A C and L broadband source (BBS) was used as the optical source. Its transmission spectrum was measured by an optical spectrum analyzer (OSA) with a 0.01-nm resolution. The RI solution was

prepared by using homogeneous sugar-water solutions with different RIs. The temperature of the sugar solution was tuned by a temperature controller and calibrated by a digital thermometer. With the increase of the RI, the transmission spectrum of the MMI experiences a corresponding red shift while that of the FBG keeps unchanged, as shown in Figure 2.8.

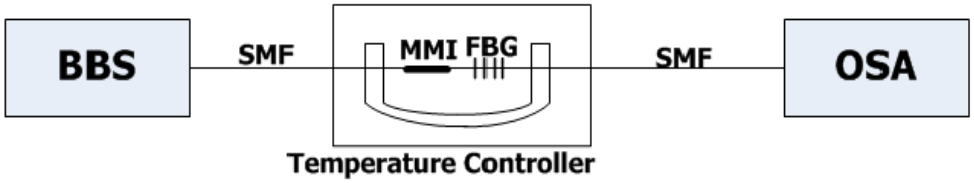


Figure 2.7 Schematic structure of the experimental setup

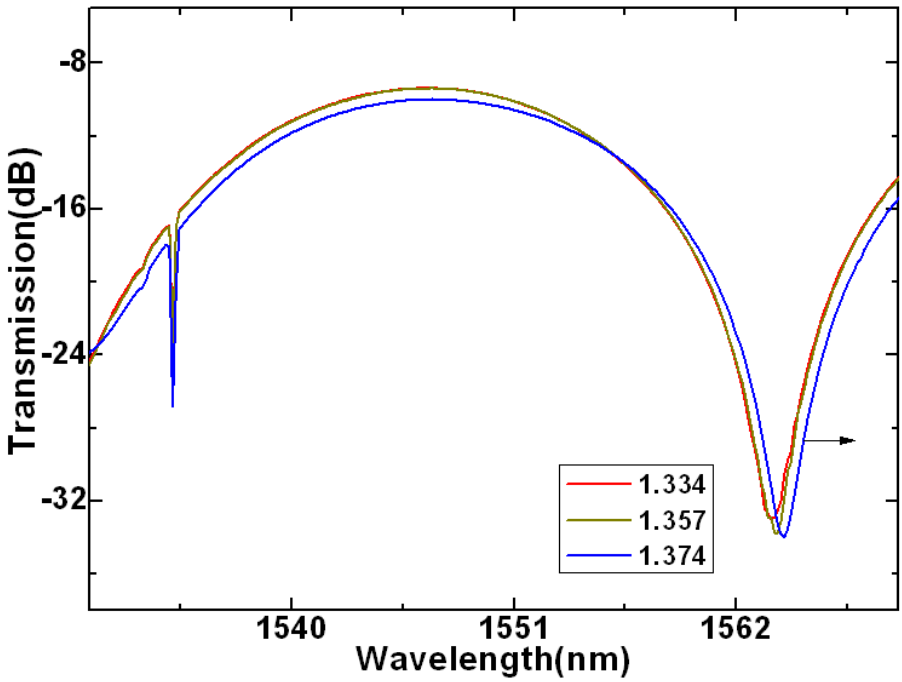


Figure 2.8 Transmission spectral responses to RI

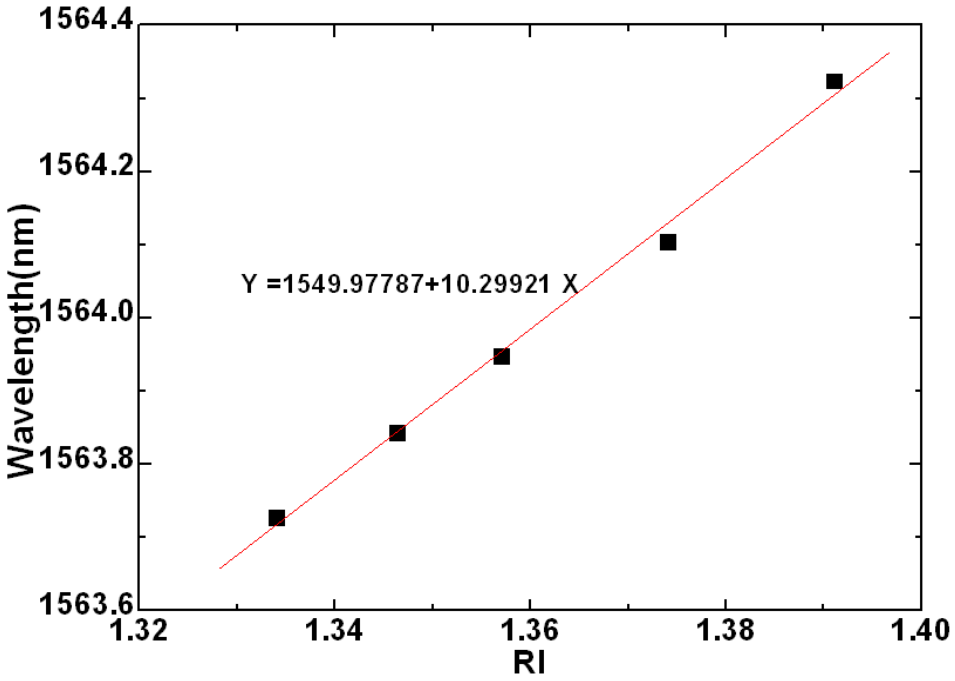


Figure 2.9 Wavelength versus RI

There is a quasi-linear relationship between the RI and dip wavelength shift of the MMI, and its RI sensitivity is 10.299 nm/RIU and the linear R-square is 0.993, as shown in Figure 2.9. Compared to the core-offset type of PCF based MMI [34] with a sensitivity of 629.76 nm/RIU, it is relatively lower. This is due to the propagation position of the cladding mode in the high ER MMI is more close to that of the core mode. It can also be seen from the smaller ER variation, the maximum ER variation due to the RI variation is only about 0.754 dB. This agrees to our predication.

As ambient temperature increases, its transmission spectrum has a corresponding blue shift while that of the FBG experiences a red shift, as shown in Figure 2.10. Within the temperature range of 23.4~60°C, there is a

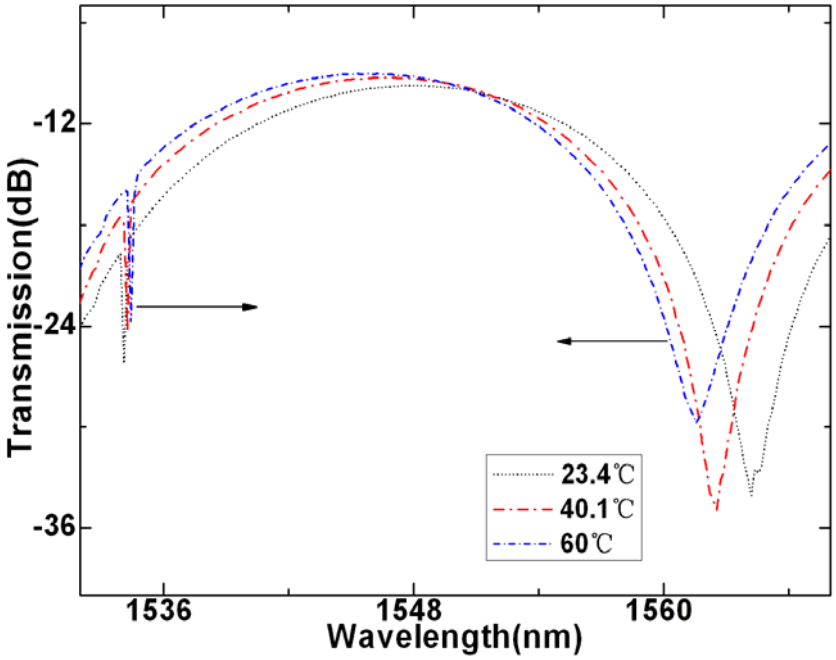


Figure 2.10 Transmission spectral responses to temperature

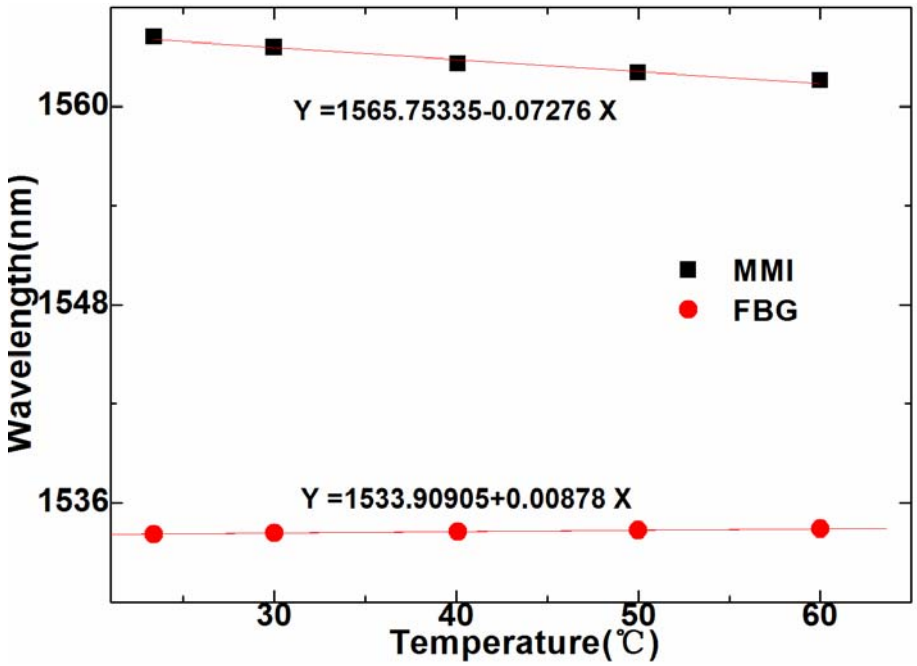


Figure 2.11 Wavelength versus temperature

quasi-linear relationship between the temperature variation and wavelength shift. The temperature sensitivity of the MMI reaches -72.8 pm/°C while that of the FBG is only 8.8 pm/°C, and the linear R-squares of the MMI and FBG are 0.98 and 0.99, respectively, as shown in Figure 2.11. It is clear that this type of device is a better candidate for a thermal sensor. Since the MMI has a high ER, with a single wavelength laser and a PD, it can be used as a low cost intensity-referenced temperature or RI sensor by using it as a quasi-linear filter [47].

Since the connected FBG is insensitive to RI, this can help to improve the dual parameters measurement resolutions [48]. According to Eq.2.10, combining the thermal and RI measurement results of the MMI and FBG as a dual parameters measurement matrix, it can be given by

$$\begin{bmatrix} \Delta\lambda_d \\ \Delta\lambda_b \end{bmatrix} = \begin{bmatrix} -72.8 & 10299 \\ 8.8 & 0 \end{bmatrix} \begin{bmatrix} \Delta T \\ \Delta n_r \end{bmatrix}, \tag{2.12}$$

According to Eq.2.11, the measured RI and temperature resolutions can be expressed as

$$\begin{bmatrix} \delta(\Delta T) \\ \delta(\Delta C_x) \end{bmatrix} = \pm \frac{1}{|90631.2|} \begin{bmatrix} 10299 & 0 \\ 72.8 & 8.8 \end{bmatrix} \begin{bmatrix} |\delta(\Delta\lambda_b)| \\ |\delta(\Delta\lambda_d)| \end{bmatrix}, \tag{2.13}$$

The measurement resolutions are limited by the wavelength resolution of the OSA. Under a wavelength resolution of 10 pm, the temperature and RI measurement resolutions are ±1.1°C and ± 0.009, respectively, and they are 6.6 and 2.4 times bigger than those in Ref. [24] with only ±7.3°C and ± 0.022.

Hence, our measurement results are acceptable for the common measurement requirements. It should be noted that the RI measurement sensitivity could be improved by adopting the MMI with a smaller waist diameter and a lower ER. However, the MMI with a smaller waist diameter has a larger insertion loss, is more fragile, and cannot be used as a low cost intensity-referenced sensor due to the lower ER.

## 2.6 Conclusions

In conclusion, the high ER SMF based MMI has been demonstrated. With the arc discharge method, it can be fabricated by using the optimized splicing parameters of a commercial splicer and a simple mechanical taper setup. It could be used as a highly sensitive thermal sensor. Its RI sensitivity is not so high since the propagation position of cladding mode is more close to that of the core mode in the MMI. Combining it with an FBG for dual parameters measurement, the measurement resolutions are better than those of the other dual parameters measurement method. It has exhibited the advantages of simple and compact structure, high ER, small size, low cost, and easy fabrication. It has potential to have more applications as fiber filters and fiber sensors.

# Chapter 3

# Thermal Characteristics of the EYPF based MMI

In this chapter, the particular thermal characteristics of an EYPF based MMI is demonstrated. Without an additional optical pump launched into it, it can serve as a high temperature sensor. However, its thermal sensitivity is reduced once an additional optical pump is launched into it.

## 3.1 Introduction

For the active fiber in-line MMIs, based on the Kramers-Kronig theory [49-52], their RI is not only wavelength dependent but also gain dependent. Hence, once a pump is launched into this type of devices, they experience an additional phase shift. This makes their thermal characteristics becomes more complicated. In this study, the intensity and wavelength dependent thermal

characteristics of an EYPF based MMI are demonstrated theoretically and experimentally. The MMI can be used as a high sensitivity temperature sensor if no additional optical pump is introduced. However, when an additional optical pump is launched into the MMI, its thermal sensitivity is reduced. This suggests that its thermal sensitivity can be controlled and its stability can be improved by introducing an additional optical pump.

The MMI is fabricated in a short length EYPF with two adjacent fiber down-tapers. With a BBS exciting the interference pattern of the MMI and an additional optical pump at 974.3-nm providing the gain to the MMI, the thermal characteristics of the MMI are demonstrated. When ambient temperature increases, the transmission spectrum of the MMI experiences a corresponding blue shift. Once introducing into the 974.3-nm optical pump, the blue shift is reduced. Experimental results show that there is a quasi-linear relationship between the wavelength shift and temperature variation. When the additional optical pump is launched into the interferometer, the thermal sensitivity of the interferometer is reduced. Experimental results show that under a pump power of 59.4 mW, thermal sensitivities of 3.1 pm/°C and 10.3 pm/°C are reduced for the resonance dips at the short and longer wavelength ranges of the MMI, respectively.

## 3.2 Experimental Setup and Sensing Principle

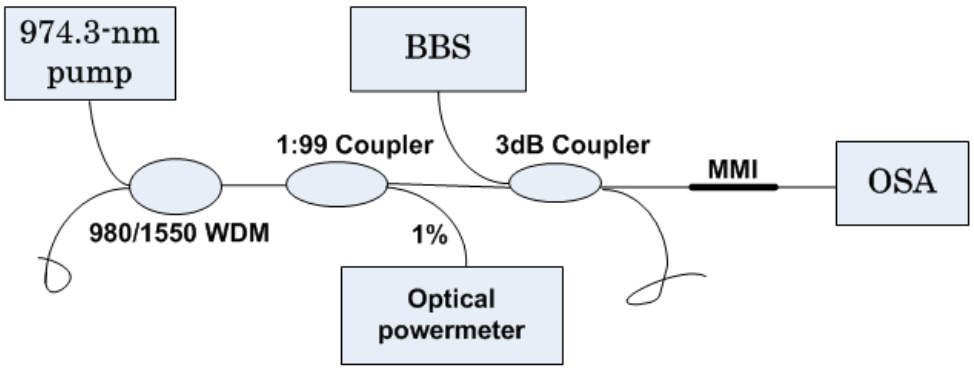


Figure 3.1 Schematic configuration of the experimental setup

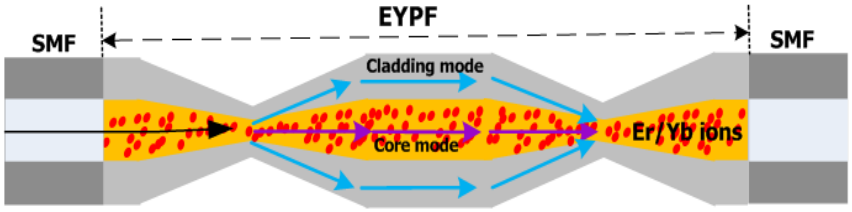


Figure 3.2 Schematic structure of the MMI

The schematic experimental setup is shown in Figure 3.1. An un-polarized C and L BBS was used as the light source. A 974.3-nm optical pump was launched into the MMI after passing through a 980/1550 nm wavelength division multiplexer (WDM), a 1:99 coupler and a 3dB coupler. The transmission spectrum of the MMI was measured by an ADVAVTEST Q8384 OSA. An optical power meter was used to monitor the 1% pump power via a 1:99 coupler, which could be used to conclude the optical power launched into the MMI. To avoid the bending effect, the MMI was placed on a U-groove slab in a temperature controller. The schematic structure of the MMI is shown

in Figure 3.2. It was fabricated on a 10.5-mm EYPF with two fiber abrupt down-tapers by using a point hydrogen flame in which the flame edge could provide a higher heating temperature than the inner portion. The diameters of the waist and lengths of the two fiber abrupt tapers are about 43.4 and 430 μm, and 56.1 and 470 μm, respectively. The distance between the two centers of the abrupt tapers is ~5 mm. The EYPF is a single mode Er/Yb co-doped fiber from Fibercore Company. It has a Numerical Aperture (NA) of 0.22, mode field/outside diameter of 5.9/125 μm, and cut-off wavelength below 1050 nm. The absorption is ~1000, ~12.5, and ~20 dB/m at wavelengths of 975, 1047, and 1532 nm, respectively.

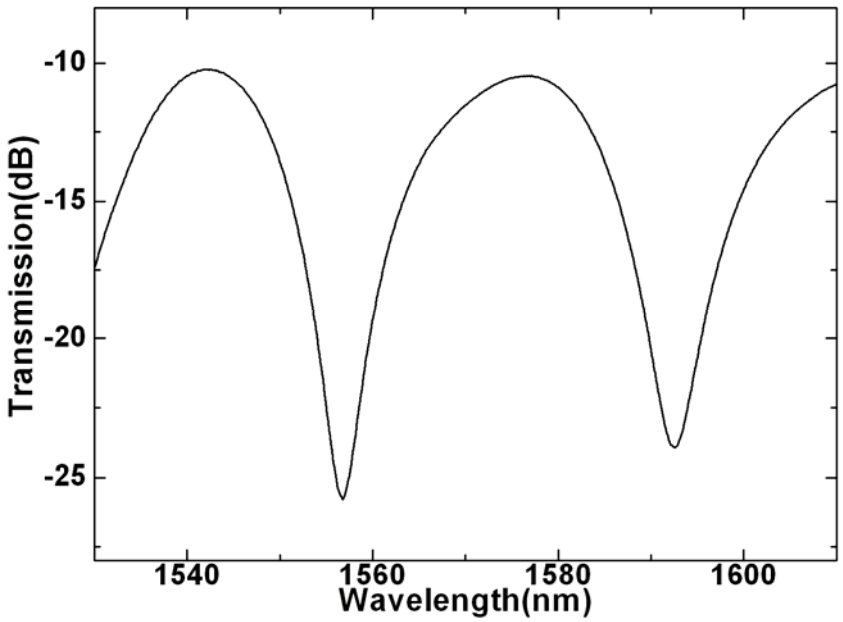


Figure 3.3 Transmission spectrum of the interferometer

As shown in Figure 3.2, when the fundamental mode propagates to the first taper, it excites the primary fundamental core mode and the other higher

order cladding modes. Moreover, the core mode and cladding modes propagate along the high-index active core and low-index passive cladding, respectively. When they meet at the second fiber taper, corresponding interferences occur between the core and cladding modes. Figure 3.3 shows the typical transmission spectrum of the MMI. Its ER reaches 15.6 dB.

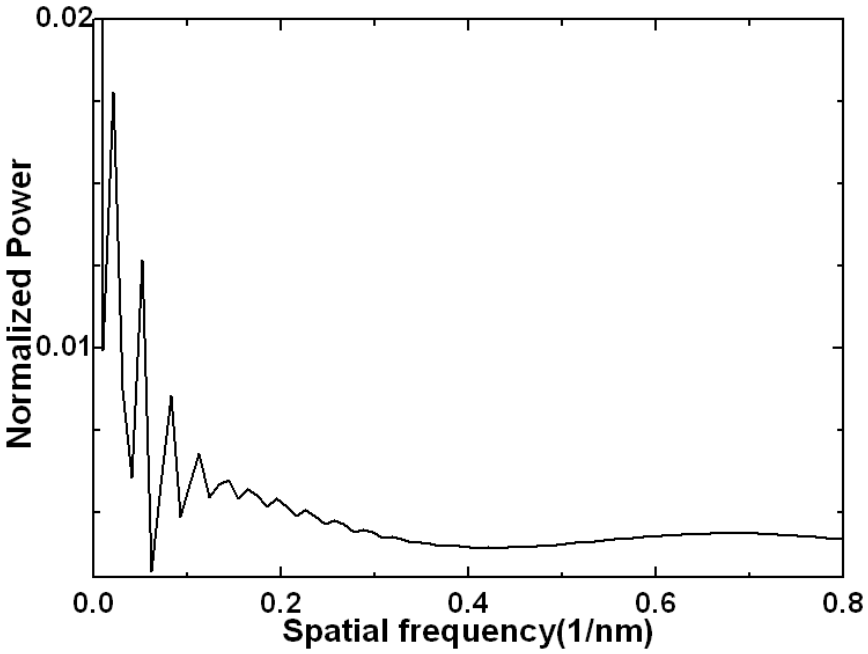


Figure 3.4 Spatial frequency spectrum of the interferometer

In order to determine the number and power distribution of the interference modes, the wavelength spectrum in Figure 3.3 was Fourier transformed to obtain the spatial frequency of the interference fringes, as shown in Figure 3.4. It can be seen that more than three cladding modes are excited, and the power is mainly distributed in the lower order core mode and the dominated cladding mode. If just considering the interference of the core

mode and dominated cladding mode, for the MMI in case of no pump power, its phase $\varphi_{un}$ at the output ( $z = L$ ) can be expressed as,

$$\varphi_{un} = \frac{2\pi}{\lambda}[n_{co}L - \int_0^L n_{cl}(\mathrm{z})dz] \ , \tag{3.1}$$

where $n_{co}$ and $n_{cl}(\mathrm{z})$ are the effective RIs of the core mode and cladding mode, respectively, $n_{cl}(\mathrm{z})$ is position dependent. During the flame heating, although the dopants are slightly diffused outside the fiber core, the remaining active dopants in the core are still high enough to guide the core mode. Hence, we can consider the effective RI of the core mode to be a constant.

Since the EYPF has a high absorption and gain efficiency in the fiber core, the RI could be changed by introducing an optical pump according to the Kramers-Kronig theory. The pump induced RI variation leads to a phase shift $\varphi_p$ of the MMI. As the pump power is more than the transparency power $P_s$ at which the gain is exactly zero, the induced phase of the MMI can be given by [51],

$$\varphi_p = \frac{2\pi}{\lambda}\int_0^L n_p(\mathrm{z})dz = \frac{2\pi}{\lambda}\int_0^L \frac{n_{eff\,2} - n_{eff\,1}}{1 + p_s / p(\mathrm{z})}dz \ , \tag{3.2}$$

where $n_{eff\,2}$ and $n_{eff\,1}$ are the effective RIs of the fiber core as all electrons are in excited state and ground state, respectively, $p(\mathrm{z})$ is the pump power along the fiber and it is position dependent, $n_p(\mathrm{z}) = \dfrac{n_{eff\,2} - n_{eff\,1}}{1 + p_s / p(\mathrm{z})}$ is the pump

induced RI at position z. C. Thirstrup et al [49] have shown that the pump induced RI in the Er-doped fiber (EDF) at wavelength on the long wavelength side decreases with the increase of the pump power. H.Garcia et al [50] also further demonstrated that the pump induced RIs in the EDF and Yb-doped fiber decrease accordingly with the increase of the pump power due to the decreased self-phase modulation effect. Hence, the pump induced RI in the EYPF should decrease accordingly with the increase of the pump power, and $\varphi_p$ decrease accordingly with the increase of the pump power. This leads to the red shift of the transmission spectrum of the MMI.

Besides the above pump induced phase variation, the pump induced heating effect on the core refractive index also contributes to the phase variation of the MMI. It can be expressed as，

$$\varphi_h = \frac{2\pi}{\lambda}\int_0^L n_h(\mathrm{z})dz\,, \tag{3.3}$$

where $n_h(\mathrm{z})$ is the RI variation due to the pump induced heating in the doped fiber, and it is position dependent and related to the pump power and the material absorption and dispersion characteristics of the doped fiber. Hence, as the pump is launched into the MMI, its overall phase can be given by

$$\varphi = \varphi_{un} - \varphi_p + \varphi_h\,. \tag{3.4}$$

Under the pump, the MMI experiences a corresponding phase decrease of $\varphi_p$. This can compensate its phase enlargement due to the ambient temperature increase.

As the phase satisfies the condition of $\varphi = (2k+1)\pi$ , where $k$ is the interference order, the dip wavelength resonance $\lambda$ occurs and can be given by

$$\begin{aligned}\lambda &= \frac{2}{(2k+1)}\int_0^L (n_{co}\text{-}n_{cl}(\mathrm{z})\text{-}n_p(\mathrm{z}) + n_h(\mathrm{z}))dz \\ &= \frac{2}{(2k+1)}[n_{co} - \overline{n}_{cl}\text{-}\overline{n}_p + \overline{n}_h]L\end{aligned}, \tag{3.5}$$

here setting $\int_0^L n_{cl}(\mathrm{z})dz = \overline{n}_{cl}L$ , $\int_0^L n_p(\mathrm{z})dz = \overline{n}_p L$, and $\int_0^L n_h(\mathrm{z})dz = \overline{n}_h L$, where $\overline{n}_{cl}, \overline{n}_p$ and $\overline{n}_h$ are the averagely effective RIs of the cladding mode, pump induced RI, and heat induced RI due to the pump, respectively. The wavelength shift $\Delta\lambda$ of the resonance dip $\lambda_p$ due to the ambient temperature variation $\Delta T$ can be expressed as,

$$\Delta\lambda_p = \frac{2[\alpha(n_{co} - \overline{n}_{cl} - \overline{n}_p + \overline{n}_h) + (\xi_{co} - \xi_{cL}\text{-}\xi_p + \xi_h)L]\lambda_p \Delta T}{(2k+1)}, \tag{3.6}$$

where $\alpha = \frac{1}{L}\frac{dL}{dT}$ is the thermal-expansion coefficient of the MMI, $\xi_{co} = \frac{1}{n_{co}}\frac{dn_{co}}{dT}$ , $\xi_{cl} = \frac{1}{\overline{n}_{cl}}\frac{d\overline{n}_{cl}}{dT}$ , $\xi_p = \frac{1}{\overline{n}_p}\frac{d\overline{n}_p}{dT}$ , and $\xi_h = \frac{1}{\overline{n}_h}\frac{d\overline{n}_h}{dT}$ are the thermal-optic coefficients of the core mode, cladding mode, pump induced RI

variation, and heat induced RI variation due to the pump, respectively. Without the pump, the wavelength shift $\Delta\lambda_{un}$ of the resonance dip $\lambda_{un}$ due to the ambient temperature variation can be given by,

$$\Delta\lambda_{un} = \frac{2[\alpha(n_{co} - \overline{n}_{cl}) + (\xi_{co} - \xi_{cL})L]\lambda_{un}\Delta T}{(2k+1)}. \quad (3.7)$$

According to Eqs.3.6 and 3.7, it can be seen that without the additional pump, the thermal characteristics of the MMI are only related to the thermal-expansion coefficient and the thermal-optic coefficients of the core mode and cladding mode. Once introducing into the additional pump, the thermal characteristics of the MMI are not only related to the above-mentioned common factors but also the thermal-optic coefficients of the pump induced RI variation and heat induced RI variation due to the pump.

## 3.3 Experimental Results and Discussions

The OSA with a 0.01 nm resolution was used to monitor the transmission spectra of the MMI. Experimental results show that under a given temperature, there is almost no wavelength shift if the pump is below 40.73 mW, while corresponding wavelength shift occurs once the pump is above 40.73 mW, and the transmission spectrum of the MMI experiences corresponding red wavelength shift. Moreover, the bigger the pump power is, the more the red shift has. At a temperature of 31.3 °C, under a pump of 42.69 mW, the pump induced red shifts for the left and right transmission dips are 261 pm and 512

pm, respectively, while under a pump of 59.4 mW, the pump induced red shifts for the left and right transmission dips reach 343 pm and 672 pm, respectively.

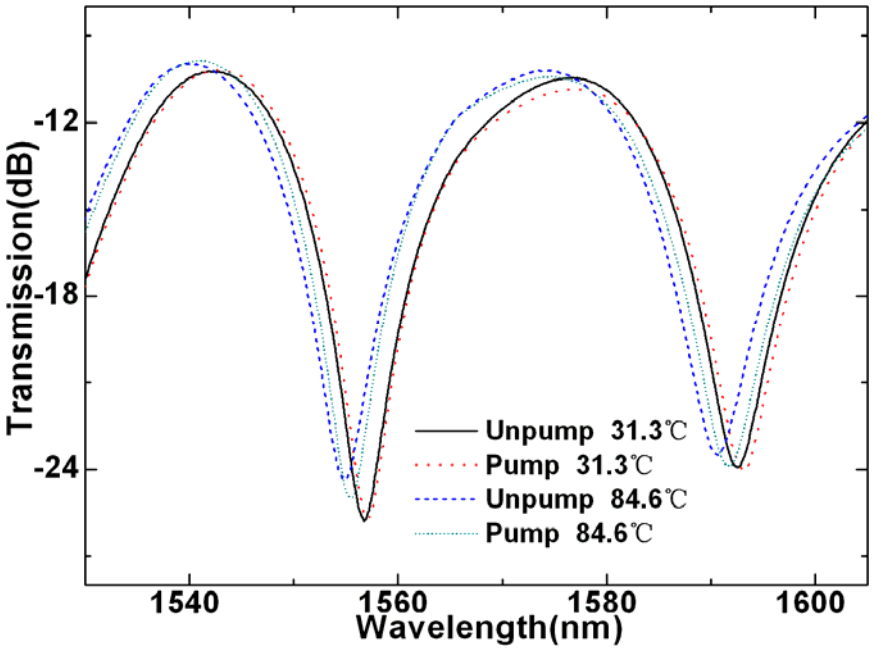


Figure 3.5 Pumped and unpumped transmission spectra under temperatures of 31.3 and 84.6°C, respectively

Since the MMI has corresponding blue shift when ambient temperature increases, the pump induced red shift can compensate the ambient temperature induced blue shift. According to Eq.3.2, a higher pump leads to a bigger phase decrease. Hence, further increasing the pump can let the MMI experience more red shift. This can further compensate the ambient temperature induced blue shift of the MMI. For our experimental setup shown in Figure 3.1, the maximum power of 59.4 mW could be launched into the MMI after the pump passes through a 980/1550 WDM, a 1:99 coupler and a 3dB coupler.

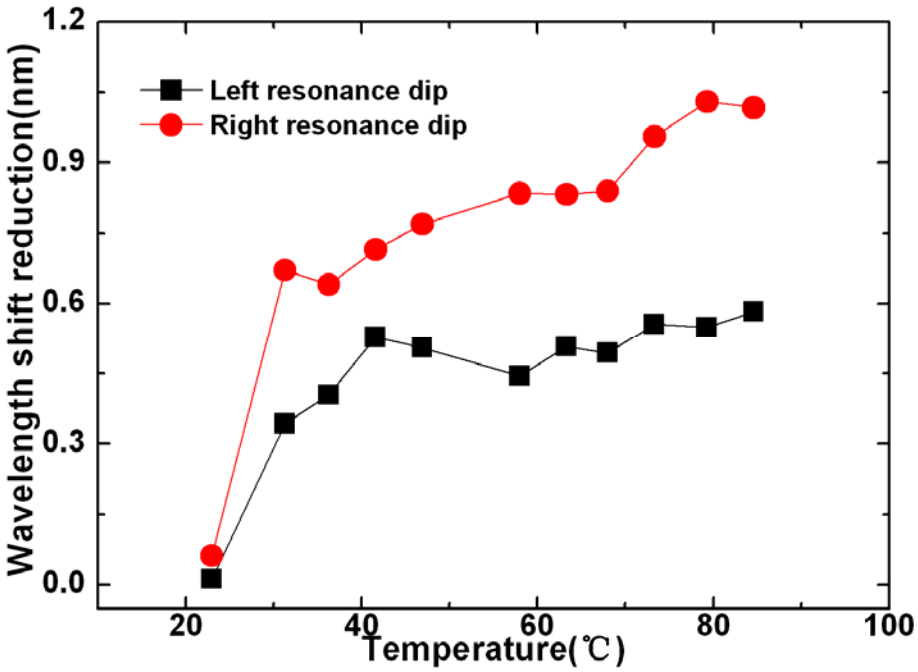


Figure 3.6 Measured wavelength shift reductions of the left and right resonance dips

Figure 3.5 shows its transmission spectral evolution under temperatures of 31.3 and 84.6 °C, respectively. As the temperature increases, the transmission spectrum experiences a corresponding blue shift. Moreover, the pumped MMI experiences a smaller blue shift compared to the unpumped one. Experimental results show that once the 974.3-nm pump is launched into the MMI at a given temperature, compared to the resonance dips without pump, the resonance dips under the pump have a red shift. It means that the pump can reduce the thermally induced blue shift of the MMI. Moreover, there is almost no wavelength shift for the transmission resonance dip under the 59.4-mW pump in a long time. This suggests that the pump induced wavelength shift is mainly determined by the pump induced RI variation.

In general, the wavelength shift reduction enlarges accordingly with the increase of the temperature, as shown in Figure 3.6. As can be seen, at a temperature of 23 °C, the wavelength shift reduction is only 12 pm for the left resonance dip, however, it reaches 583 pm at a temperature of 84.6 °C. The right resonance dip experiences relatively bigger wavelength shift reduction compared to that of the left resonance dip. Its wavelength shift reduction is 63 pm at a temperature of 23 °C while it reaches 1017 pm at a temperature of 84.6 °C.

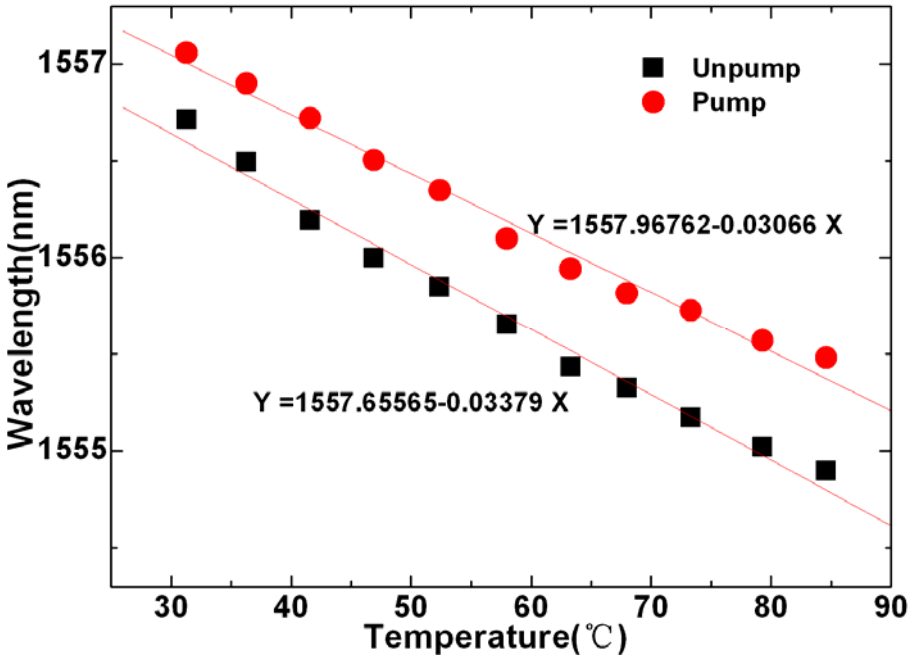


Figure 3.7 Measured relationship between the temperature and the wavelength of the left resonance dip

Figures 3.7 and 3.8 show the measured quasi-linear relationships between the temperature and the wavelength shifts of the left and right resonance dips, respectively. For the left resonance dip, the thermal sensitivities of the pumped

and unpumped MMIs are -30.7 and -33.8 pm/°C, respectively. Due to the pump, 3.1-pm/°C reduction of thermal sensitivity is achieved. For the right resonance dip, the thermal sensitivity of the unpumped MMI is -35.2 pm/°C while it is reduced to -24.9 pm/°C for the pumped MMI. 10.3-pm/°C reduction

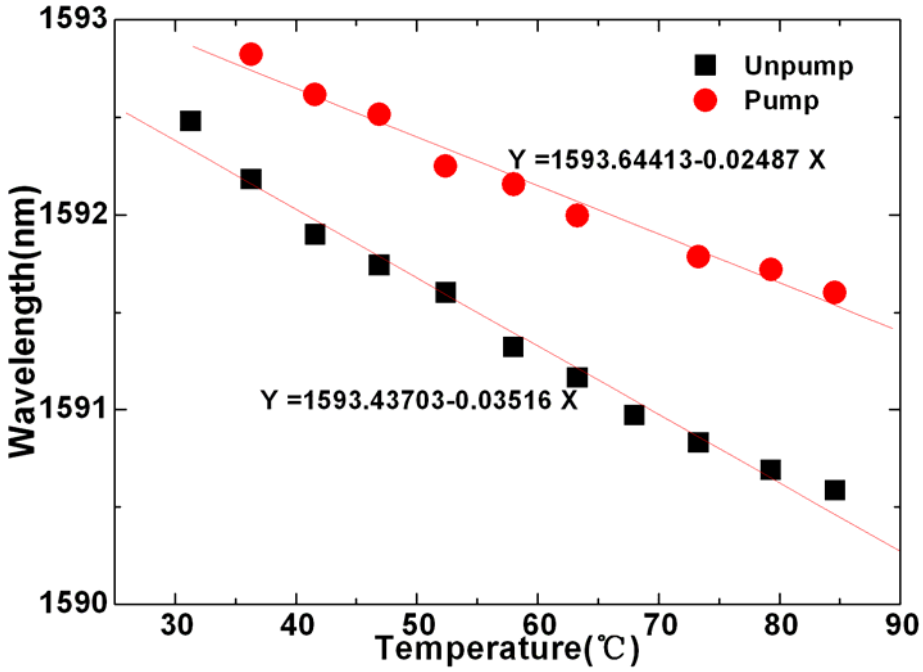


Figure 3.8 Measured relationship between the temperature and the wavelength of the right resonance dip

of thermal sensitivity is achieved. The thermal sensitivity reduction of the resonance dip at the longer wavelength range is 3.3 times bigger than that of the one at the short wavelength range. The above results show that the thermal characteristics of the MMI are intensity and wavelength dependent. In addition, since the other higher order weak cladding modes shown in Figure 3.4 have a modulation function on the interference pattern constructed by the core mode and the dominated cladding mode, they may also contribute to the wavelength

shift difference of the resonance dips in the short and longer wavelength ranges.

## 3.4 Conclusions

In conclusion, in this study, the intensity and wavelength dependent thermal characteristics of the EYPF based MMI have been demonstrated. Without the additional optical pump, it could be used as a high sensitivity temperature sensor. By introducing into an additional optical pump, its thermal sensitivity is reduced. This suggests that its thermal sensitivity could be controlled and its stability could be improved by introducing an additional optical pump. This novel finding may have potential applications for the thermal sensitivity tuning and thermal stability improvement of the EYPF based fiber devices.

# Chapter 4

# High ER Dual Cladding Modes Fiber Up-Taper MMI

In this chapter, a novel dual cladding modes (DCMs) fiber up-taper MMI with a high ER is proposed and demonstrated. This type of MMI is almost like an LPG-type device, also with a deep resonance dip within C and L bands. Moreover, the fabrication of such device is simple and low cost, with a good reproducibility. Its applications for temperature, strain, RI, micro-displacement, ultrasound, and dual parameters (strain and temperature) measurements are investigated theoretically and experimentally.

## 4.1 Introduction

Compared to the fiber down-taper MMIs, the fiber up-taper MMIs are more robust since the fiber down-taper MMIs are more fragile. An MMF based fiber

up-taper MMI was proposed in 2014 [27], but this type of MMI had to adopt the MMF with a step-index profile. It should be noted that it is difficult to fabricate a high ER up-taper MMI on the common SMF since its RI contrast between the core and cladding is small. In 2012, a fiber bitaper based MMI with waist enlarged diameter was proposed [28]. However, the maximum ER of the MMI is lower than 18 dB, and it has many resonance dips within C and L bands. Hence, it cannot serve as an LPG-type device. Moreover, to fabricate this device, a manual splicing method has to be applied. Hence, its fabrication reproducibility is not good.

In this study, a novel DCMs fiber up-taper MMI with a high ER is proposed and demonstrated. It consists of two fiber fusion up-tapers formed in series along one same SMF. It is almost like an LPG-type device, also with a deep resonance dip within C and L bands. It can be fabricated automatically by setting an enlarged “overlap” parameter of a commercial splicer. The maximum ER of this MMI can reach 27.7 dB. This type of interferometer shows a high thermal sensitivity. Moreover, it has opposite wavelength shift trends in response to temperature and strain. Hence, when it is used as a strain or acoustic sensor, the temperature influence can be compensated by applying a pre-strain. Since the two cladding modes in the MMI show different thermal and strain sensitivities, a mode division multiplexing (MDM) method can be used to realize simultaneous temperature and strain measurement with high measurement resolutions. By embedding this MMI into a cured carbon fiber

composites (CCFC) based beam, it can be used as an intensity-modulated micro-displacement sensor with a high sensitivity. Its temperature-cross issue can be solved by applying a pre-displacement since there are opposite ER variation trends in response to displacement and temperature. Due to its simultaneous responses to the acoustic pressure in wavelength shift and intermodal power coupling change, it can be used as an intensity-modulated fiber acoustic sensor (FAS) with an ultrahigh sensitivity.

## 4.2 Theoretical Simulation

The schematic structure of the proposed MMI is shown in Figure 4.1. It is made up of two cascaded fiber up-tapers along one same SMF. The inset in Figure 4.1 shows the photograph of the typical fiber up-taper. The light propagation in the MMI was simulated by using the BPM method. The LP01 mode of the SMF at wavelength 1550 nm was used as the input optical field. Setting the RIs of the fiber core, fiber cladding and air to 1.45205, 1.44681 and 1, respectively, before the light propagates to the first up-taper, only the core mode propagates along the core of the fiber. When the light propagates to the first fiber up-taper, the cladding modes are effectively excited in the fiber cladding. After the core and cladding modes meet at the second fiber up-taper, corresponding intermodal interferences occur, as show in Figure 4.2. Figure 4.3 shows its light mode propagation status when the light propagates

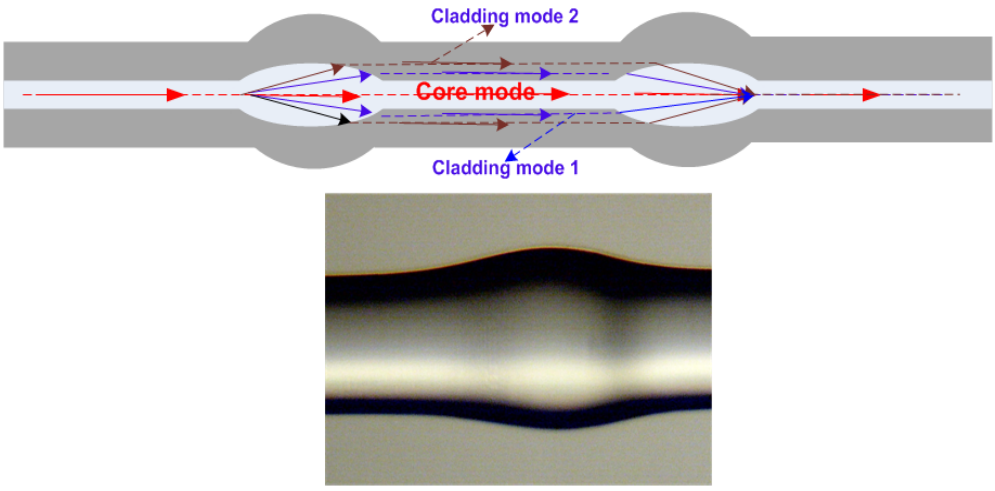


Figure 4.1 Schematic structure of the fiber up-taper MMI

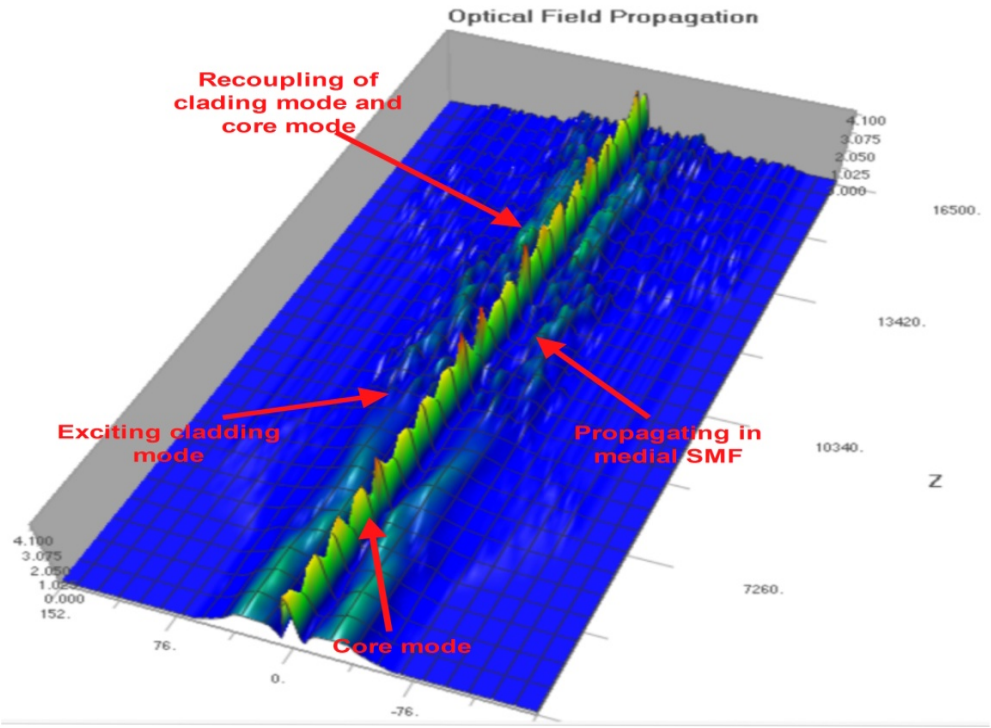


Figure 4.2 Amplitude distribution of the optical field propagating in the MMI

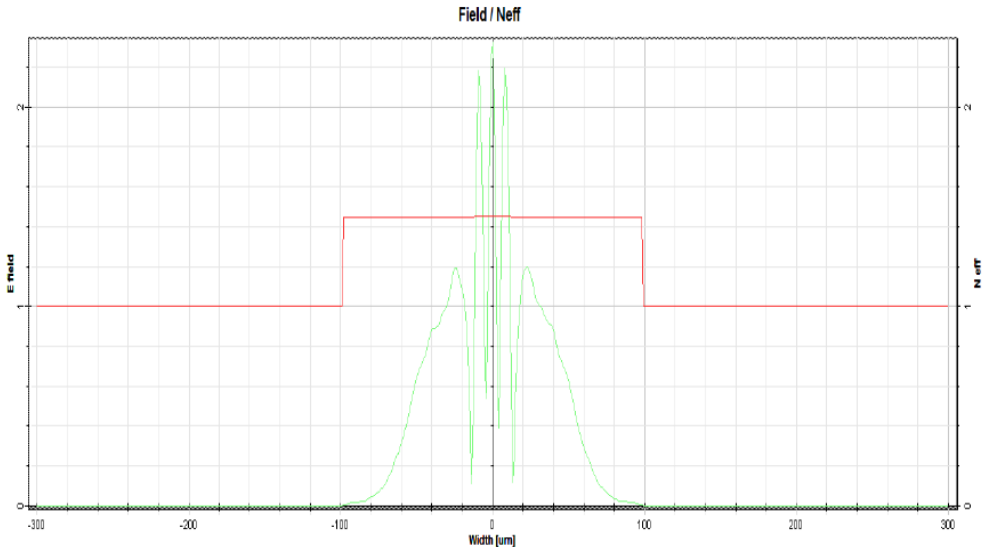


Figure 4.3 Excited cladding modes when the light propagates to the first fiber up-taper

to the first fiber up-taper. It can be seen that one strong cladding mode and the other weak one are excited at the output of the first fiber up-taper simultaneously, and they are corresponding to the cladding modes 1 and 2 shown in Figure 4.1. When they propagate to the second fiber up-taper, they recouple with the core mode to construct core-cladding mode interferences.

## 4.3 Principle of Operation

Its RI and temperature sensing principles are the same to those of the fiber down-taper MMI in Eqs.2.5 and 2.8. When a longitudinal strain is applied to the MMI, its transmission spectrum has a corresponding wavelength shift. Since the core and cladding modes propagate in different waveguide structures of the MMI, the strain affects the two modes in different manner. The effective photo-elastic constants of the core and cladding modes are denoted

by $p_{co}$ and $p_{cl}$, respectively, the strain induced effective RI variation can be given by

$$\Delta(n_{co} - \overline{n}_{cl}) = (P_{co} n_{co} - P_{cl} \overline{n}_{cl})\varepsilon \,, \tag{4.1}$$

and the strain induced length variation of the MMI can be given by

$$\Delta L = L\varepsilon \,. \tag{4.2}$$

Hence, the dip wavelength shift $\Delta\lambda_{dt}$ due to the applied strain can be given by,

$$\frac{\Delta\lambda_{d\varepsilon}}{\lambda_d} = (1 + P_e)\varepsilon, \tag{4.3}$$

where $P_e = \frac{P_{co} n_{co} - P_{cl} \overline{n}_{cl}}{n_{co} - \overline{n}_{cl}}$, is a constant that describes the strain-induced variation of the effective RI difference of the two modes.

## 4.4 Fabrication of the MMI

The interferometer was fabricated by a commercial fiber splicer (Fujikura FSM-40S). To excite the DCMs, a strong cladding mode and a weak cladding mode, the "overlap" parameter of the splicer is enlarged while the other parameters, such as discharge power, duration time, gap, etc, are set to be default. Repeat experiment results show that if setting the "overlap" parameter to around "265," the two cladding modes can be effectively excited, and the

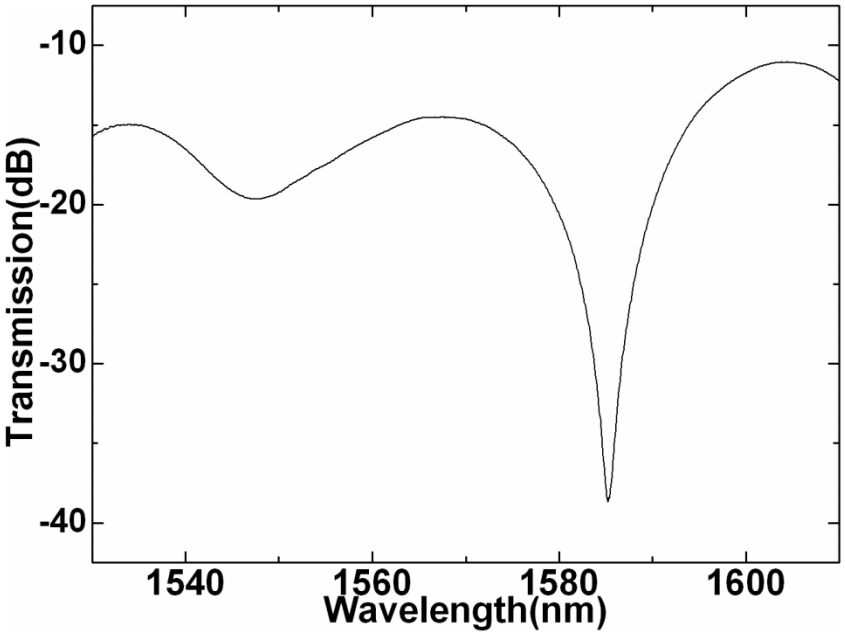


Figure 4.4 Transmission spectrum of sample 1

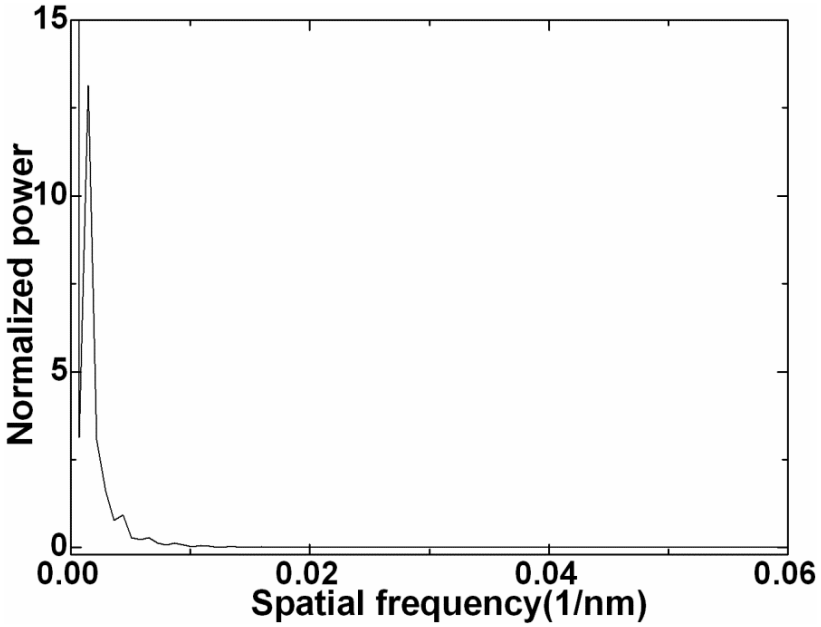


Figure 4.5 Spatial frequency spectrum of sample 1

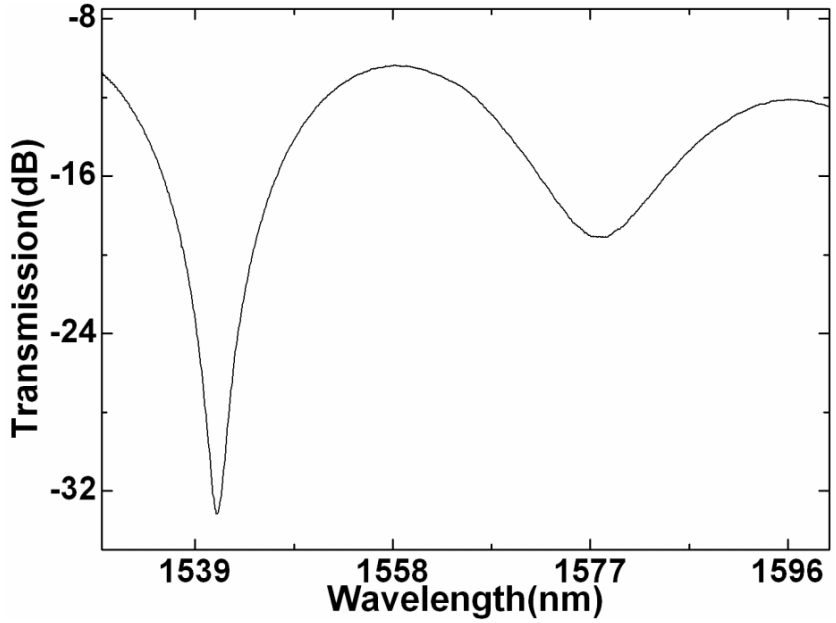


Figure 4.6 Transmission spectrum of sample 2

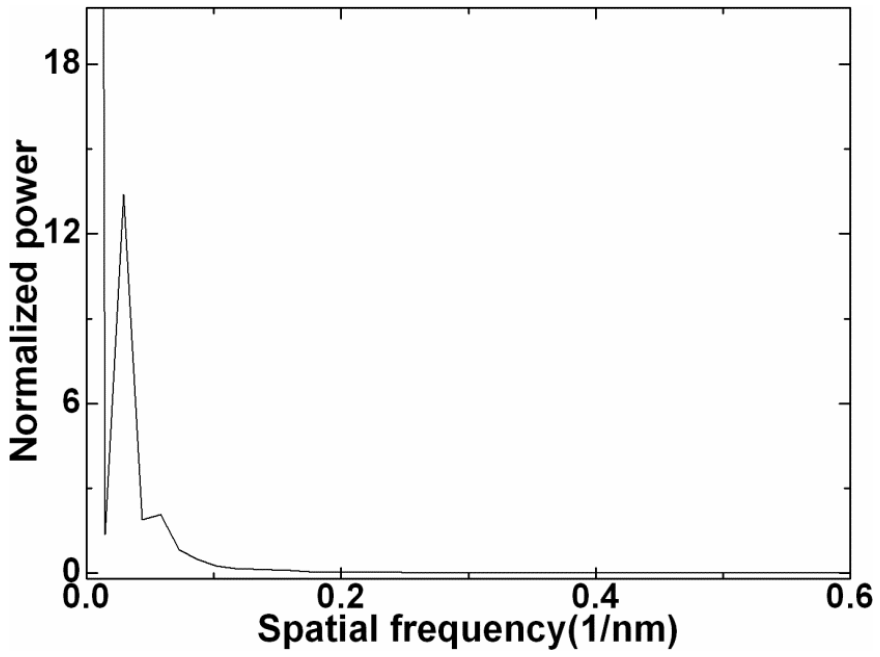


Figure 4.7 Spatial frequency spectrum of sample 2

two fiber up-tapers have near identical maximum waist diameters and lengths of the expanded sections of about 168 μm and 245 μm. Figures 4.4 and 4.6 show the typical transmission spectra of the 2-cm MMIs with the maximum ERs of 27.7 and 22.81 dB, respectively, and Figures 4.5 and 4.7 show their corresponding spatial frequency spectra. As can be seen, one dominate cladding mode and a weak high order cladding mode are excited simultaneously. The interference pattern is mainly constructed by the core mode and the dominated cladding mode, the other weak cladding mode has a modulation function on the interference pattern. This will lead to a transmission spectrum almost like that of the LPG. Repeated experimental results show that for the interference patterns of the MMIs, one deepest resonance dip always occurs in the longer wavelength range or short wavelength range, which is dependent on the symmetrical status of the two fiber-up tapers.

## 4.5 MDM in the MMI for Dual Parameters Measurement

### 4.5.1 Introduction

Dual parameters (temperature and strain) measurement has attracted much attention. Most of the techniques are based on two fiber devices with different sensitivities in response to strain and temperature, such as two different FBGs

[53,54]; an FBG combined with a long period grating (LPG) [55], a polarization maintaining fiber loop mirror (PMFLM) [56], an MMF based interferometer [57], or a PCF based inter-modal interferometer [48]; and a PMFLM combined with an LPG [58], other different types of PMF [59,60], or a temperature compensated PMFLM [13]. The solutions with two fiber devices generally have a large footprint, which limits their practical applications since they tend to be disturbed by ambient environment. Our group has proposed to excite cladding modes in the PMFLMs [61,62] for simultaneous strain and temperature measurement, but to construct a PMFLM, besides a longer PMF, other components, such as a 3-dB coupler and a polarization controller, generally have to be applied, which leads to its complex structure and high cost. Hence, it is more desirable to have just one small and compact sensor for dual parameters measurement with high measurement resolutions. Some techniques based on one specially designed fiber device, such as an FBG written in a splice point between two different types of fibers [63,64], a tilted FBG [65], and a superstructure FBG [66], have been proposed. However, complicated fabrication techniques have to be adopted to fabricate them, which leads to their high cost.

In this study, a novel scheme for simultaneous strain and temperature measurement by MDM in a DCMs fiber up-taper MMI is proposed. The DCMs MMI has a strong cladding mode and a weak cladding mode. Based on a wavelength-referenced method, the temperature and strain resolutions are

only ±1.1 C° and ±54.4 με, respectively. With the MDM method, the two cladding modes in spatial frequency domain are discriminated for simultaneous temperature and strain measurement, with the higher measurement resolutions of ±0.05 C° and ±3.14 με, which are much higher than those of the other proposed dual parameters (temperature and strain) measurement solutions.

## 4.5.2 Principle of Operation

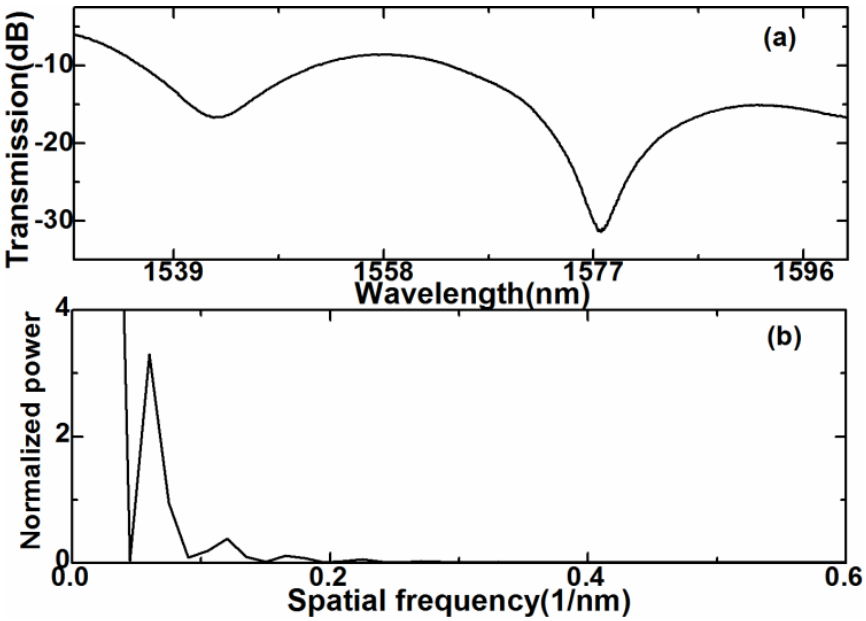


Figure 4.8 (a) Transmission spectrum of the interferometer and (b) its corresponding spatial frequency spectrum

Figures 4.8 (a) and (b) show the typical transmission spectrum of the interferometer and its corresponding spatial frequency spectrum. The MMI has the length of 2 cm. As can be seen from Figure 4.8 (b), one dominant cladding mode and a weak cladding mode are excited simultaneously. This

enables a strong interference pattern with an ER of 22.86 dB, and a weak one with an ER of 8.24 dB, as shown in Figure 4.8 (a). As we all know, for the two-mode fiber interferometers, their transmission resonance dips generally have almost the same strain and thermal sensitivities. Hence, when they are used for dual parameters measurement, the measurement resolutions are very low. For the DCMs fiber interferometer, due to the contribution of the two cladding modes, the interference pattern has one deep resonance dip and the other shallow one, which may be useful for improving the dual parameters measurement resolutions for the wavelength-referenced method. However, for the wavelength-reference method, it is difficult to discriminate the temperature sensitivity difference of the two cladding modes, as well as the strain sensitivity difference.

It can be seen from Figure 4.8 (b) the two cladding modes have a bigger power difference, which means their propagating positions along the fiber cladding are relatively far, and the dominant cladding mode 1 is more close to the fiber core while the weak cladding mode 2 is farther from the fiber core, as shown in Figure 4.1. Since they propagate in different structures along the fiber cladding, they experience different thermal and strain sensitivities. The farther the two cladding modes, the higher difference in temperature and strain sensitivities is. Hence, an MDM method is better to discriminate the two cladding modes for simultaneous strain and temperature measurement with higher measurement resolutions.

The phase difference between the core mode and *j*-th cladding mode can be given by

$$\varphi_j = \frac{2\pi(n_{co} - n_{cl}^j)L}{\lambda} = \frac{2\pi}{\lambda}\Delta n_{neff}^j L\,, \tag{4.4}$$

where $L$ is the length of the interferometer, $n_{co}$ and $n_{cl}^j$ are the effective RIs of the core and *j*-th cladding modes, respectively, *j*=1,2; and $\Delta n_{eff}^j$ is the effective RI difference between the core mode and *j*-th cladding mode. Since the phase $\varphi$ is a function of wavelength $\lambda$, a Taylor expanding to Eq.4.4 with the central wavelength of $\lambda_0$ and the deviation of $\Delta\lambda = \lambda - \lambda_0$ can be applied. Ignoring the higher order terms, it can be given by

$$\varphi_j = \varphi_0 - \frac{2\pi}{\lambda_0^2}\Delta n_{eff}^j L\Delta\lambda\,. \tag{4.5}$$

Considering the mode dispersion, the modal group RI difference $\Delta m_{eff}^j = \Delta n_{eff}^j - \lambda_0 \frac{\partial \Delta n_{eff}^j}{\partial \lambda}$, Eq.4.5 can be replaced as

$$\varphi_j = \varphi_0 - \frac{2\pi}{\lambda_0^2}\Delta m_{eff}^j L\Delta\lambda\,. \tag{4.6}$$

Its transmission spectrum can be fast Fourier transformed (FFTed) to obtain its spatial frequency spectrum. According to Eq.4.6, we can get its spatial frequency as

$$\xi_j = \frac{1}{\lambda_0^2}\Delta m_{eff}^j L\,. \tag{4.7}$$

As can be seen from Eq.4.7, for the *j*-th cladding mode, it has a corresponding spatial frequency. Hence, the two cladding modes induce two corresponding spatial frequencies. By monitoring the responses of the two spatial frequencies to temperature or strain, the temperature or strain sensitivity difference of the two cladding modes can be discriminated.

### 4.5.3 Experimental Results and Discussions

An unpolarized C and L BBS was used as the optical source. Its transmission spectrum was measured by an OSA. The interferometer was supported by two fiber holders placed on an optical table, with one side mounted directly to an optical table and the other side mounted on a translation stage. The strain was applied by stretching the fiber using the translation stage, and it was controlled in the range of 81.3 to 1626 με with a step of 81.3 με. With the increases of the strain, its transmission spectrum experiences a corresponding blue shift, as shown in Figure 4.9. Figures 4.10 and 4.11 show the measured relationships between the strain and wavelength shift for the right and left dips of the transmission spectrum. There are quasi-linear relationships between the strain and wavelength shift for the right and left dips, with linear R-squares of 0.993 and 0.998, and strain sensitivities of -1.03 and -1.02 pm/με, respectively.

The ambient temperature was changed by a temperature controller, with an inserted digital semiconductor thermometer as a calibrator. It was controlled from 25 C° to 70 C° with a step of 5 C°. With the increase of the temperature,

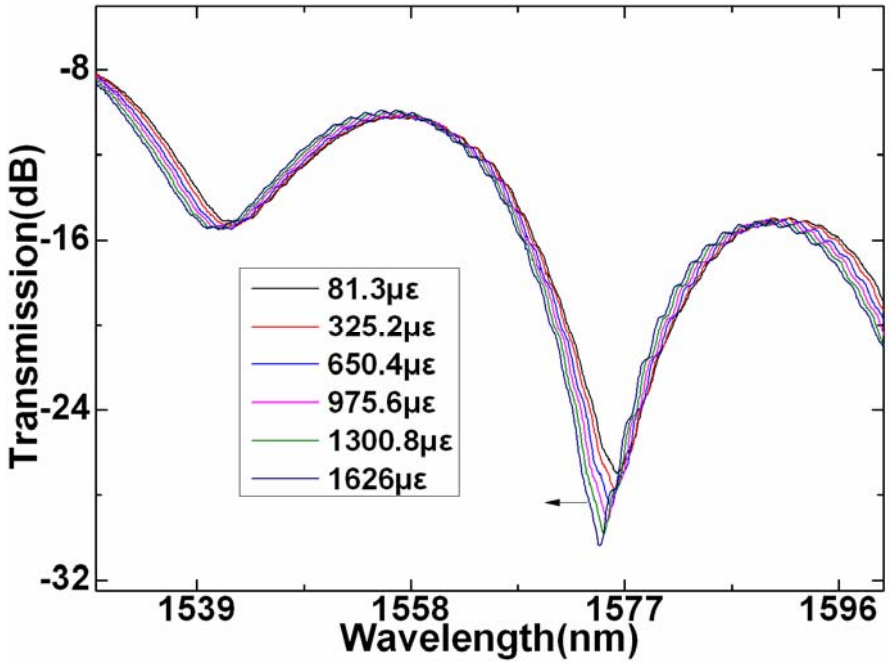


Figure 4.9 Transmission spectral responses to strain

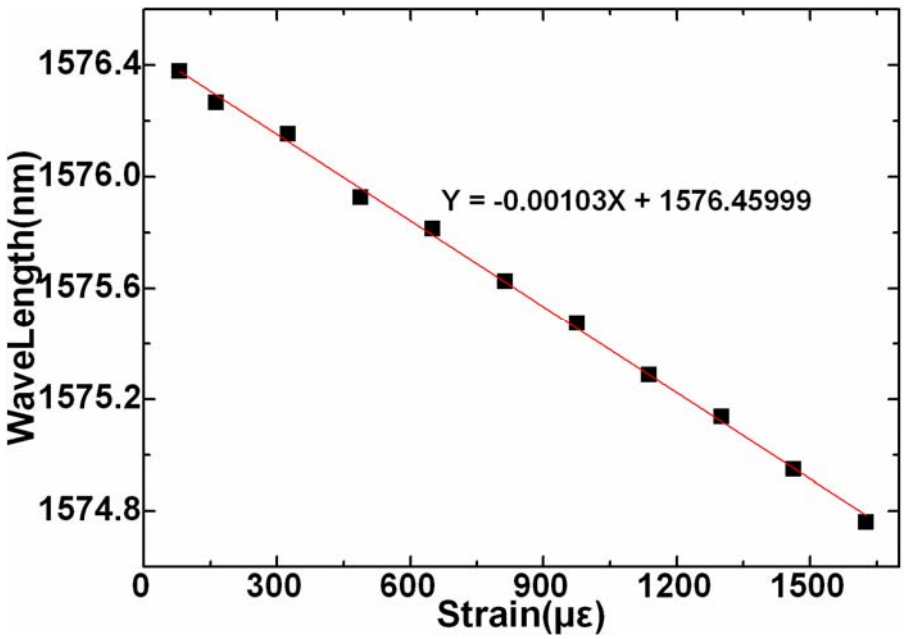


Figure 4.10 Relationship between the strain and the right dip wavelength

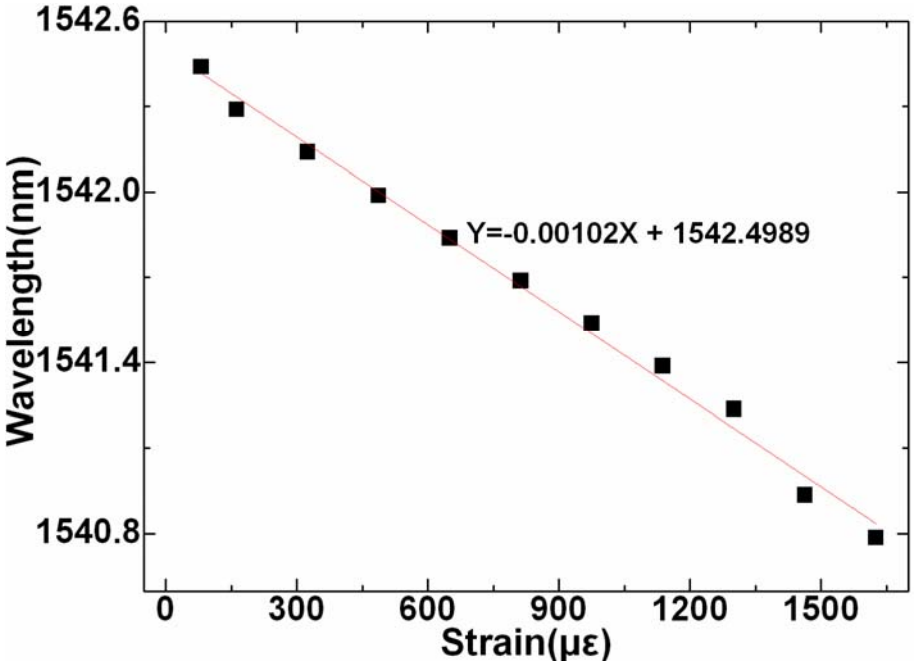


Figure 4.11 Relationship between the strain and the left dip wavelength

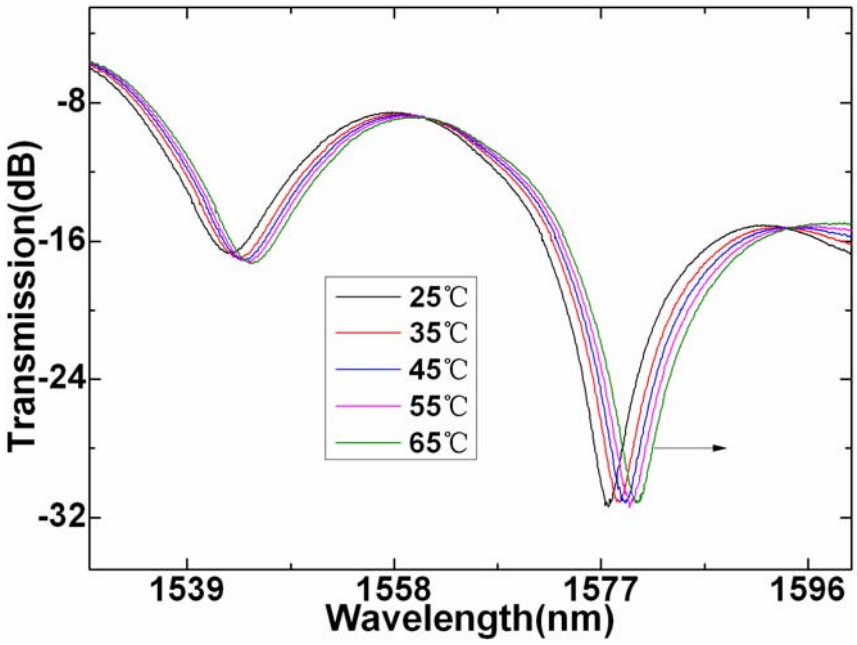


Figure 4.12 Transmission spectral responses to temperature

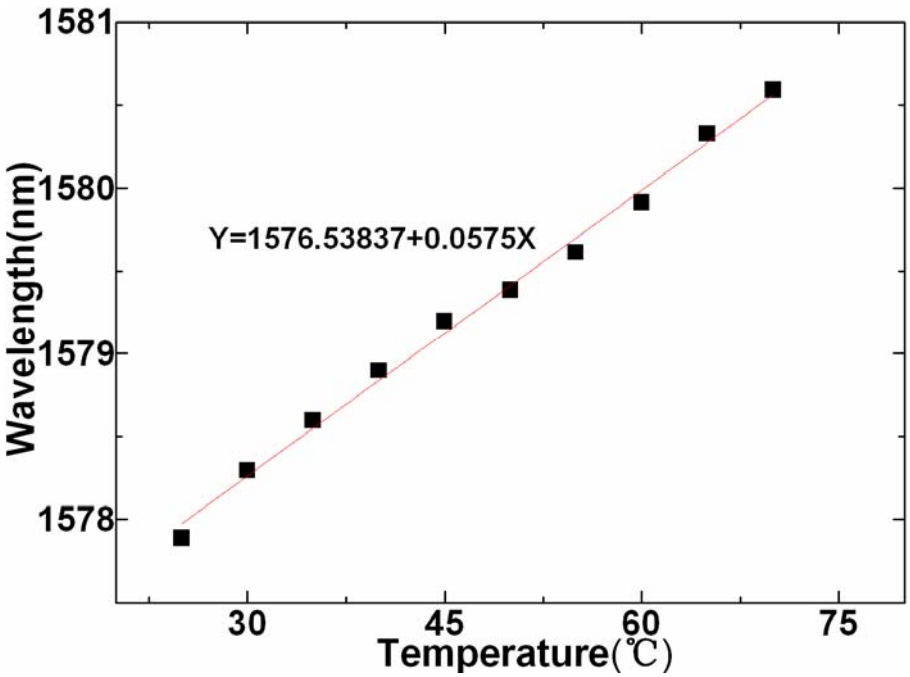


Figure 4.13 Relationship between the temperature and the right dip wavelength

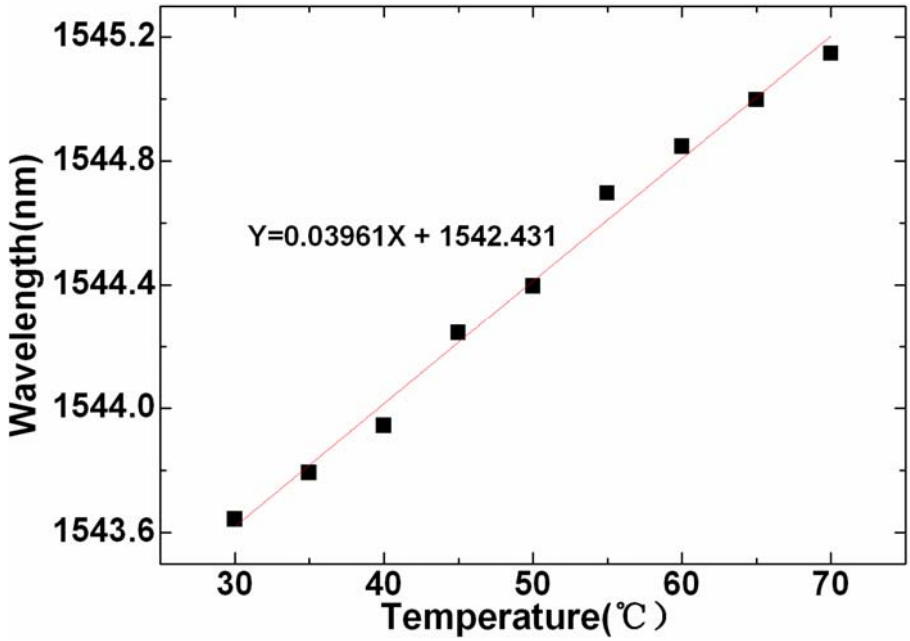


Figure 4.14 Relationship between the temperature and the left dip wavelength

the transmission spectrum experiences a corresponding red shift, as shown in Figure 4.12. There are quasi-linear relationships between the temperature and wavelength shift for the right and left dips, with linear R-squares of 0.991 and 0.9939, as shown in Figures 4.13 and 4.14. As can be seen, the right dip has a higher sensitivity of 57.5 pm/C° while the left dip in the short wavelength range has a lower sensitivity of 39.6 pm/C°.

Based on the above experimental results, the temperature $\Delta T$ and strain $\varepsilon$ measurement matrix for the left and right dips can be given by

$$\begin{bmatrix} \Delta\lambda_L \\ \Delta\lambda_R \end{bmatrix} = \begin{bmatrix} 39.6 & -1.02 \\ 57.5 & -1.03 \end{bmatrix} \begin{bmatrix} \Delta T \\ \varepsilon \end{bmatrix}. \tag{4.8}$$

According to Eq.4.8, the temperature and strain measurement resolutions can be expressed as

$$\begin{bmatrix} \delta(\Delta T) \\ \delta(\varepsilon) \end{bmatrix} = \pm \frac{1}{|17.862|} \begin{bmatrix} |\text{-}1.02| & |\text{-}1.03| \\ |39.6| & |57.5| \end{bmatrix} \begin{bmatrix} |\delta(\Delta\lambda_L)| \\ |\delta(\Delta\lambda_R)| \end{bmatrix}. \tag{4.9}$$

Under a wavelength resolution of 10 pm, the temperature and strain resolutions are ± 1.1C° and ± 54.4με, respectively. As can be seen, the strain measurement resolution is not good. Hence, an MDM method is proposed to realize simultaneous measurement of temperature and strain with higher measurement resolutions.

It should be noted that the measured data of the transmissivity against wavelength can be got in real time via a GPIB interface of the OSA, and they

can be FFTed in real time by a high speed computer. The FFTed data in response to strain are shown in Figure 4.15. Due to the strong and weak cladding modes, a strong spatial frequency (SP1) and a weak SP2 are induced simultaneously. It can be seen that with the increase of the strain, the normalized powers distributed in SP1 and SP2 increase accordingly. There are quasi-linear relationships between the normalized power and strain for SP1 and SP2, with linear R-squares of 0.982 and 0.997, and sensitivities of 0.00042 and 0.00013, respectively, as shown in Figure 4.16. The strain sensitivity of SP1 is 3.2 times bigger than that of SP2.

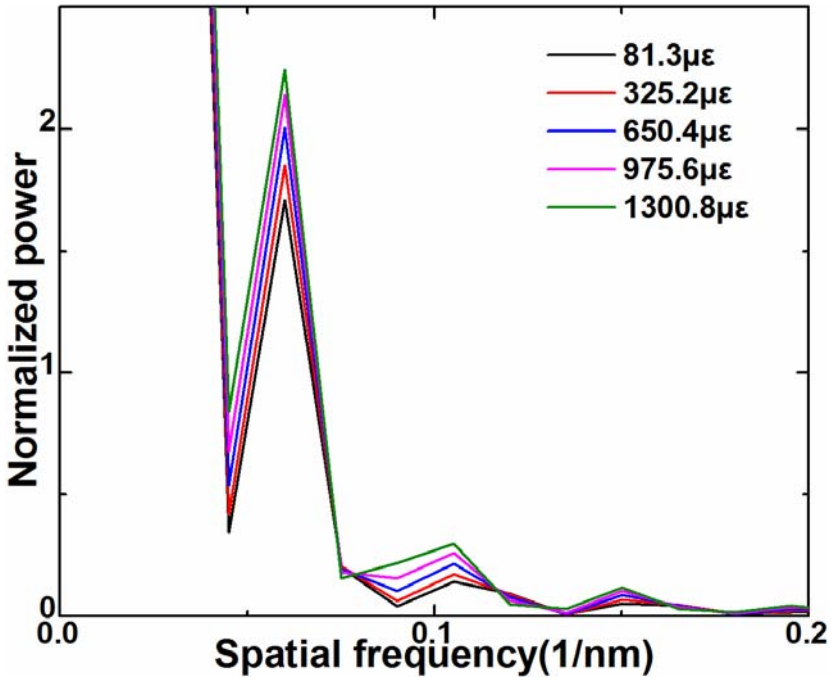


Figure 4.15 Spatial frequency spectral responses to strain

The FFTed data in response to temperature are shown in Figure 4.17. With the increase of the temperature, the normalized powers distributed in SP1

and SP2 decrease quasi-linearly accordingly, with linear R-squares of 0.996 and 0.989, and thermal sensitivities of -0.0304 and -0.0066, as shown in Figure 4.18. The temperature sensitivity of SP1 is 4.6 times bigger than that of SP2. It can be seen that the two cladding modes have a big strain sensitivity

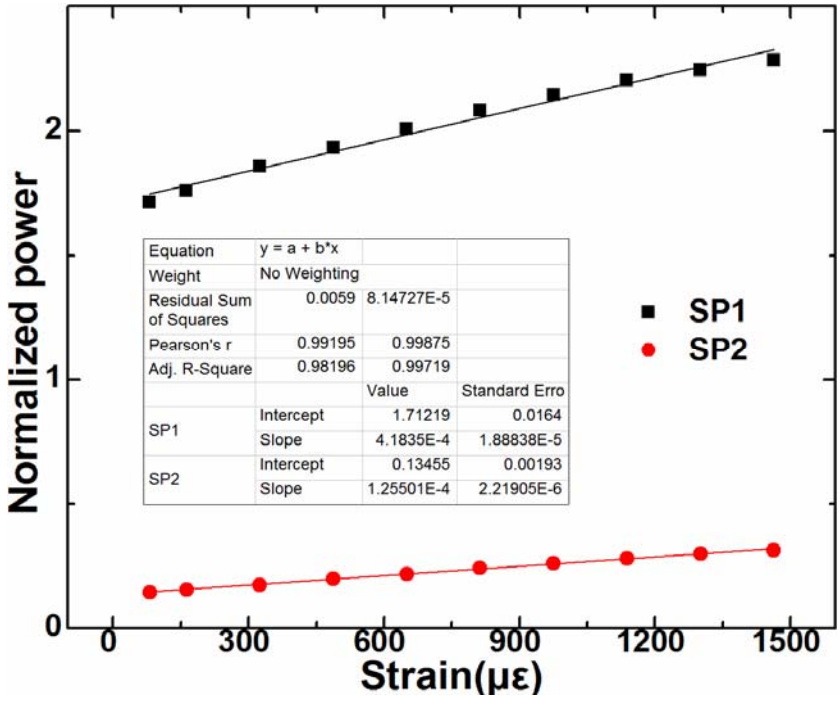


Figure 4.16 Relationship between the strain and the normalized power

difference, as well as a big temperature sensitivity difference. This just agrees to our theoretical predication, the farther their propagation positions along the fiber cladding, the higher the difference in thermal and strain sensitivities is. This is helpful to improve the dual parameters measurement resolutions. Based on the above results, the temperature and strain measurement matrix for SP1 and SP2 can be given by

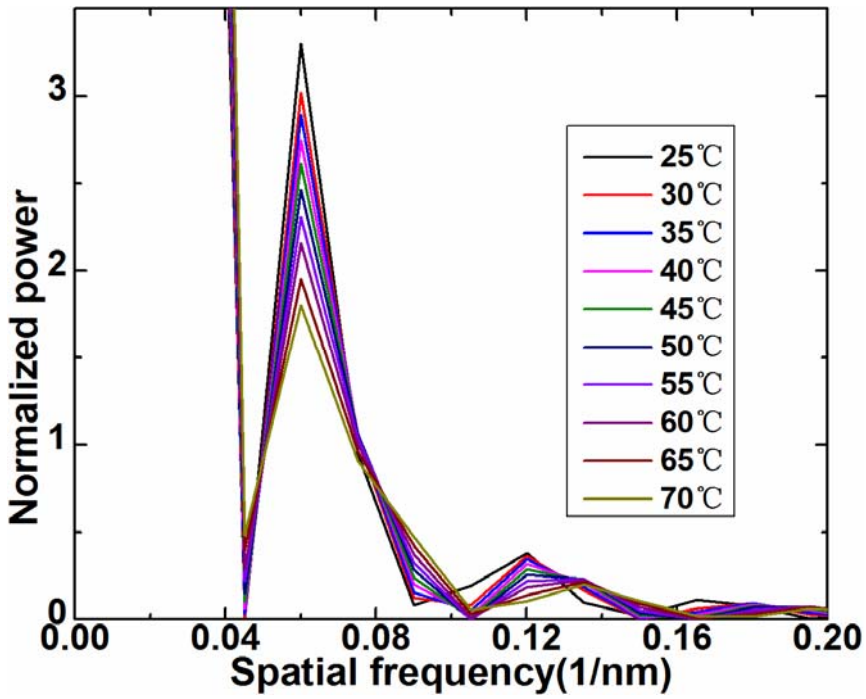


Figure 4.17 Spatial frequency spectral responses to temperature

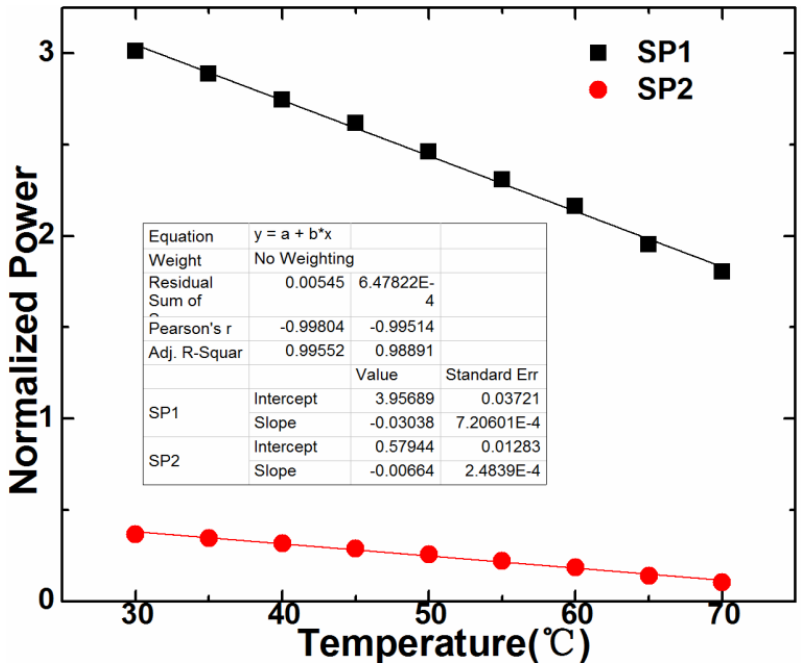


Figure 4.18 Relationship between the temperature and the normalized power

$$\begin{bmatrix} \Delta P_1 \\ \Delta P_2 \end{bmatrix} = \begin{bmatrix} -0.0304 & 0.00042 \\ -0.0066 & 0.00013 \end{bmatrix} \begin{bmatrix} \Delta T \\ \varepsilon \end{bmatrix}. \quad (4.10)$$

According to Eq.4.10, the measurement resolutions of temperature and strain can be expressed as

$$\begin{bmatrix} \delta(\Delta T) \\ \delta(\varepsilon) \end{bmatrix} = \pm \frac{1}{|0.00000118|} \begin{bmatrix} |0.00013| & |0.00042| \\ |-0.0066| & |-0.0304| \end{bmatrix} \begin{bmatrix} |\delta(\Delta P_1)| \\ |\delta(\Delta P_2)| \end{bmatrix}. \quad (4.11)$$

For the MDM method based on the FFTed processing, its data reading error can be corrected to 0.0001. Hence, the temperature and strain resolutions reach ± 0.05 C° and ± 3.14 με, respectively, which are 22 and 17.3 times higher than those of the above wavelength-referenced method, and are distinctively higher than those of the other proposed solutions [13,48,56-66]. It should be noted that the speed of the MDM method is limited by the speed of the computer. For our data processing, a computer with a Core i7-4770 CPU and 8-GB ram was adopted to perform the processing, and the processing speed for each measurement was shorter than 1 second. Hence, real-time digital processing of the measured data is possible with a higher speed computer.

## 4.5.4 Conclusions

In conclusion, MDM in a DCMs fiber interferometer for simultaneous strain and temperature measurement has been demonstrated. With just one DCMs fiber interferometer, dual parameters measurement with higher measurement

resolutions could be achieved. With the MDM method, the temperature and strain resolutions reach ±0.05 C° and ±3.14 με, respectively, and are much higher than those of the other dual parameters measurement solutions. The proposed DCMs fiber interferometer and MDM measurement method are potential to have wide applications in dual parameters measurement field.

## 4.6 Temperature and Strain Sensing Performances of a 1-cm MMI

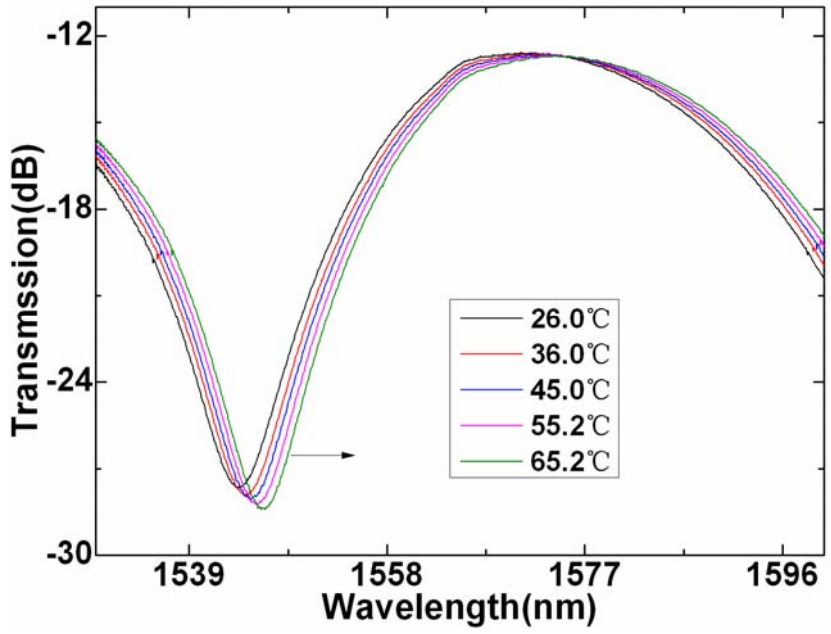


Figure 4.19 Transmission spectral responses to temperature of the 1-cm MMI

The other fiber up-taper MMI, with the length of 1 cm and an ER of 20.85 dB, was also demonstrated for temperature and strain sensing with the above same experimental setup. Its transmission spectrum also experiences a corresponding red shift with the increase of the temperature, as shown in

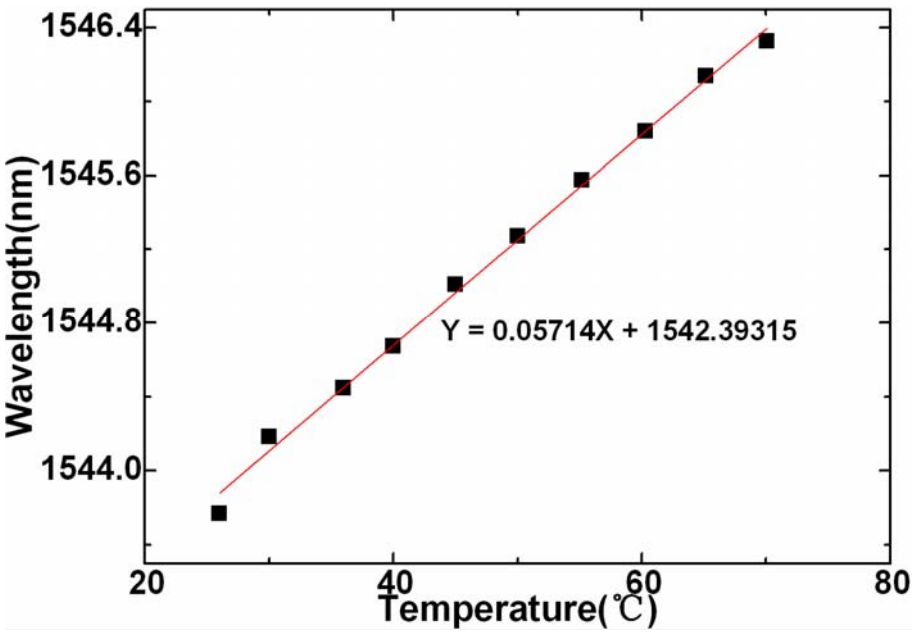


Figure 4.20 Relationship between the temperature and the dip wavelength of the 1-cm MMI

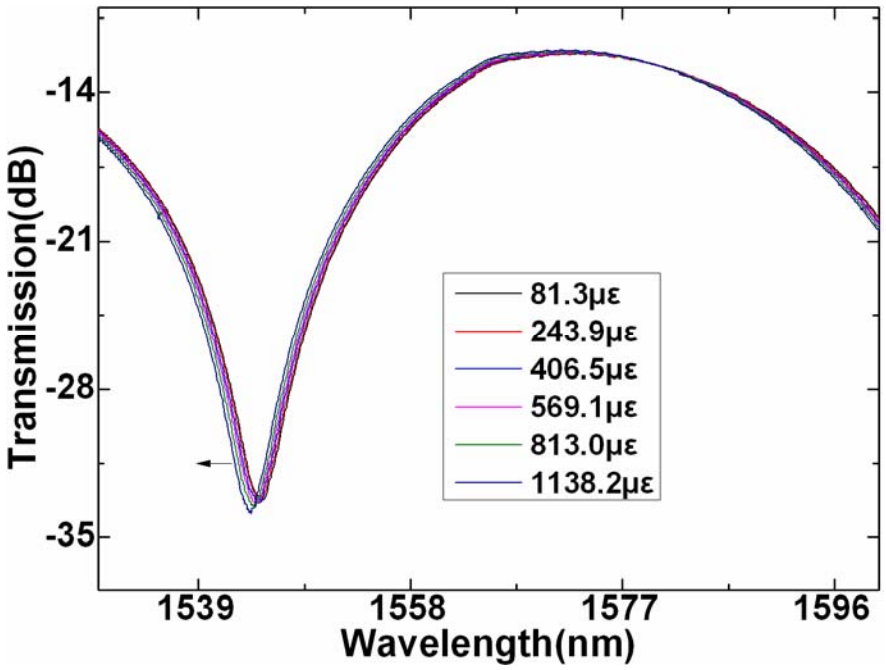


Figure 4.21 Transmission spectral responses to strain of the 1-cm MMI

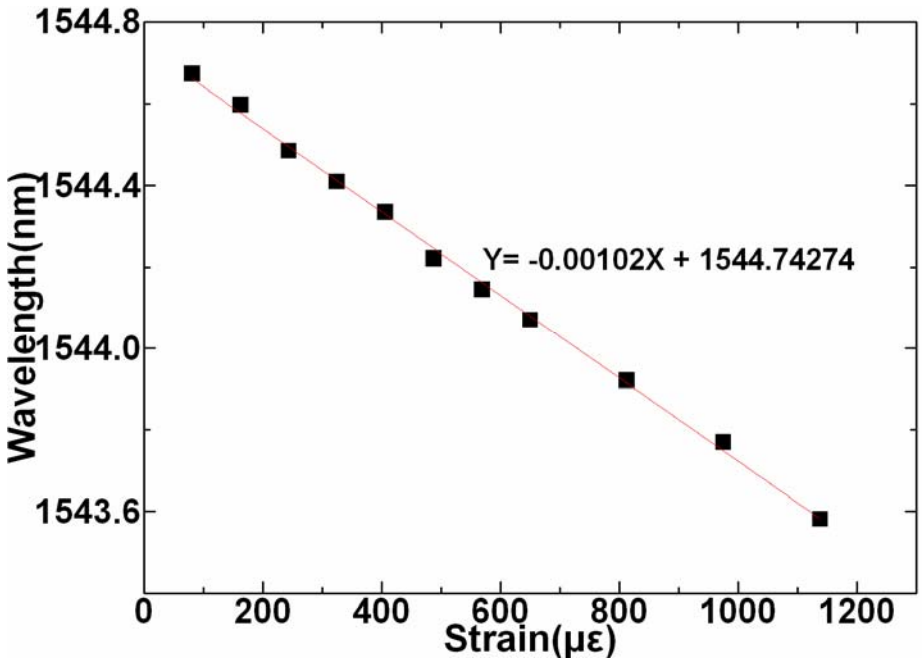


Figure 4.22 Relationship between the strain and the dip wavelength of the 1-cm MMI

Figure 4.19. There is a quasi-linear relationship between the temperature and the wavelength shift with a temperature sensitivity of 57.1 pm/ C° and the linear R-square of 0.9955, as shown in Figure 4.20. Figure 4.21 shows its transmission spectral response to strain. With the increase of the strain, its transmission spectrum also experiences a corresponding blue shift. There is a quasi-linear relationship between the strain and wavelength shift, with a sensitivity of -1.02 pm/με and the linear R-square of 0.998, as shown in Figure 4.22.

Based on the above experimental results, the MMIs with the 2-cm and 1-cm lengths have almost the same temperature and strain sensitivities for the deep resonance dip. As can be seen from the above experimental results, the

resonance dip experiences opposite variation trends in wavelength shift to strain and temperature, hence when the MMI is used as a strain sensor, a pre-strain can be applied to the MMI to compensate for the temperature influence.

## 4.7 RI Sensing of the MMI

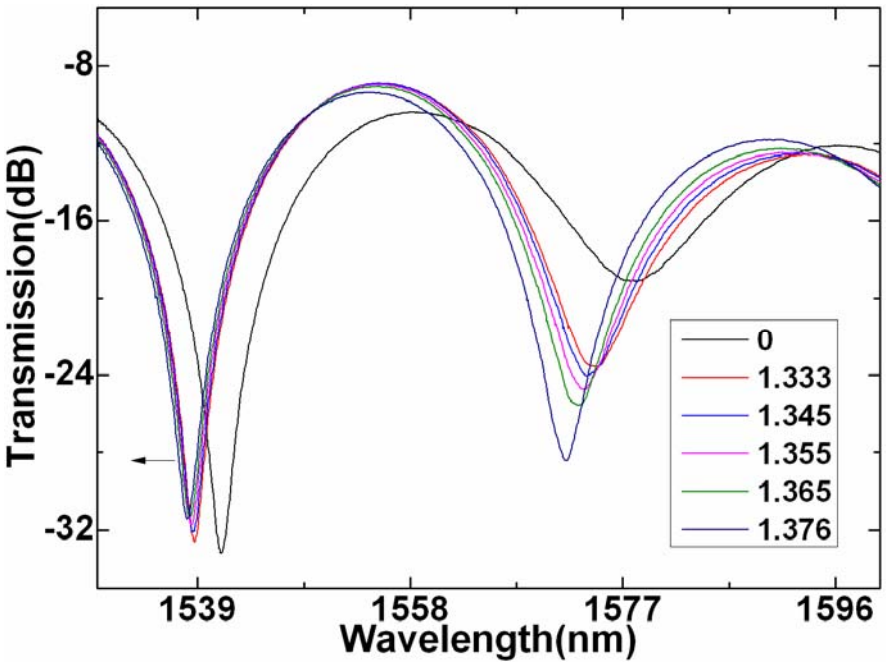


Figure 4.23 Transmission spectral responses to RI

The experimental setup for testing the RI sensing performance of the MMI is based on the above strain experiment setup. The only difference is that a glass plate was put under the MMI contiguously. During the experiment, the MMI was kept straight and tight to prevent the bending influence. The RI solutions were prepared by mixing the water and alcohol. With the RI range of 1.333 to 1.376 with an RI step of 0.005. A commercial refractometer (KEM RA-130)

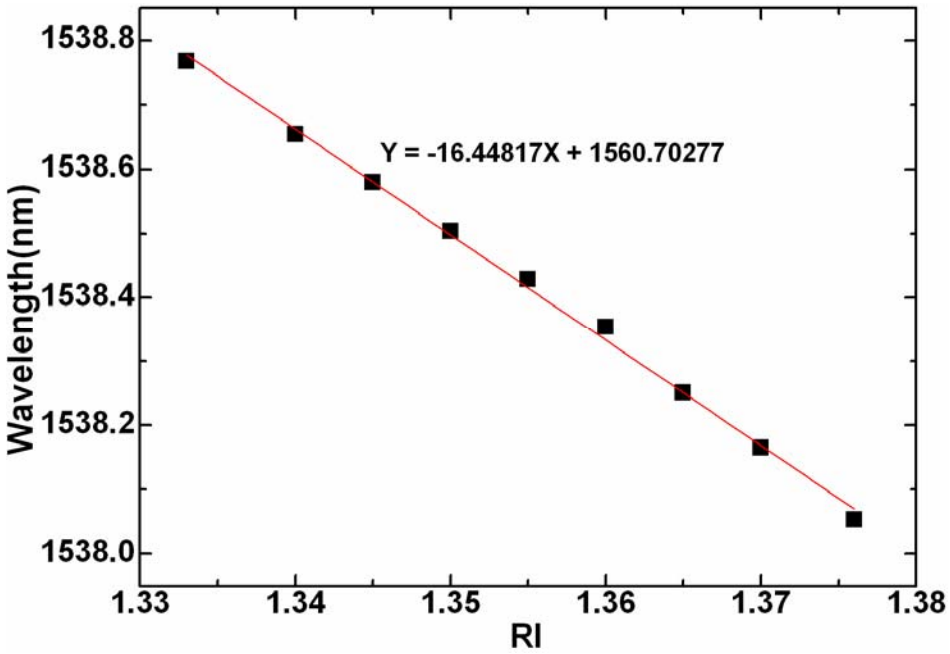


Figure 4.24 Relationship between the RI and the left dip wavelength

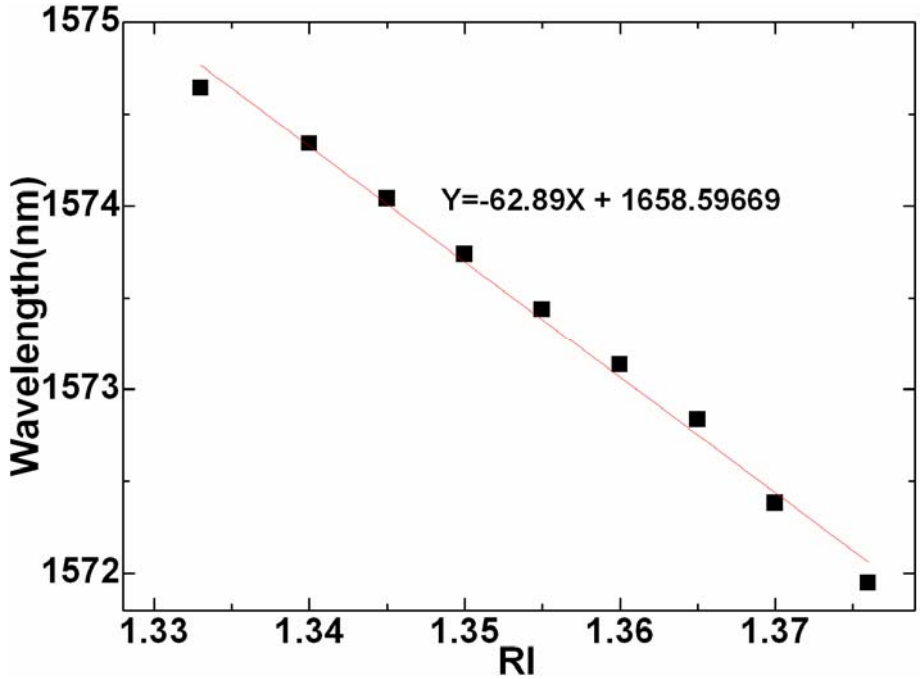


Figure 4.25 Relationship between the RI and the right dip wavelength

with a measurement resolution of 0.001 was used to calibrate the RI values. To achieve the full contact between the MMI and RI solution, we place the

MMI just above the glass plate and completely immerse it in the solution. A 2-cm MMI, with a maximum ER of 22.81 dB, was used to demonstrate its RI sensing performance. With the increase of the RI, its transmission spectrum experiences a corresponding blue shift, as shown in Figure 4.23.

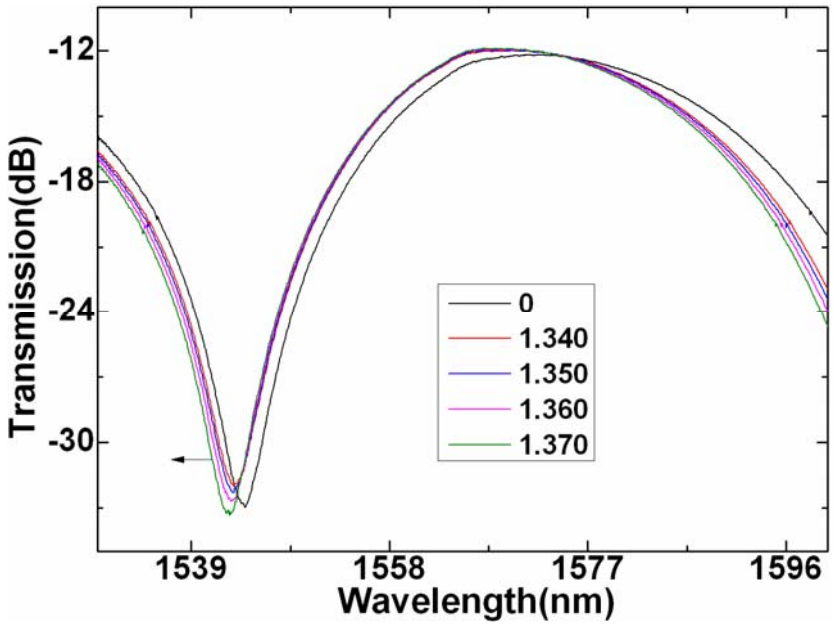


Figure 4.26 Transmission spectral responses to RI of the 1-cm MMI

Figures 4.24 and 4.25 show the measured relationships between the RI and the wavelength shift of the left and right resonance dips. There are quasi-linear relationships between the RI and the wavelength shift with the linear R-squares of 0.9971 and 0.991 for the left and right dips, respectively. However, the sensitivity of right dip in the long wavelength range is -62.89 nm/RIU, and 3.8 times higher than that of the left dip in the short wavelength range of about -16.448 nm/RIU. This shows that the MMI is wavelength dependent on the RI variation. In addition, as can be seen, the interference

pattern is not uniform, this is due to the modulation function of the other high order cladding mode, and it leads to the high RI sensitivity of the MMI in the right dip. The above 1-cm MMI was also used to test the RI sensing performance with the same experimental setup. With the increase of the RI, the transmission spectrum experiences a corresponding blue shift, as shown in Figure 4.26. A quasi-linear relationship between the RI and wavelength shift is obtained with a sensitivity of -23.695 nm/RIU and the linear R-square of 0.9977, as shown in Figure 4.27.

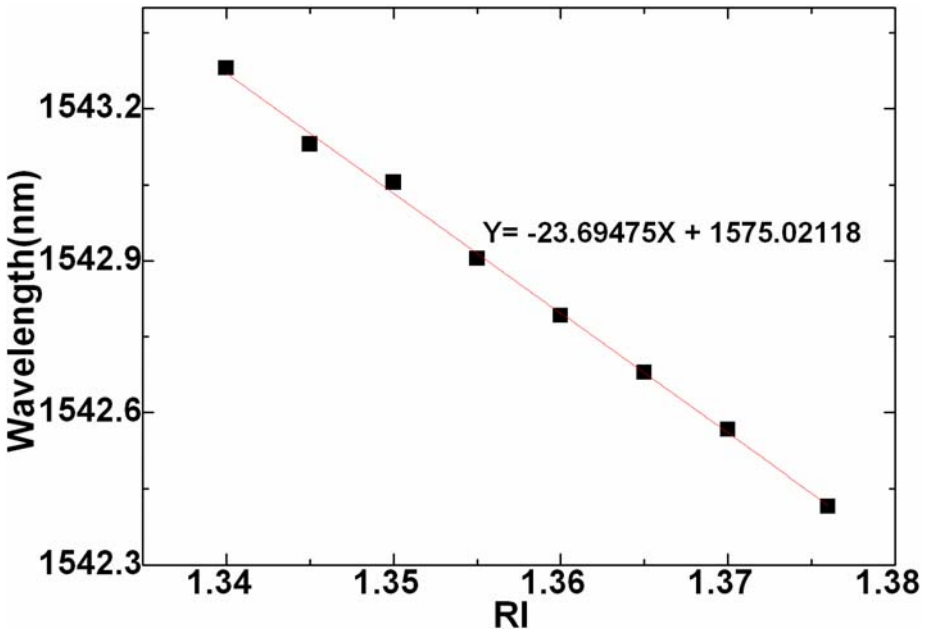


Figure 4.27 Relationship between the RI and the dip wavelength of the 1-cm MMI

According to the above experimental results, the MMI is both RI and temperature sensitive, and there is a big difference for the RI sensitivity with regard to the left and right dips. In addition, according to the experimental

results in section 4.5, the left and right dips of the 2-cm MMI have different temperature sensitivities. Hence, combining the two dips with different RI and temperature sensitivities to a dual parameter measurement matrix, simultaneous measurement of temperature and RI can be achieved.

## 4.8 Micro-Displacement Sensor with the Embedded MMI

### 4.8.1 Introduction

Micro-displacement measurement is a primary requirement for measurement industry. Fiber-optic micro-displacement sensors have attracted much interest due to their inherent advantages, such as immunity to electromagnetic interference and chemical corrosion, light weight, remote sensing ability, good multiplexing capability, etc. To this day, several fiber micro-displacement sensors based on fiber Bragg grating (FBG) [67, 68], long period fiber grating (LPG) [69], high birefringence fiber loop mirror (HBFLM) [47], MMIs based on different fiber structures [70-74], etc, have been proposed. Among them, the use of an FBG has to adopt the specially designed beams to realize temperature and micro-displacement discrimination [67, 68], which leads to a complicated sensing structure and a high price. For the LPG one [69], three LPGs based on a Mach–Zehnder configuration are applied, which leads to a complicated sensor system and high cost. For the HBFLM one, the adopted

HBFLM generally has a large footprint because it is constructed by a 3 dB coupler, a polarization controller, and a section of PMF. Recently, the MMI ones [70-74] have attracted much attention due to their inherent advantages of low cost and compact structure. Among them, most of the MMIs [70-73] have to be introduced into a core-offset splice joint, and even added into the other bowknot taper joint in Refs.[72, 73]. It should be noted that if introducing a core-offset splice joint to the MMI, the polarization characteristics is introduced, which makes the MMI sensor become polarization dependent. This influences the measurement accuracy and stability of the MMI micro-displacement sensor. Moreover, the key issue for the core-offset MMIs is their bad reproducibility. A simple MMI based on a single-mode multimode single-mode fiber structure was proposed in Ref. [74], but to discriminate temperature and displacement, its 3-dB bandwidth needed to be measured, which may induce a data read error for a wide 3-dB bandwidth. Moreover, due to its lower ER, it cannot be used as a low cost intensity-referenced sensor. In addition, to construct such an MMI, a longer multimode fiber is generally needed. This makes the MMI tend to be more sensitive to changes in the ambient environment as compared to a small footprint one.

It should be noted that although the FBG, LPG and HBFLM in Refs.[68–70] were surface mounted on the beams for micro-displacement measurement, but these cannot fully protect them from outer damage. The MMIs in [71-74] are only demonstrated for micro-displacement measurement

with bare fiber structures, hence they are limited for practical applications. Note that when the above fiber-optic devices are used for practical sensors, suitable package material and method have to be applied since any torsion and outer disturbance applied to them influence their measurement accuracy.

In this study, a novel micro-displacement sensor based on an embedded fiber DCMs fiber up-taper MMI is demonstrated. By exciting one dominant cladding mode and one weak cladding mode in the MMI, its ER reaches 27.7 dB and its transmission spectrum has only one very deep resonance dip within C and L bands. With the MMI embedded in a CCFC based beam, it can be used as an intensity-modulated micro-displacement sensor with a high sensitivity. Experimental results show that its ER decreases quasi-linearly with the enlargement of the displacement. Its measurement resolution reaches 4.67 μm, and its dynamic measurement range is within 0~200 Hz. Its temperature cross-sensitivity issue can be solved by applying a corresponding pre-displacement since it has opposite ER variation trends in response to the displacement and temperature.

### 4.8.2 Principle of Operation

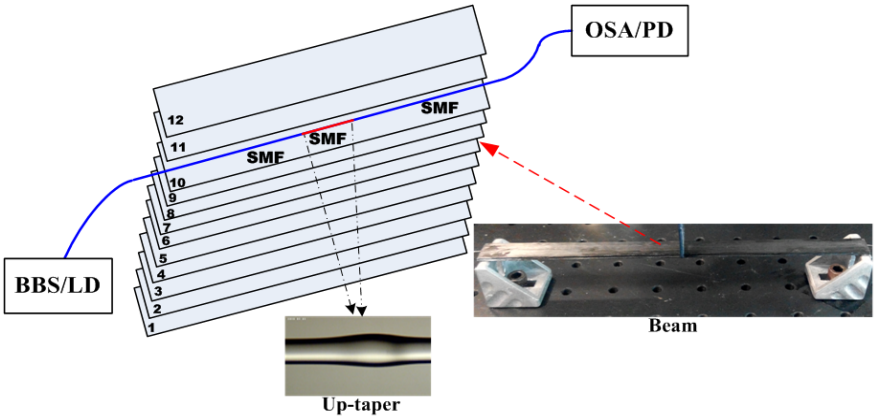


Figure 4.28 Schematic structure and photograph of the sensor and the experimental setup

The schematic structure and photograph of the CCFC based beam embedded with the MMI, and experimental setup are shown in Figure 4.28. An un-polarized C and L BBS was used as the optical source. The transmission spectrum of MMI was measured by an OSA. The inset in Figure 4.28 shows the microscope image of the fiber fusion up-taper, and the two fiber tapers have almost the same maximum waist diameter of about 168 μm. Figure 4.29 shows the transmission spectrum of the MMI and its corresponding spatial frequency spectrum. As can be seen, its ER reaches 27.7 dB, and a deep resonance dip within C and L bands is shown. One dominated cladding mode and one weak cladding mode are excited simultaneously, as shown in Figure 4.29 (b). The interference mainly occurs between the core mode and the dominant cladding mode. Due to the modulation function of the weak cladding mode on the interference pattern, the MMI only has one deep resonance dip.

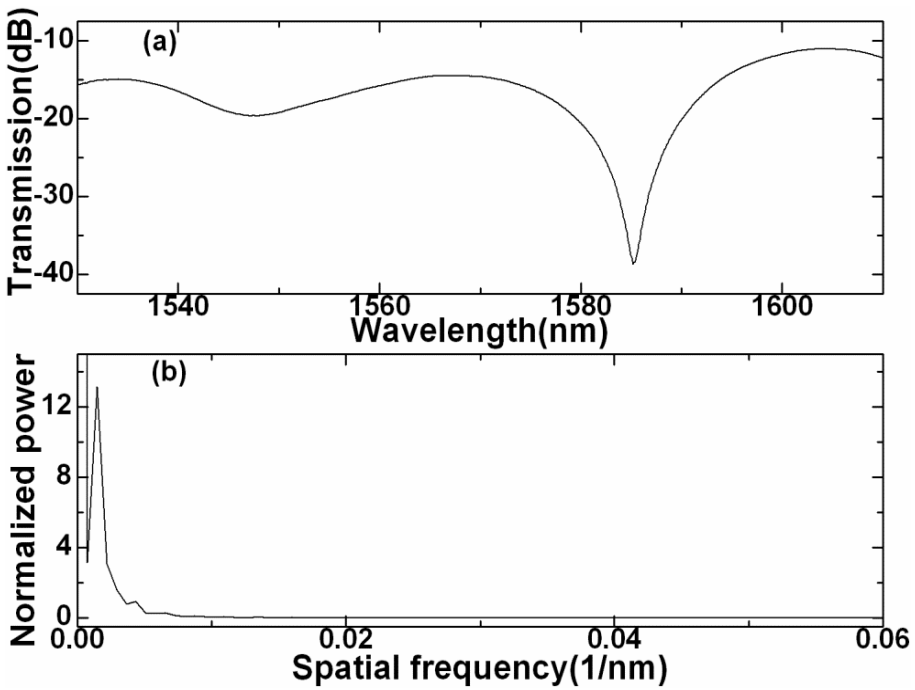


Figure 4.29 (a) Transmission spectrum of the MMI and (b) its spatial frequency spectrum

The CCFC based beam is constructed by 12-layer CCFC laminates. The MMI is embedded in the 9th and 10th layers along the reinforced fiber direction of the CCFC. The thickness of each layer of the composite is 125 μm. The length, width, and thickness of the CCFC based beam are 20 cm, 1.3 cm, and 1.5 mm, respectively. The beam was put on a three bending test platform with the 12th layer touched on the two holders, which were fixed on an optical table. When a displacement *d* is applied to the beam, the cladding mode and core mode experience power losses simultaneously, and the power coupling condition from the cladding mode to the core mode change accordingly. Under a dynamic displacement with an angular frequency of $\omega$, assuming that the

power coupling coefficient is $kd\sin(\omega t)$, where $k$ is a coefficient, describing the power coupling efficiency from the cladding mode to the core mode, the ER of the MMI can be given by

$$ER = 10\lg\left(\frac{1+\sqrt{kd\sin(\omega t)I_2/I_1}}{1-\sqrt{kd\sin(\omega t)I_2/I_1}}\right)^2, \tag{4.12}$$

where $I_1$ and $I_2$ are the power distributed in the core mode and the cladding mode, respectively, with $I_2 < I_1$. The displacement induced bending leads to power loss of the core and cladding modes, respectively, and the cladding mode experiences more and faster power loss than core mode. Thus, with the increase of the displacement, the power ratio $I_2/I_1$ of the two modes decreases accordingly. This leads to a reduction of the ER [33].

Since the length of the MMI is much shorter than that of the beam, we can assume the section of the beam where the MMI located is a circular arc. Hence, its radius of curvature is directly proportional to the displacement of the beam. Based on the theory of material mechanics [75], when a displacement *d* is vertically applied to the central position of the beam within its elastic range, the induced strain $\varepsilon_d$ along the MMI can be expressed as [68],

$$\varepsilon_d = \frac{12y}{l^2}d, \tag{4.13}$$

where *y* is the distance between the strained and neutral layers, and *l* is the

span of the beam. As a displacement is applied to the beam, the MMI suffers an extension strain due to the beam extension, simultaneously it experiences a bending induced strain distribution of $\varepsilon_b$, hence the wavelength shift of $\Delta\lambda_\varepsilon$ due to the beam extension strain and bending induced strain can be given by

$$\frac{\Delta\lambda_\varepsilon}{\lambda} \approx (1+\frac{p_{co}n_{co}-p_{cl}\overline{n}_{cl}}{n_{co}-\overline{n}_{cl}})(\varepsilon_d+\int_0^L \varepsilon_b dz), \tag{4.14}$$

where $L$ is the length of the MMI, $n_{co}$ is the effective RI of the core mode, $\overline{n}_{cl}$ is the averagely effective RI of the cladding mode since the cladding mode is position dependent, and $p_{co}$ and $p_{cl}$ are the elasto-optic coefficients of the core mode and cladding mode, respectively.

### 4.8.3 Experimental Results and Discussions

The OSA with a wavelength resolution of 0.01 nm was used to measure the transmission spectrum. With the increase of the displacement, the ER of the MMI decreases accordingly, simultaneously the transmission spectrum of the MMI experiences a corresponding blue shift, as shown in Figure 4.30. There is a quasi-linear relationship between the displacement and ER variation, and its correlation coefficient square reaches 0.9867, with a displacement sensitivity

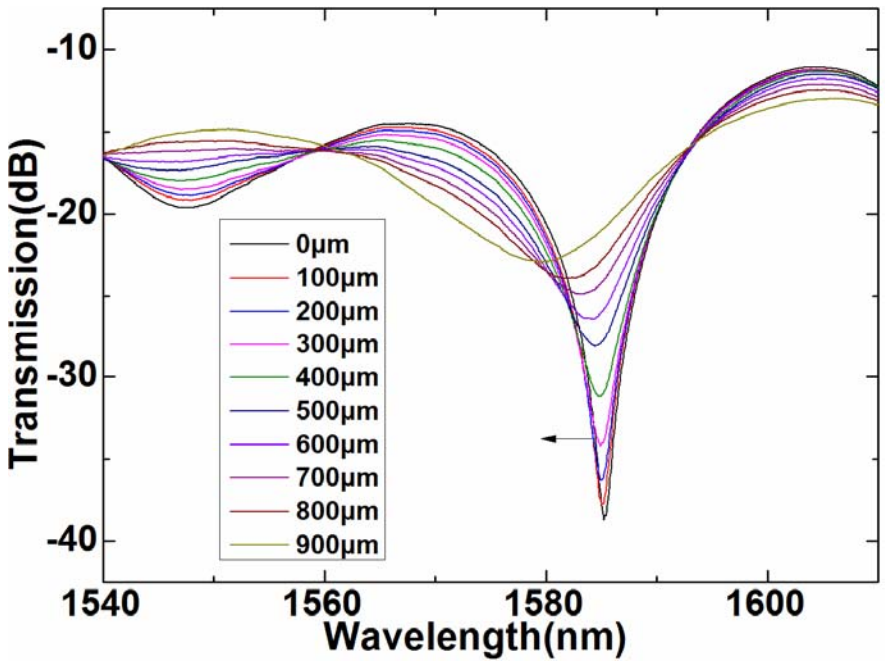


Figure 4.30 Transmission spectral responses to displacement

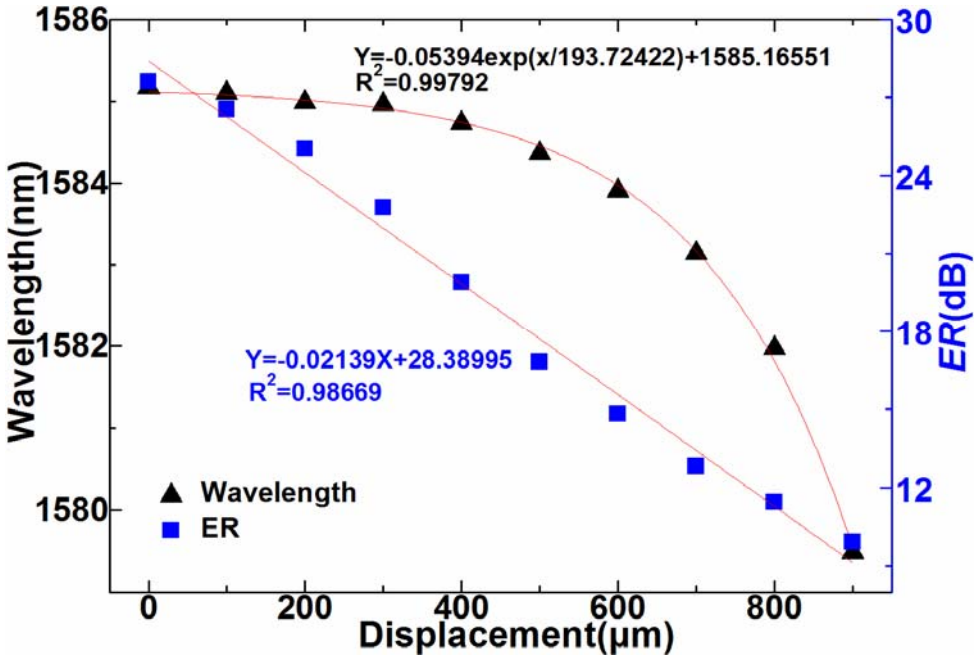


Figure 4.31 Relationships between the displacement and the dip wavelength/ER

of -0.0214 dB/μm, as shown in Figure 4.31. Under a 0.1-dB resolution of the OSA, the displacement resolution reaches 4.67 μm. Hence, it can be used as a low cost intensity-modulated fiber micro-displacement sensor. The dip wavelength decays exponentially with the enlargement of the displacement, as also shown in Figure 4.31. There is a quasi-linear relationship between the displacement and wavelength shift within the displacement range of 0~400 μm, with a displacement sensitivity of -1.01 pm/μm. This matches our theoretical predication in Eq.4.14, the dip wavelength of MMI has a quasi-linear relationship with the beam extension strain $\varepsilon_d$ if we do not consider the bending induced strain $\varepsilon_b$ . When the displacement is larger than 400 μm, the bending induced strain $\varepsilon_b$ becomes distinct, hence the dip wavelength decays greatly with the increase of the displacement, here about 5.244-nm wavelength shift occurs when the displacement changes from 400 μm to 900 μm.

To test the dynamic response of the sensor, an electro-dynamic type vibration exciter was used to apply the dynamic displacement to the sensor. A laser diode (LD), with 9.67-dBm power output and 1585.65-nm wavelength just located within its quasi-linear wavelength range, was used as the optical source, and a photo-detector (PD), with the bandwidth of 125 MHz, was used to capture the optical power. The sensing signal detected by the PD was monitored by an oscilloscope (OSC). Experimental results show that the

dynamic measurement range is within the range of 0~200 Hz. Figures 4.32 (a) and (b) show the measured output voltage versus time graphs of the sensor under 1.2 and 200-Hz dynamic displacements, respectively. It should be noted that the above measurements have good repeatability, which are attributed to the substantial sensor structure and the good restorability of the carbon-fiber composite material.

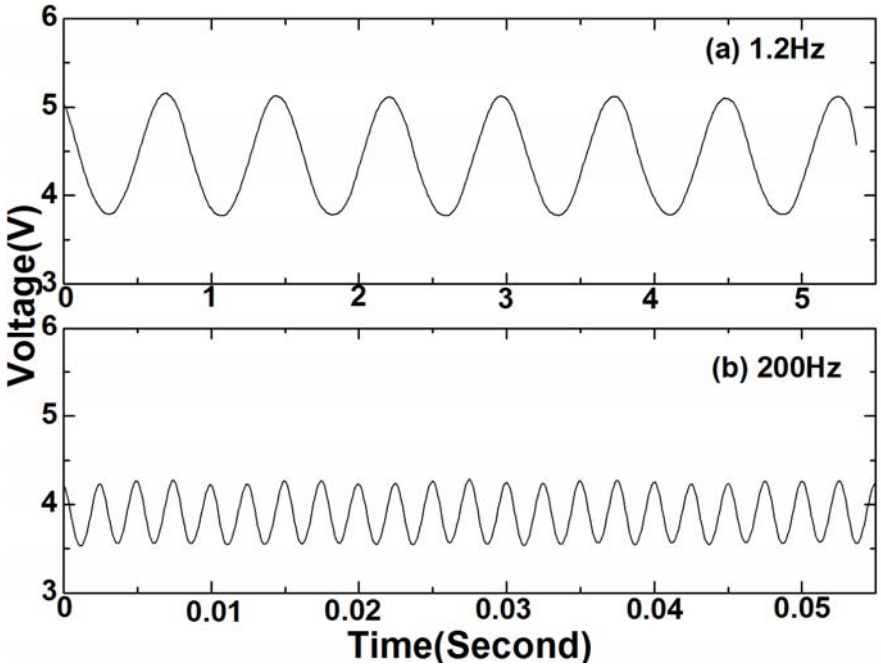


Figure 4.32 Response of the sensor under dynamic displacement

For the fiber micro-displacement sensor, its temperature cross-sensitivity is a critical problem that should be considered. To get its thermal characteristics, we put it in a temperature controller under a 100-μm pre-displacement, with a digital thermal-meter as the calibrator. With the increase of the temperature, its transmission spectrum experiences a

corresponding red shift, as shown in Figure 4.33. There is a quasi-linear relationship between the temperature and its ER variation, with the correlation coefficient square and sensitivity of 0.9934 and 0.054 dB/°C, respectively, as shown in Figure 4.34. Compared to its displacement response trend, the thermal response shows an opposite trend. This shows that the thermally induced ER-increase can be compensated by the displacement induced ER-reduction. Hence, a pre-displacement on the sensor can be used to compensate the temperature influence. According to its sensitivities to displacement and temperature, a 2.5-μm pre-displacement can compensate 1-C° temperature variation.

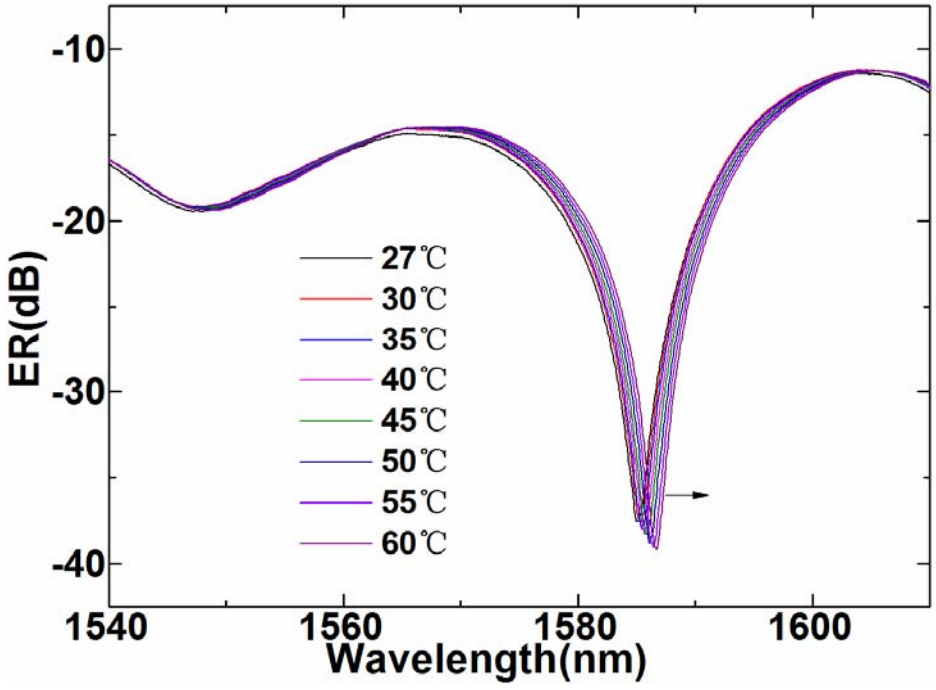


Figure 4.33 Transmission spectrum responses to temperature

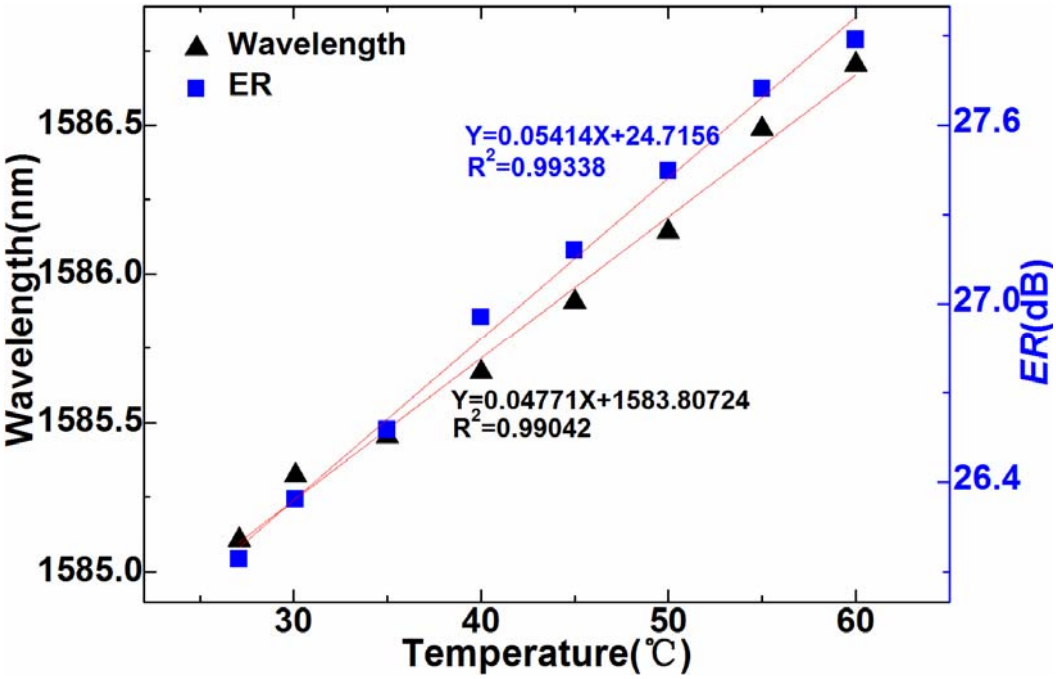


Figure 4.34 Relationship between the temperature and its ER/dip wavelength

As can be seen from Figure 4.34, the dip wavelength also changes quasi-linearly with the temperature, with the correlation coefficient square and sensitivity of 0.9904 and 0.048 nm/°C, respectively. Fortunately, there are also opposite response trends for the temperature and displacement induced wavelength shifts. Hence, the temperature induced red shift can be compensated by the displacement induced blue shift.

### 4.8.4 Conclusions

In conclusion, an intensity-modulated micro-displacement sensor based on an embedded DCMs MMI has been demonstrated. The DCMs excited in such MMI enable it have a much high ER, guaranteeing it to be used as a low-cost intensity-modulated micro-displacement sensor with a high measurement

resolution. Its temperature-cross sensitivity can be compensated by applying a corresponding pre-displacement. The fabrication of the MMI only involves cleaving and automatic splicing with the standard communication SMF, allowing its good reproducibility, low cost, and good integration ability with other fiber components. The miniaturized and compact size, linearity and high measurement resolution would enable this type of sensor to be widely used in displacement measurement industry.

## 4.9 Ultrahigh-Sensitivity FAS with the MMI

### 4.9.1 Introduction

Acoustic sensors have been widely applied in various areas, especially in navigation, health imaging, and the non-destructive evaluation (NDE) of structures and facilities. Common acoustic sensors are piezoelectric transducers (PZTs), which directly convert acoustic signal into output voltage. However, as we all know, they cannot be used in the environments of electromagnetic interference, chemical corrosion, high temperature, etc. Hence, FASes have attracted much attention. Not only they do have high adaptability in the above-mentioned environments, but also they can be deployed in remote areas for real-time monitoring. The first FAS was proposed by Bucaro et al. and Cole et al. in 1977 [76-78]. Several types of FASes, based on interferometric configurations, such as Mach-Zehnder (MZ) [79], Michelson [80], Sagnac [81,82], Fabry-Pérot (FP) [83-85], fiber Bragg

grating (FBG) [86], and distributed Bragg reflector (DBR) [87,88], have been proposed. The MZ FAS uses one of its arms to sense the acoustic wave and the other one is used as the reference. Additionally, thin-tapers being used on the sensing arm of the MZ one can significantly improve its sensitivity [79]. However, the two-arm MZ FAS is bulky, and it is very fragile due to the thin tapers. The Michelson FAS has the same issue as that of the MZ FAS. The Sagnac FAS has to employ a longer fiber [81,82], which leads to its bulkiness. Due to the high value (about 72 GPa) of the Young's modulus of the optical fiber, the FBG acoustic sensor has a lower sensitivity to the acoustic wave, and has to be coated by a material with a lower Young's modulus to improve its sensitivity [86]. The FP FAS is modelled on a diaphragm based reflection surface with its stability limited by the diaphragm performance and the glue fixing material [83-85]. Recently, a new compact DBR acoustic sensor based on two FBG reflection mirrors was proposed [88]. However, its fabrication method is complicated and expensive. Moreover, it cannot detect the low frequency acoustic wave, such as kHz, due to its limited line-width.

Most of the FASes mentioned above have to be immersed in a water tank to take acoustic measurements. It is well known that acoustic signals are relatively strong in water, but are greatly attenuated and become very weak outside of the water tank. To meet NDE measurement requirements, the acoustic sensors need to be attached on the outside surface of the structures and facilities. In previous years, there have been few reports on surface

mounted FASes.

In this study, a miniaturized and compact DCMs fiber up-taper interferometer based on surface-mounted FAS with an ultrahigh sensitivity is demonstrated. The interferometer has an interference pattern with an ER of more than 20 dB, enabling it to be used as an intensity-modulated FAS with an ultrahigh sensitivity. Moreover, it has simultaneous responses to the acoustic pressure in wavelength shift and power coupling change from the cladding mode to the core mode. This is the other reason why it has an ultrahigh sensitivity. Its temperature-dependent wavelength shifting issue can be solved by applying a corresponding pre-strain since it has opposite wavelength shift trends in response to strain and temperature

## 4.9.2 Principle of Operation

Figures 4.35 (a) and (b) show the typical transmission spectrum of the 2-cm FAS and its corresponding spatial frequency spectrum, respectively. The maximum ER of the interference fringes reaches more than 20 dB, and its transmission spectrum has only one deep resonance dip within C and L bands. As can be seen from Figure 35 (b), just two cladding modes are excited, one dominant cladding mode and the other weak cladding mode. The phase $\varphi$, due to the interference between the core mode and the dominant cladding mode, can be given by $\varphi=2\pi(n_{co}-\overline{n}_{cl})L/\lambda$, where $L$ is the length of the

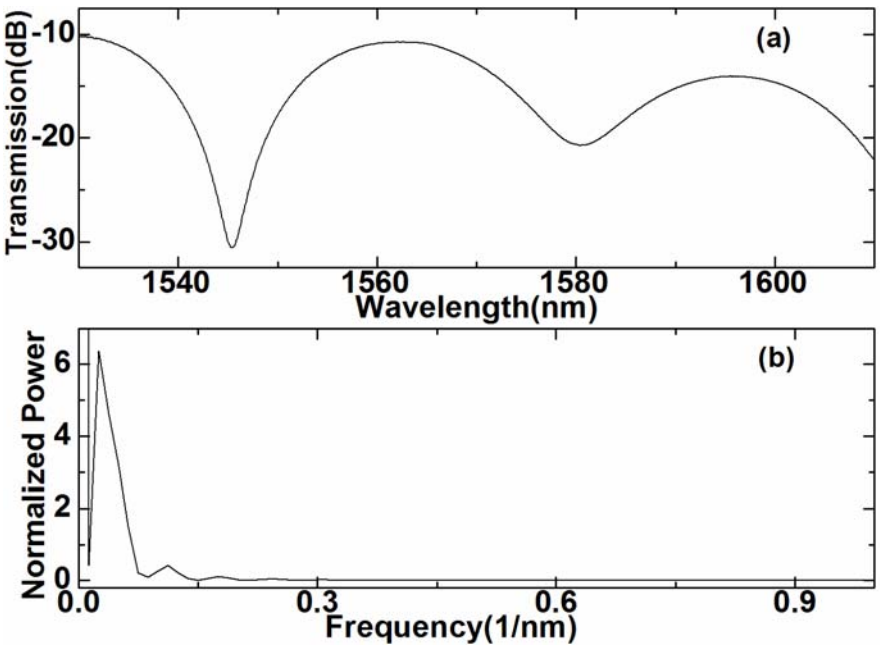


Figure 4.35 (a) Transmission spectrum of the FAS and (b) its spatial frequency spectrum

FAS, $n_{co}$ is the effective refractive index (RI) of the core mode, $\overline{n}_{cl}$ is the averagely effective RI of the cladding mode and it satisfies $\int_0^L n_{cl}(z)dz = \overline{n}_{cl}L$, and $n_{cl}(z)$ is the effective RI of the cladding mode and is position dependent. The resonance dip of $\lambda_k = \frac{2(n_{co} - \overline{n}_{cl})L}{2k+1}$ occurs when the phase satisfies $\varphi = (2k+1)\pi$, where $k$ is an integer, representing the interference order.

When an acoustic pressure is applied to the FAS, it experiences a corresponding dynamic micro-bending modulation, which causes its dynamic wavelength shift and dynamic power coupling change from the cladding mode

to the core mode simultaneously. The acoustic pressure induced micro-bending leads to a corresponding strain distribution $\varepsilon(z) = K_{\varepsilon}(z) P_a \sin(\omega_a t)$ along the FAS, where $K_{\varepsilon}(z)$ is a position dependent coefficient, describing the transforming efficiency from the acoustic pressure to the micro-bending along the FAS, and $p_a$ and $\omega_a$ are the amplitude and angular frequency of the acoustic pressure, respectively. Hence, the dynamic wavelength shift due to the acoustic pressure can be given by

$$\Delta\lambda_k = P_a \sin(\omega_a t)\lambda_k (1 + \frac{p_{co} n_{co} - p_{cl} \overline{n}_{cl}}{n_{co} - \overline{n}_{cl}}) \int_0^L K_{\varepsilon}(z) dz , \qquad (4.15)$$

where $p_{co}$ and $p_{cl}$ are the elasto-optic coefficients of the core mode and cladding mode, respectively.

As stated earlier, simultaneously there is also a power coupling change from the cladding mode to the core mode due to the acoustic pressure. Assuming that the power coupling coefficient is $K_a P_a \sin(\omega_a t)$, where $K_a$ is a coefficient, describing the power coupling efficiency from the cladding mode to the core mode, the acoustic pressure induced ER variation can be given by

$$ER = 10 \lg(\frac{1 + \sqrt{K_a P_a \sin(\omega_a t) I_2 / I_1}}{1 - \sqrt{K_a P_a \sin(\omega_a t) I_2 / I_1}})^2 , \qquad (4.16)$$

where $I_1$ and $I_2$ are the power distributed in the core mode and cladding mode, respectively, with $I_2 < I_1$.

According to Eqs.4.15 and 4.16, when using a single wavelength laser with the wavelength just located within the quasi-linear wavelength range of the FAS, the intensity of the laser can be simultaneously modulated by the wavelength shift and the ER variation induced by the acoustic pressure.

### 4.9.3 Experimental Results and Discussions

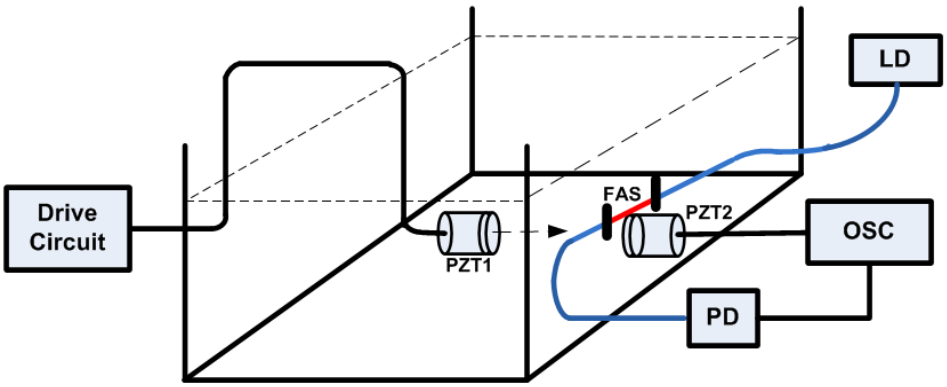


Figure 4.36 Schematic configuration of the experimental setup

The schematic configuration of the experimental setup is shown in Figure 4.36. A 120-KHz ultrasound generator, PZT1, was placed in the water and used to generate the ultrasound, and its intensity was controlled by tuning its drive voltage. The FAS was surface-mounted to the outside of the water tank and stretched tightly with tapes. A piezoelectric acoustic sensor, PZT2, was also surface mounted onto the outside of the water tank close to the FAS, and was used to calibrate the FAS. A laser diode (LD), with a wavelength of 1546.64 nm and output power of 5.41 dBm, was used as the optical source. The wavelength of the LD locates just within the quasi-linear wavelength range of the interference fringe of the FAS. A PD with a 125-MHz bandwidth was used

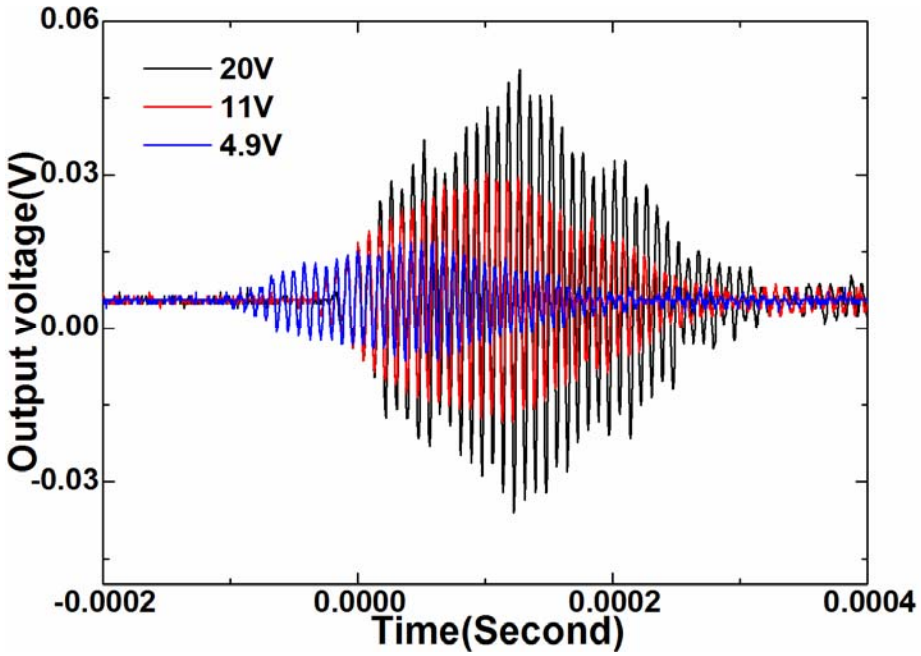


Figure 4.37 Output voltage vs. time graphs of the FAS

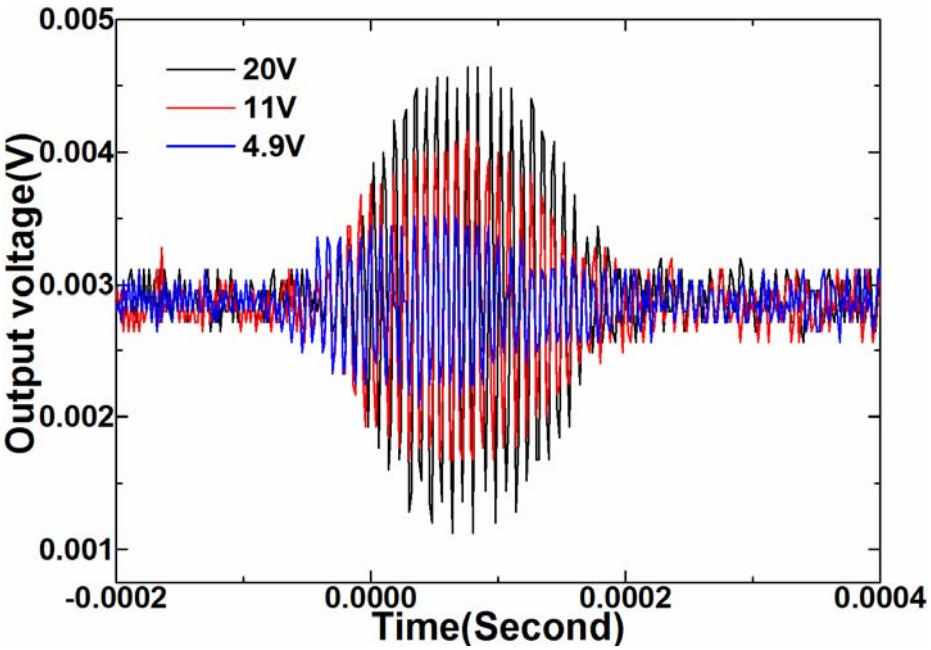


Figure 4.38 Output voltage vs. time graphs of PZT2

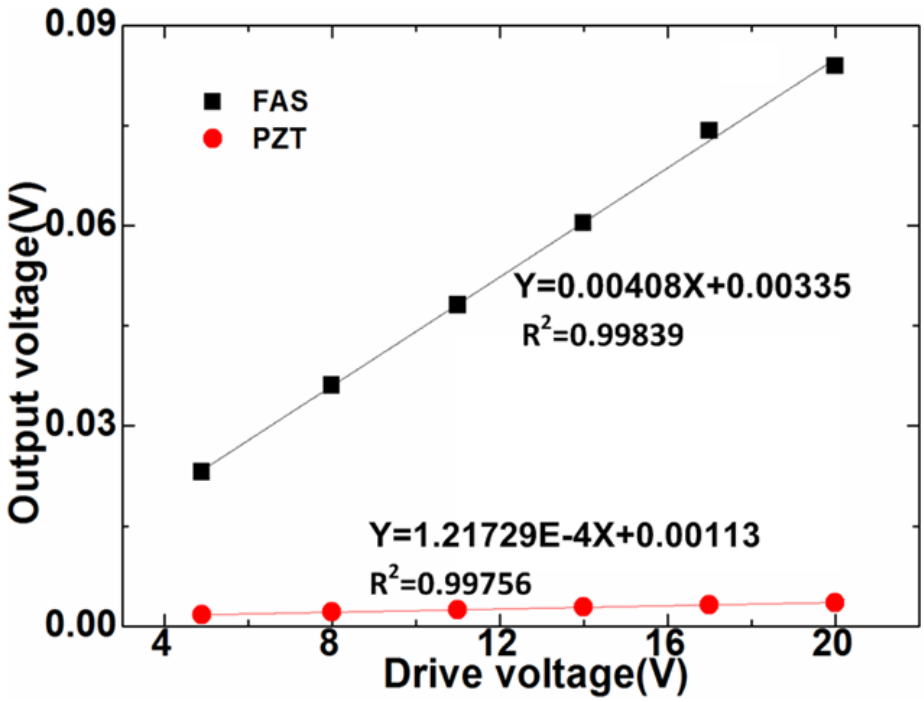


Figure 4.39 Relationships between the maximum PP voltage and the diver voltage of the FAS and PZT2

to detect the optical sensing signal. An OSC was used to capture the electric sensing signals. Figures 4.37 and 4.38 show the measured output voltage vs. time graphs of the FAS and PZT2 under the driver voltages of 4.9, 11 and 20 V, and distance of 27.5 cm away from the generator. As the drive voltage is increased, the maximum peak to peak (PP) output voltages of the FAS and PZT2 increase quasi-linearly accordingly, with the FAS having a distinct larger sensitivity, as shown in Figure 4.39, the slope of the FAS is distinctly larger than that of the PZT2. Using the PZT2 as the calibrator, we can get the measured relationship between the PP output voltage and acoustic pressure for the FAS, as shown in Figure 4.39. The sensitivity of the FAS reaches about 2.65 V/ μPa and is 33.5 times larger than that of the PZT2. It should be noted

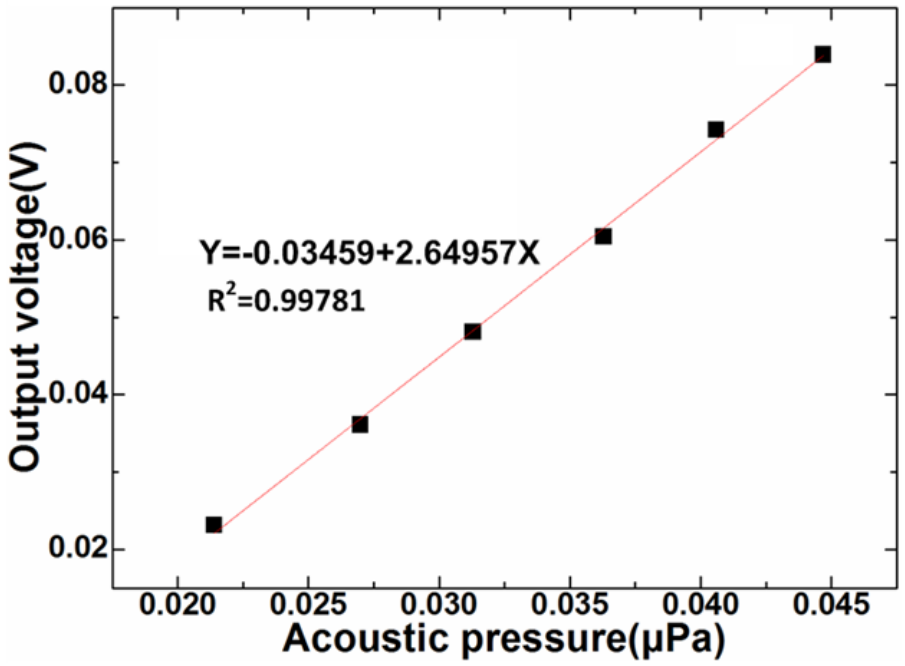


Figure 4.40 Relationship between the output voltage and the acoustic pressure of the FAS

that the output voltage is influenced by the reflection and diffraction of the ultrasound source in the water tank. Hence, the measurement accuracy can be improved further by adopting the water tank with ultrasound absorption materials. Experimental results show that the minimum response frequency of the FAS is 1 Hz. Due to the limitation of the operation frequency of the acoustic generator and PZT2 calibrator, we just demonstrate the performance of the FAS at 120-KHz acoustic pressure.

To explain in detail the sensitivity of the proposed FAS, we also demonstrated its macro-bending sensing performance. It was held by two fiber holders (62-cm apart) placed on an optical table; its left side was mounted directly to the optical table and the right side was mounted on a translation

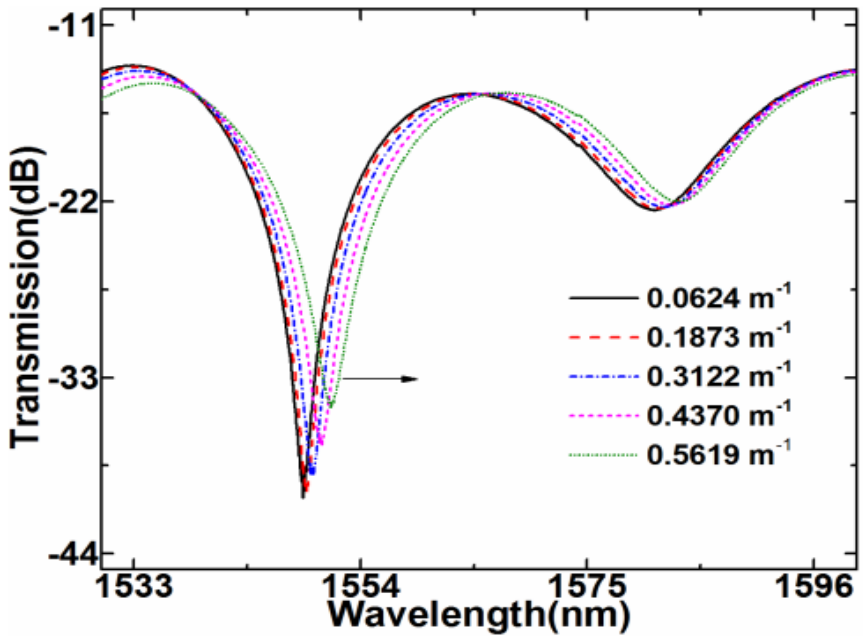


Figure 4.41 Transmission spectral responses to curvature

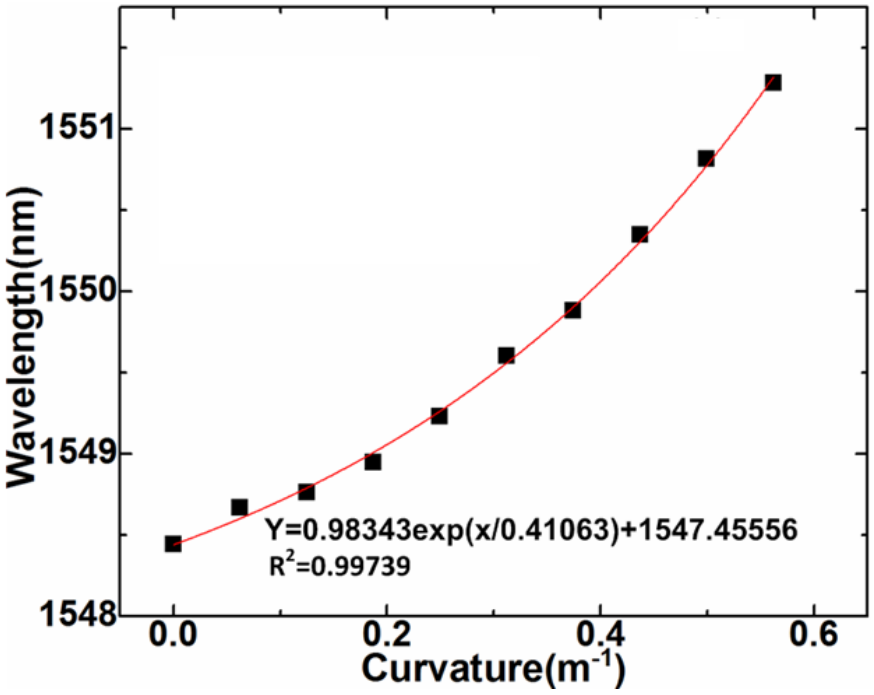


Figure 4.42 Relationship between the curvature and the left dip wavelength

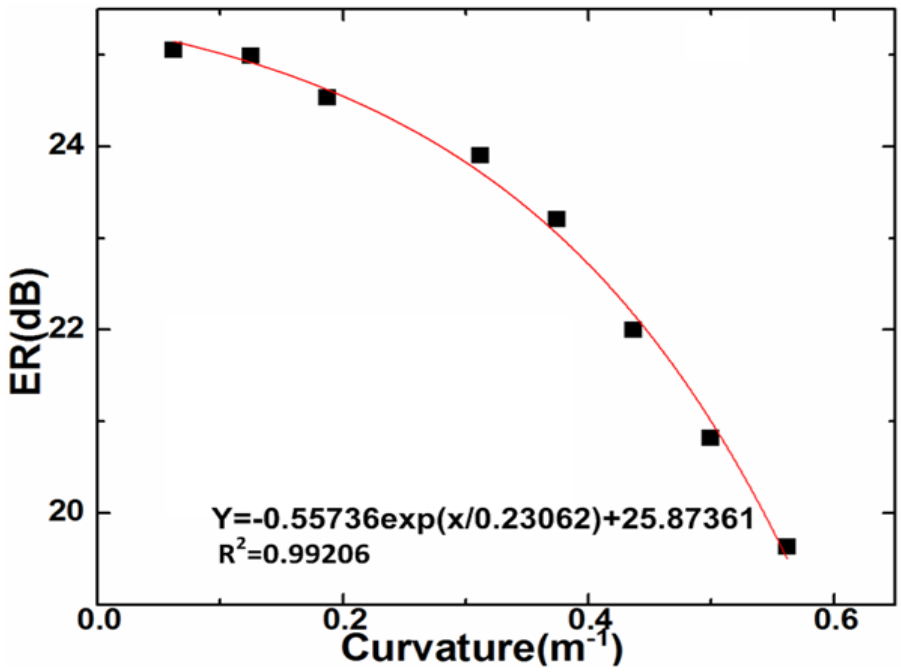


Figure 4.43 Relationship between the curvature and its ER

stage. Its curvature was changed by shrinking the length of the fiber, which was fixed between the two holders. With the increase of the curvature, the transmission spectrum experiences a corresponding red shift, as shown in Figure 4.41. Its dip wavelength increases exponentially with an increase in curvature while its maximum ER decreases exponentially, as shown in Figures 4.42 and 4.43, respectively. From a curvature of 0.0624 to 0.5619 $m^{-1}$, about 2.613-nm wavelength shift and 5.416-dB ER reduction occur simultaneously. The two responses, in wavelength shift and ER variation, simultaneously contribute to the ultra-high sensitivity of the FAS. Unlike the responses from macro-bending, the micro-bending induced responses in wavelength shift and power coupling only have limited variation ranges. Hence, we can regard their relationships with the acoustic pressure as quasi-linear.

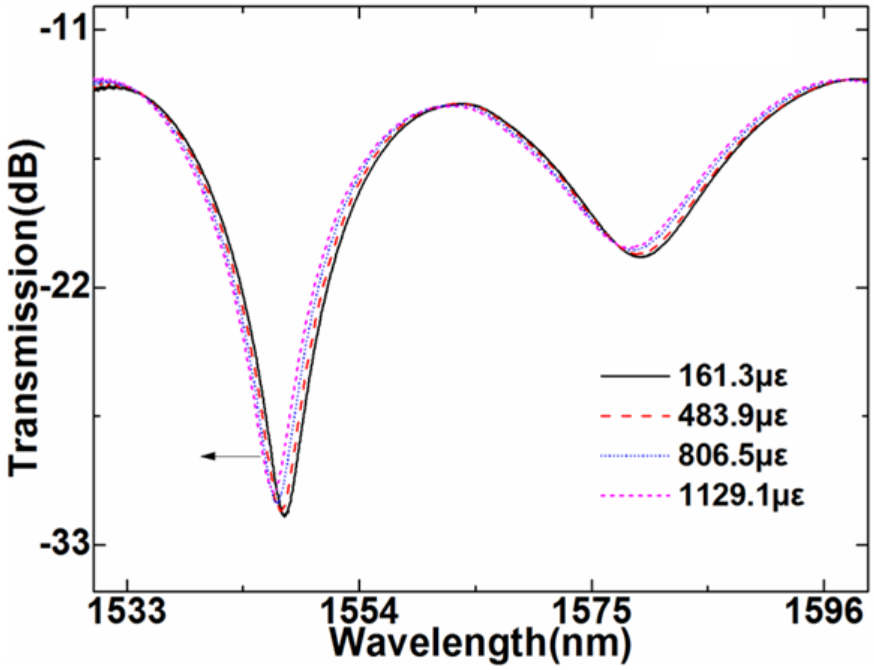


Figure 4.44 Transmission spectral responses to strain

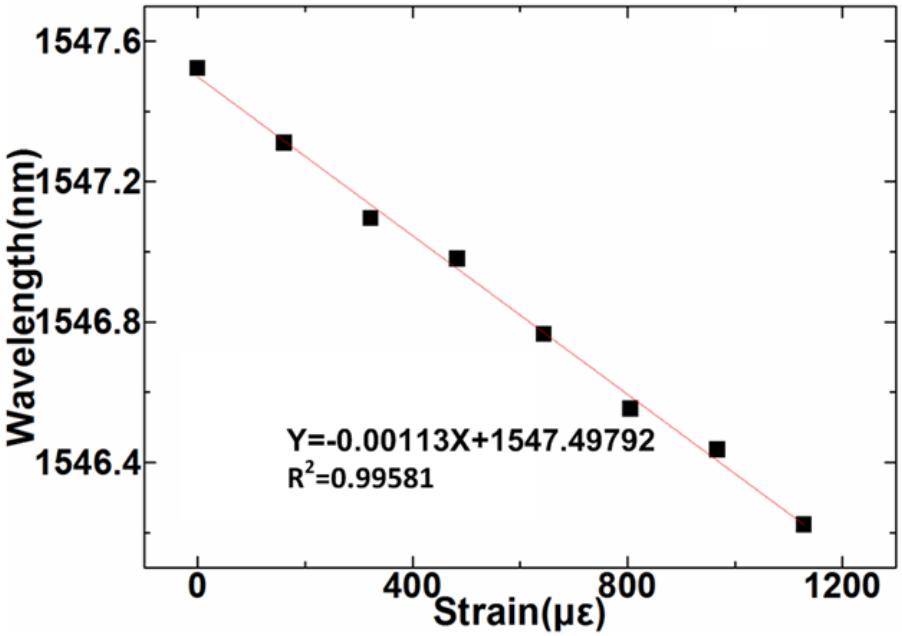


Figure 4.45 Relationship between the strain and the left dip wavelength

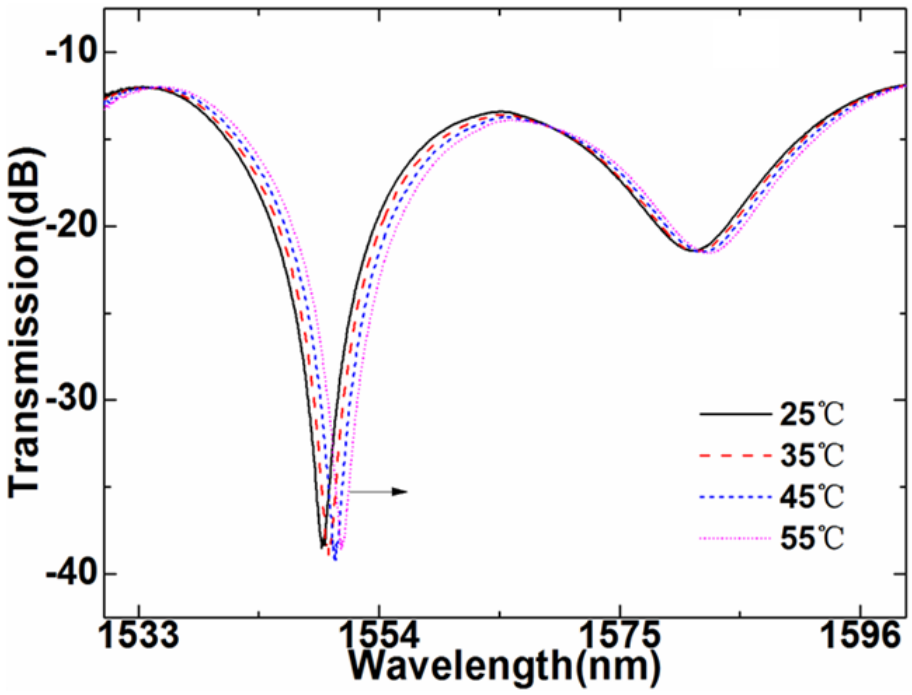


Figure 4.46 Transmission spectral responses to temperature

Using the curvature measurement platform, we also demonstrated its strain sensing response. The strain could be applied by stretching the length of the fiber fixed between the two holders. With the increase in strain, the transmission spectrum experiences a corresponding blue shift, as shown in Figure 4.44. Its dip wavelength decreases quasi-linearly accordingly, with a strain sensitivity of -1.13 pm/με, as shown in Figure 4.45.

For an FAS sensor, its temperature cross-sensitivity needs to be considered. To avoid the bending effect, the FAS was fixed on a U-groove slab in a temperature controller. A digital thermal-meter was used to calibrate its ambient temperature. As the temperature increases, the transmission spectrum experiences a corresponding red shift, as shown in Figure 4.46. There is a

quasi-linear relationship between the temperature and the dip wavelength, and its thermal sensitivity reaches 59 pm/C°, as shown in Figure 4.47. Compared to its strain response trend, the thermal response shows an opposite trend. This shows that its temperature induced red shift can be compensated with the strain induced blue shift. Hence, a pre-strain on the sensor can be used to compensate the temperature influence. According to its sensitivities to strain and temperature, a 52.2-με pre-strain can compensate 1-C° temperature variation.

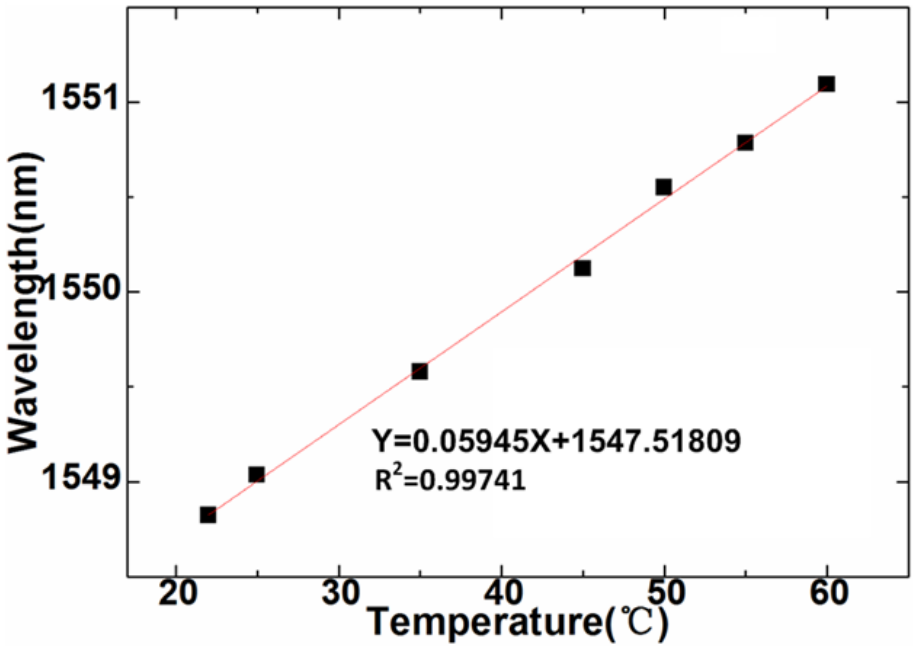


Figure 4.47 Relationship between the temperature and the left dip wavelength

## 4.9.4 Conclusions

In conclusion, a DCMs fiber up-taper interferometer based surface-mounted acoustic sensor with an ultrahigh sensitivity has been demonstrated

theoretically and experimentally. The optimized dual fusion up-tapers along the SMF enable the dual excited cladding modes, guaranteeing its high ER interference pattern for intensity-modulated and ultrahigh-sensitivity FAS application. Besides this, its simultaneous responses to the acoustic pressure in wavelength shift and power coupling from the cladding mode to core mode also contribute to its ultrahigh sensitivity. Its sensitivity reaches 2.65 V/ μPa and is 33.5 times larger than that of the surface-mounted PZT. Its temperature cross-sensitivity could be compensated by applying a corresponding pre-strain. The fabrication of the sensor involves cleaving and splicing with a low cost standard SMF, allowing easy integration with the other fiber components. The intensity-referenced interrogation method for the sensor guarantees its low cost. This type of sensor shows the distinct advantages of simple and compact structure, small size, and ultrahigh sensitivity. It has potential to be widely used in acoustic measurement industry.

## 4.10 Conclusions

In this chapter, a novel DCMs fiber up-taper MMI has been proposed and demonstrated. With the enlarged “overlap” parameter of a commercial splicer, high ER SMF based DCMs MMIs could be fabricated automatically by constructing two adjacent fiber up-tapers on one same SMF. This type of MMI is almost like the LPG device, also with a deep resonance dip within C and L bands. It could be used for temperature, strain, RI, micro-displacement,

ultrasound and dual parameter measurements. The MMIs with different lengths have almost the same temperature and strain sensitivities for the deep resonance dip. When it is used as a strain sensor, its temperature-cross issue can be solved by applying a pre-strain since it has opposite wavelength shift trends in response to strain and temperature. With an MDM method, the DCMs in the MMI can be discriminated for simultaneous measurement of strain and temperature with high measurement resolutions. By embedding the MMI in a CCFC based beam, it can be used as an intensity-modulated micro-displacement sensor with a high sensitivity, and its temperature-cross issue can be solved by applying a pre-displacement since its ER response trends to strain and temperature are opposite. Due to its high ER and simultaneous responses to the acoustic pressure in wavelength shift and intermodal power coupling change, it can be used as an intensity-modulated FAS with an ultrahigh sensitivity, and its temperature-cross issue can be solved by applying a pre-strain. In addition, the fabrication of the MMI only involves cleaving and splicing with a low cost standard SMF, allowing its easy integration with the other fiber components. Compared to the fiber down-taper MMI, this type of MMI is more robust. Moreover, as fiber sensors, the miniaturized and compact size, linearity and high sensitivity would enable this type of sensor to be used in practical measurement industry.

# Chapter 5

# Ethanol-Filled PBF based MMIs

In this chapter, the light guidance characteristics of the fully and partially ethanol-filled PBFs are investigated firstly, then the thermal performances of the ethanol-filled PBF based MMIs are demonstrated theoretically and experimentally.

## 5.1 Introduction

The first application of the photonic bandgap fiber (PBF), also called bandgap guiding hollow core PCF, is for gas sensing in 2005 since there is a large overlap of the optical field with the measured gas [89]. Then much interest has been focused on the PBF based interferometers due to their advantages of temperature insensitiveness, simple structure and easy fabrication, especially for their wide applications in fiber sensing [90-96]. By splicing a very short section of PBF between the SMFs [5,90] or use discharging fabrication

method [91,92], simple FPIs can be constructed. The other main application of the PBF is for MMIs. Different from the PBF based FPIs, to construct the PBF MMIs, some special splicing techniques, such as tapering splicing [93], fully collapsed splicing [94] and mismatch offset splicing [36], have to be used to splice the PBF to the SMFs since they can effectively excite high order cladding modes in the PBFs to construct the core-cladding MMIs. The above-mentioned interferometers have been widely used for strain, temperature, curvature and RI sensing. However, it should be noted that when the PCFs are used as temperature sensors, their thermal sensitivities are relatively lower, especially for the PBFs due to their air core and air cladding structures. A PBF based MMI was proposed for temperature sensing with a thermal sensitivity of ~−7.1 pm/°C [93] while a core-offset PBF based MI was with the thermal sensitivity of ~6.66 pm/ °C [36].

It should be noted that different from the solid core index guiding PCFs [34, 95-97] that guide light by total internal reflection (TIL), the light in the PBF is confined and guided via a photonic bandgap that prohibits the propagation of light in the cladding region under certain conditions. If changing the RI of the core or cladding region of the PBF, the light confinement and guidance conditions are changed accordingly. Although their confinement loss becomes bigger, there still exist some low-loss windows for applications [98]. Totally different from the solid core index guiding PCFs, as we all know, the core index value of the solid core PCF is fixed and cannot be

changed. Hence, even filling the ethanol in the air claddings of a solid core index guiding PCF [95], the effective refractive index difference between the interference modes is only $3.838 \times 10^{-3}$. Although an index guiding Ethanol-filled polarization maintaining PCF (PMPCF) could be used as a high sensitivity thermal sensor [97], a 3-dB coupler has to be applied to construct it as a fiber loop mirror, which leads to its complexity and big volume. Moreover, the long length of the PMPCF tends to be influenced by ambient disturbance.

In this study, the light guidance characteristics of the fully and partially ethanol-filled PBFs are investigated theoretically, and the thermal performances of the ethanol-filled PBF based MMIs are demonstrated theoretically and experimentally. For the proposed fully and partially ethanol-filled PBFs, the effective RI difference between the core mode and higher order cladding mode can be improved to $1.02 \times 10^{-1}$ and $9.5 \times 10^{-2}$, are 26.6 and 24.8 times bigger than that in Ref. [95], respectively. For ref. [95], the effective RI difference between two interference modes is only $3.838 \times 10^{-3}$ due to the unchangeable RI of the solid core of the index guiding PCF. Hence, our sensor can be fabricated 26.6 and 24.8 times shorter than that of the index guiding PCF interferometer in Ref. [95] under a same free spectral range (FSR). Different from the ethanol-filled solid core PCFs with only about two support modes [95], even for the unfilled PBF, it can support LP01 and LP04-like modes while for the fully- and partially ethanol-filled PBFs, they can support more high order cladding modes. Without using the

above-mentioned special splice techniques, just splicing a short section of the fully or partially ethanol-filled PBF between the SMFs, a PBF based MMI can be constructed with a high thermal sensitivity. The most important advantage is that the thermal sensitivity of our proposed sensor can be adjusted within a large range by selectively filling the air core and/or air claddings of the PBF with ethanol since its core RI can be changed by filling the ethanol. However, for Ref. [95], its thermal sensitivity cannot be changed further due to the solid core with a fixed core RI. Experimental results show that the thermal sensitivity of the PBF based MMI can be adjusted by selectively filling the air core and/or air claddings of the PBF with ethanol. The fully and partially ethanol-filled PBF based MMIs are with the thermal sensitivities of -292 pm/°C and -120 pm/°C, respectively, and they are 43.8 and 18 times bigger than that of the unfilled PBF based MMI in Ref. [36].

## 5.2 Fabrication of the PBF based MMI

The PBF was fabricated by NKT Photonics, with the core diameter, pitch, cladding diameter, and MFD at 1550nm of 10 μm ± 1 μm, 3.8 μm, 120 μm, and 7.5 μm, respectively. The scanning electron microscope (SEM) image of its cross section is shown in Figure 5.1 (a). It was cut into segments of 8 cm in length, and the plastic coatings of its two ends were stripped using a blade by

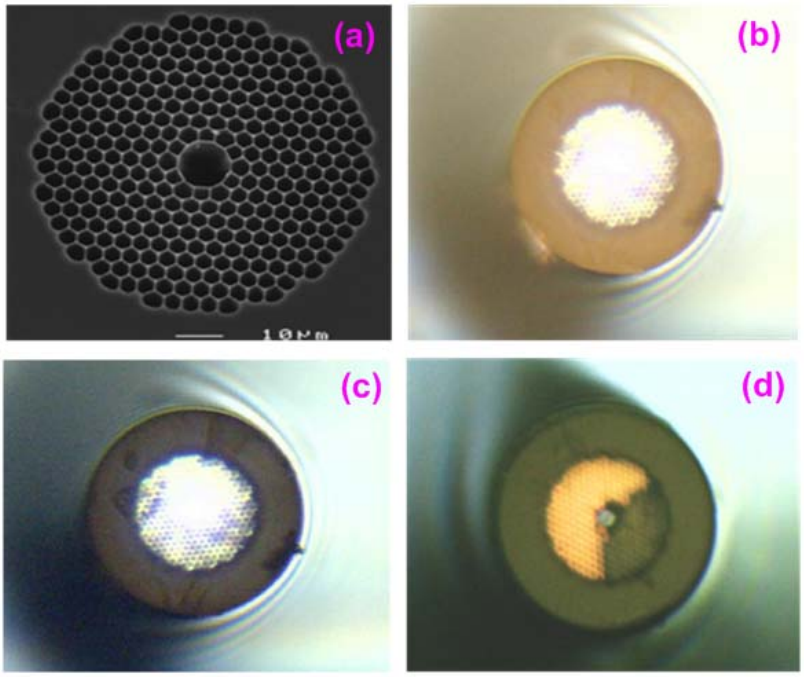


Figure 5.1 (a) SEM of the cross section of the PBF (b) cross section view of the unfilled PBF (c) cross section view of the fully ethanol-filled PBF and (d) cross section view of the partially ethanol-filled PBF

hand for 1.5 cm. Then, its ends were cleaved carefully using a high precision fiber cleaver. A 95% ethanol solution was used for the filling. To fully fill the ethanol in its air core and air claddings, one end of the PBF sample was dipped into the ethanol solution for 20 minutes to allow the solution to fully fill the air holes via capillary force. To partially fill the ethanol into its air claddings, we used resin glue to block the air core and part of the air cladding holes while leaving other cladding holes open, then the other part of the cladding holes were filled by the solution via capillary force. In the experiment, about one-third of the air cladding holes were filled with the solution while the rest were empty. Figures 5.1 (b) and (c) show the cross section views of the

unfilled and fully ethanol-filled PBF after launching a white light into the PBF. As can be seen, a darker and colorful cross section is shown for the fully ethanol-filled PBF, which is caused by the ethanol solution inside. Figure 5.1 (d) shows the cross section view of the partially ethanol-filled PBF.

## 5.3 Mode Analyses

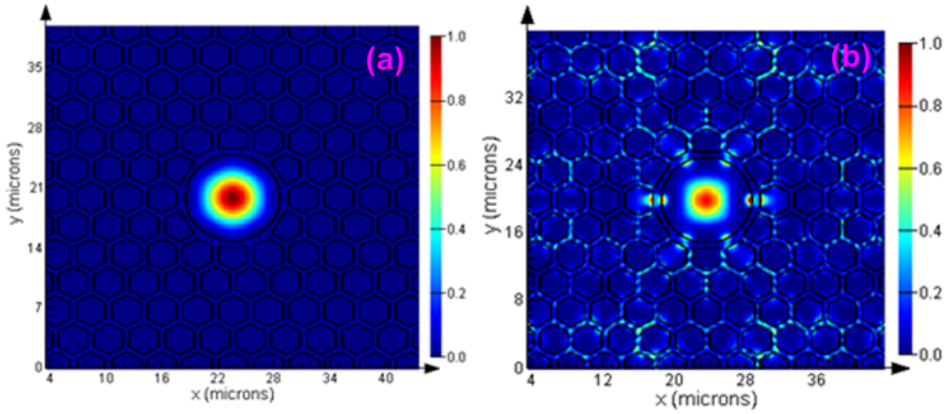


Figure 5.2 (a) LP01 and (b) LP04-like modes of the unfilled PBF

For a better understanding on the ethanol-filled PBF based modal interference, a Finite-difference-time-domain (FDTD) method was used to analyze the propagating modes in the PBF. In our simulation, the diameters of the air core and the pitch between air-holes in the cladding area were taken as 10.1 μm and 3.8 μm, respectively. The RIs of the pure silica and ethanol were initialized to be 1.44570 and 1.3614, respectively. For the unfilled PBF, the core LP01 mode and a high order LP04-like mode co-exist in the PBF, of which the effective RIs are 0.9934227 and 0.9903007 at a wavelength of 1550 nm, respectively, as shown in Figures 5.2 (a) and (b). The effective RI difference

between the two modes is about $3.1\times10^{-3}$.

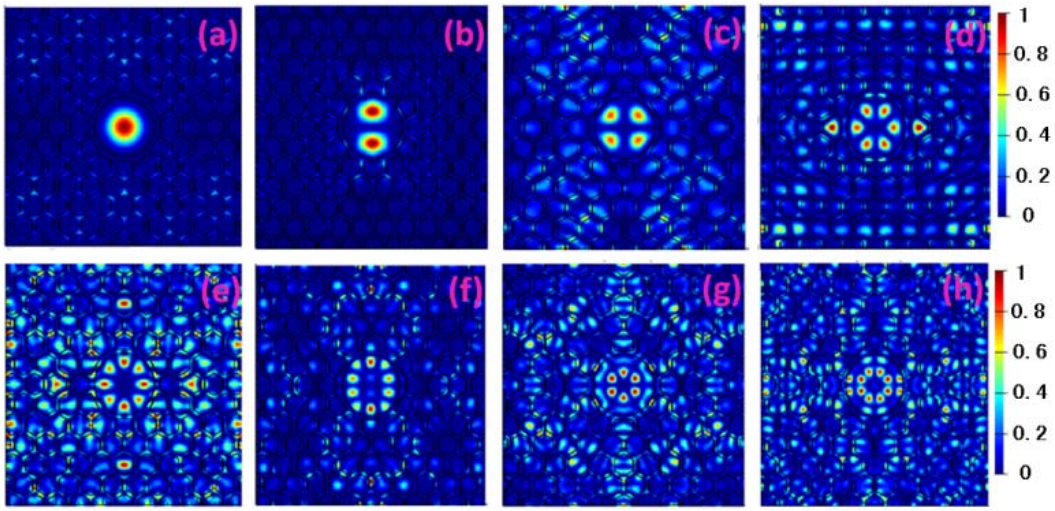


Figure 5.3 Simulated mode patterns of the fully ethanol-filled PBF under effective RIs of (a)1.35515,(b)1.349220,(c)1.338253,(d)1.321603, (e)1.309952,(f)1.297659,(g) 1.277047, and (h)1.252734, respectively

Figure 5.3 shows the simulated mode patterns of the fully ethanol-filled PBF. It can support the core LP01 mode and high order LP11,LP21,LP31,LP41,LP51, LP32 and LP42-like modes at 1550 nm, with the effective RIs of (a)1.35515, (b)1.349220, (c)1.338253, (d)1.321603, (e)1.309952, (f)1.297659, (g)1.277047, and (h)1.252734, respectively, as shown in Figures 5.3(a)-(h). The electric fields of the modes are symmetrically distributed since the fully ethanol-filled PBF still has the symmetrical RI distribution. The maximum effective RI difference between the core mode and cladding mode reaches $1.02\times10^{-1}$.

Figure 5.4 (a) shows the cross section view of the simulated partially ethanol-filled PBF with about 1/3 ethanol-filled cladding air holes. It can

support the core LP01 mode and high order LP11, LP12, LP21, LP41, LP22 and LP31-like modes at 1550 nm, with the effective RIs of (b)0.9924907, (c)0.9839447, (d)0.9430347, (e)0.9300968, (f)0.9291467, (g)0.9092067 and (h)0.897042, respectively, as shown in Figures 5.4(b)-(h). As can be seen, due to its asymmetric RI distribution structure, the electric field distributions of the core mode and other high order cladding modes also become asymmetric. This shows the strong polarization dependent properties of the partially filled PBF. The maximum effective RI difference between the core mode and high order mode reaches about $9.5\times10^{-2}$.

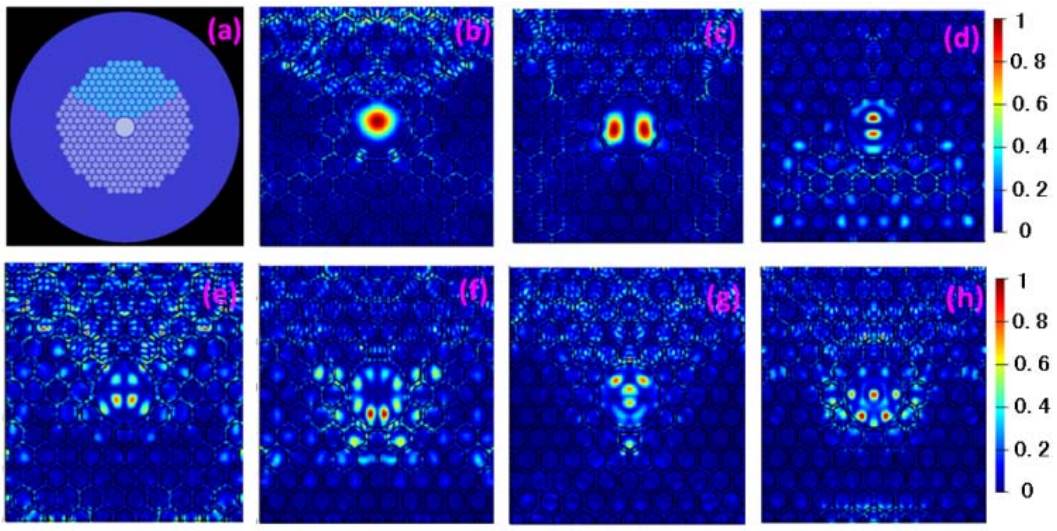


Figure 5.4 (a) Cross section of the simulated partially ethanol-filled PBF and simulated mode patters under effective RIs of (b) 0.9924907, (c)0.9839447, (d)0. 9430347, (e)0.9300968,(f)0.9291467, (g)0.9092067, and (h) 0.897042, respectively

According to the simulated results above, more high order cladding modes can be easily excited if filling the ethanol into the air core and/or air

claddings of the PBF, and the RI difference between the core and cladding modes can be effectively improved.

## 5.4 Principle of Operation

The MMI with an SMF-PBF-SMF structure is shown in Figure 5.5. The ethanol-filled PBF was cut to a short section for constructing the MMI. Note that after cleaving the PBF, it must be hung in the air for 1-2 minutes to get rid

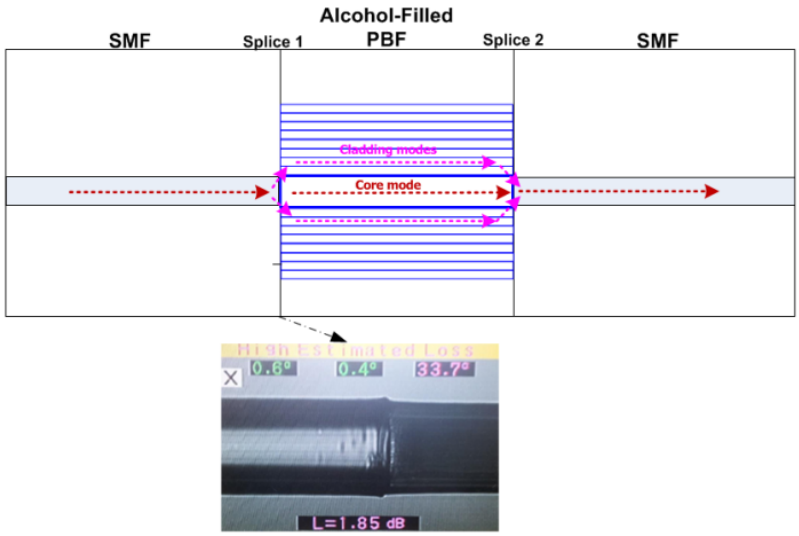


Figure 5.5 Schematic structure of the PBF based MMI (Inset is the photograph of the splice joint between the SMF and PBF)

of the ethanol solution on the surface of the cross section. A commercial Fujikura FSM-40PM splicer was used to construct the interferometer. To avoid the air hole collapse, a re-arc splice method was used with the splicing parameters of an arc current of 10.5 mA, arc time of 300 ms, and an offset position of R-90 μm. The inset in Figure 5.5 shows the photograph of the splice joint between the SMF and PBF. When the light of the fundamental

mode propagates to the splice joint 1, the high order cladding modes are excited due to the MFD mismatch between the SMF and PBF. After they propagate to the second splice joint, they re-couple with the core mode and construct intermodal interferences, and the phase difference between the core mode and *m*-th cladding mode can be given by

$$\varphi = \frac{2\pi (n_{co} - n_{cl}^{m})L}{\lambda}, \tag{5.1}$$

where $n_{co}$ and $n_{cl}^{m}$ are the effective RIs of the core and *m*-th cladding modes, respectively, and $L$ is the length of the ethanol-filled PBF. As the phase satisfies the conditions of $\varphi = 2k\pi$ and $(2k+1)\pi$, where $k$ is the interference order, the peak and dip resonance wavelengths occur. The FSR of the transmission spectrum can be given by

$$FSR = \frac{\lambda_1 \lambda_2}{(n_{co} - n_{cl}^{m})L}, \tag{5.2}$$

where $\lambda_1$ and $\lambda_2$ are the wavelengths corresponding to two adjacent intensity maxima or minima. The peak and dip resonance wavelengths of $\lambda_p$ and $\lambda_d$ could be obtained as

$$\lambda_p = \frac{1}{k}(n_{co} - n_{cl}^{m})L, \tag{5.3}$$

$$\lambda_d = \frac{1}{2k+1}(n_{co} - n_{cl}^{m})L. \tag{5.4}$$

Since the core and cladding modes propagate in different waveguide structures

of the ethanol-filled PBF, the temperature variation affects the two modes in different manners. We denote the thermo-optic coefficients by $\xi_{co}$ and $\xi_{cl}$ for the core and cladding modes, respectively. The temperature induced effective RI variation can be given by

$$\Delta(n_{co} - n_{cl}^{m}) = (\xi_{co} n_{co} - \xi_{cl} n_{cl}^{m})\Delta T \,. \tag{5.5}$$

and the temperature induced length variation of the MMI can be given by

$$\Delta L = \alpha L \Delta T \,, \tag{5.6}$$

where $\alpha$ is the thermal-expansion coefficient of the MMI. Hence, the peak or dip wavelength shift $\Delta\lambda_{d,p}$ of the MMI due to the temperature variation can be obtained as

$$\frac{\Delta\lambda_{d,p}}{\lambda_{d,p}} = (\alpha + \xi)\Delta T \quad , \tag{5.7}$$

where $\xi = \dfrac{\xi_{co} n_{co} - \xi_{cl} n_{cl}^{m}}{n_{co} - n_{cl}^{m}}$, is a constant that describes the thermal-induced variation of the effective RI difference of the two interference modes.

# 5.5 Experimental Results and Discussions

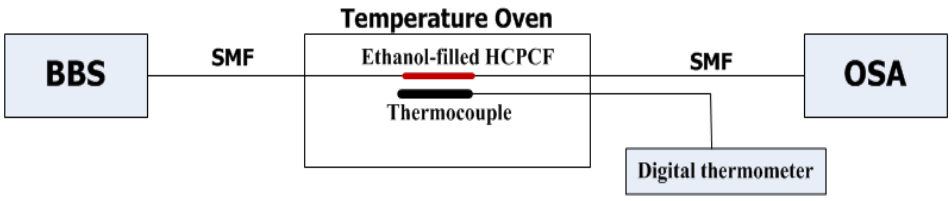


Figure 5.6 Schematic diagram of the experimental setup

Figure 5.6 shows the schematic diagram of the experimental setup. A C and L

BBS was used as the light source. The transmission spectrum of the MMI was captured by an ADVAVTEST Q8384 OSA with a resolution of 0.05 nm. The temperature was calibrated by a digital thermometer based on a silicon semiconductor thermocouple under a resolution of 0.1 C°. To avoid the bending effect, the MMI was held on a U-groove slab in a temperature oven.

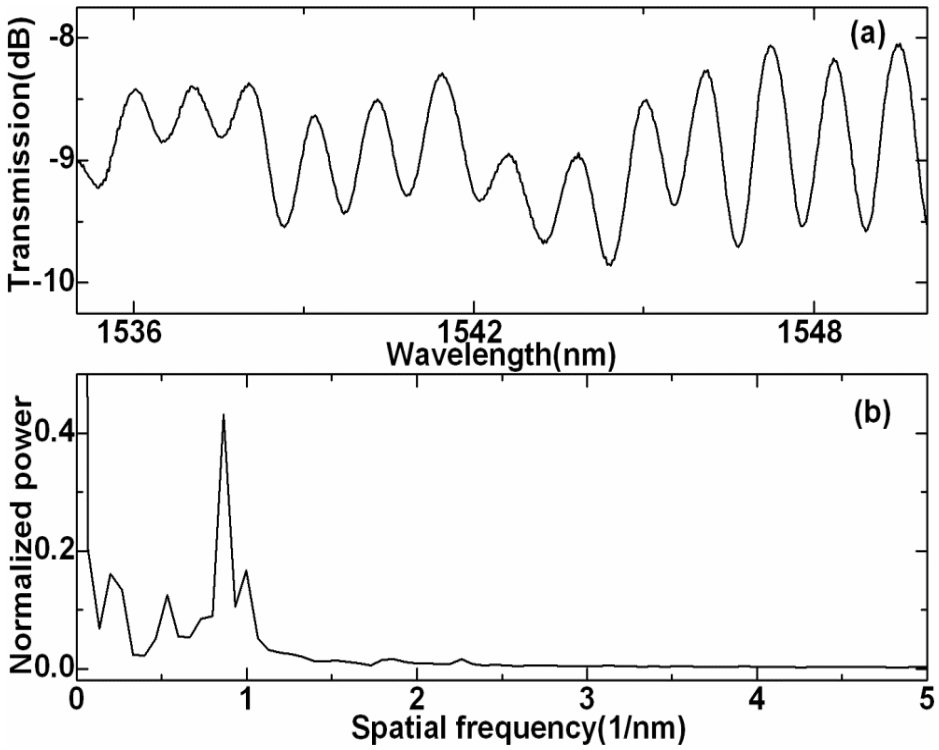


Figure 5.7 (a) Transmission spectrum of the fully ethanol-filled PBF MMI and (b) its corresponding spatial frequency spectrum

Figure 5.7 (a) shows the typical transmission spectrum of a ~1.9-cm fully ethanol-filled PBF based MMI. To determine the number and power distribution of the interference modes, the wavelength spectrum in Figure 5.7 (a) was Fourier transformed to obtain the spatial frequency of the interference

fringes, as shown in Figure 5.7 (b). It can be seen that a distinct dominant cladding mode is excited, and there are also the other three weak cladding modes. Since the FSR of the transmission spectrum has almost the same value about 1.12 nm, the interference is mainly constructed by the core mode and one dominated cladding mode, and the other weak cladding modes have a modulation function on the interference spectrum, which leads to the non-uniform spectrum of the MMI. According to Eq.5.2, we can get the effective RI difference between the two interference modes of about 0.1. Based on the previously simulated results in Figure 5.3, the two interference modes should be the LP01 and LP42-like modes.

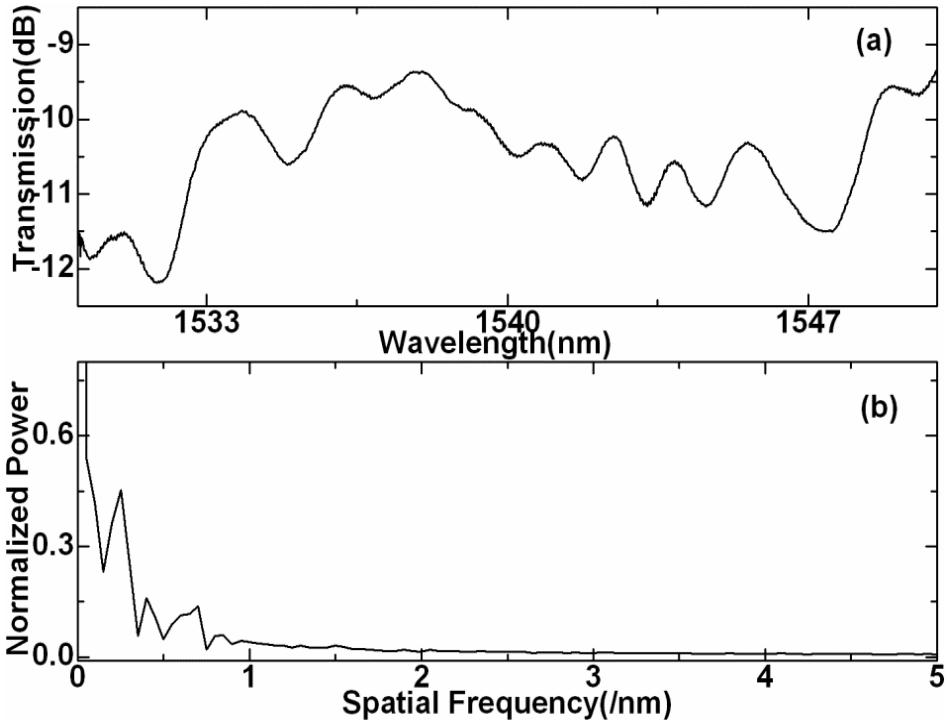


Figure 5.8 (a) Transmission spectrum of the partially ethanol-filled MMI and (b) its corresponding spatial frequency spectrum

Figure 5.8 shows the typical transmission spectrum of a ~1.6-cm partially ethanol-filled PBF MMI and its corresponding spatial frequency spectrum. As can be seen, more than three cladding modes are excited. The transmission spectrum has two main FSRs of ~2.82 nm and ~1.3 nm. Hence, at least two dominated cladding modes contribute to the interference with the core mode, which lead to the seriously non-uniform of the interference pattern, as shown in Figure 5.8 (a). According to Eq.5.2, we can get two effective RI difference values between the core and cladding modes of about 0.05 and 0.1. Based on the previously simulated results in Figure 5.4, the two interference cladding modes may be the LP12 and LP31-like modes.

With the increase of the temperature, the transmission spectrum of the fully ethanol-filled PBF MMI experiences a distinct blue shift, as shown in Figure 5.9. Since it has a narrow FSR, to distinguish the wavelength shift induced by the temperature variation, we marked every two adjacent transmission spectra each time. Figure 5.10 shows the measured relationship between the temperature and wavelength shift. For the two initial monitored peaks at the wavelengths of 1549.5 nm and 1547.24 nm, both show good linear responses to temperature within the range of 25.6-50 C° with linear R-squares of 0.991 and 0.9927, respectively, and their thermal sensitivities reach -292 and -290 pm/C°. The sensitivity of the fully ethanol-filled PBF based MMI is 41.1 and 43.8 times bigger than those of the unfilled PBF based MMIs in Refs. [93] and [36]. According to Eq.5.7, the fully ethanol-filled PBF

based MMI has the higher value of $(\alpha+\xi)$, its value reaches -1.9×10$^{-4}$/°C while those of the unfilled PBF based interferometer are only about -4.6×10$^{-6}$/°C and 4.3×10$^{-6}$/°C.

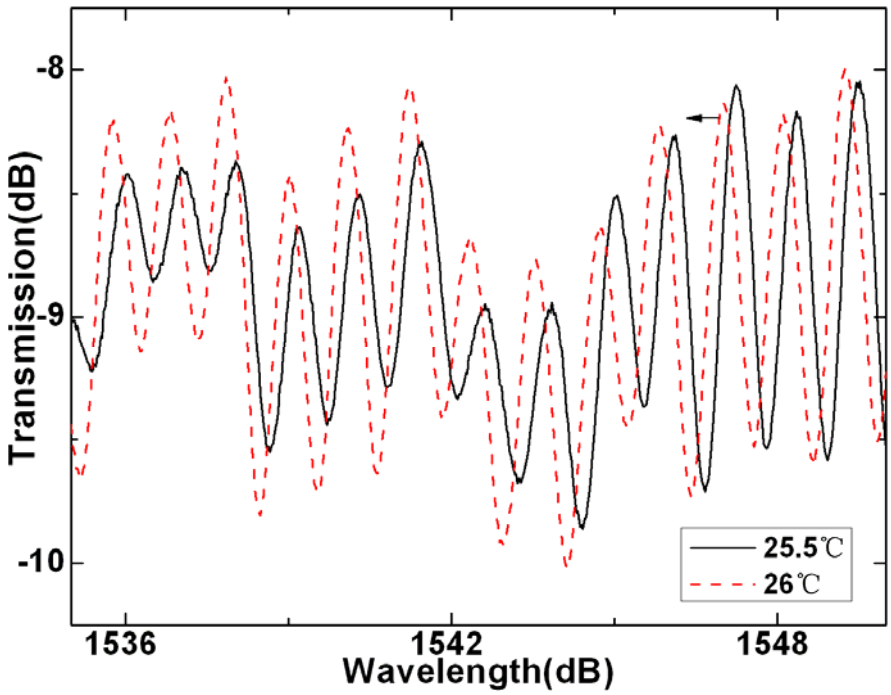


Figure 5.9 Transmission spectral responses to the temperature for the fully ethanol-filled PBF based MMI

Figure 5.11 shows the transmission spectral response to the temperature for the partially ethanol-filled PBF based MMI. Its transmission spectrum also experiences a distinct blue shift with the increase of the temperature. Fortunately, its interference pattern exists relatively bigger FSRs, by monitoring the resonance dips located within the bigger FSR, its wavelength shift can be continuously monitored.

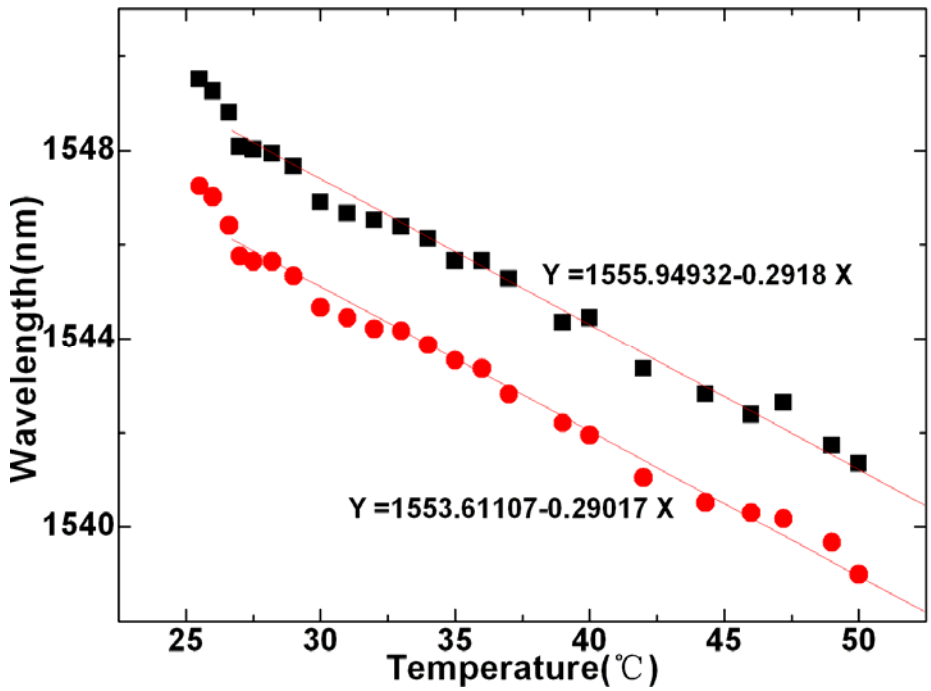


Figure 5.10 Temperature variation against wavelength shift for the fully ethanol-filled PBF based MMI

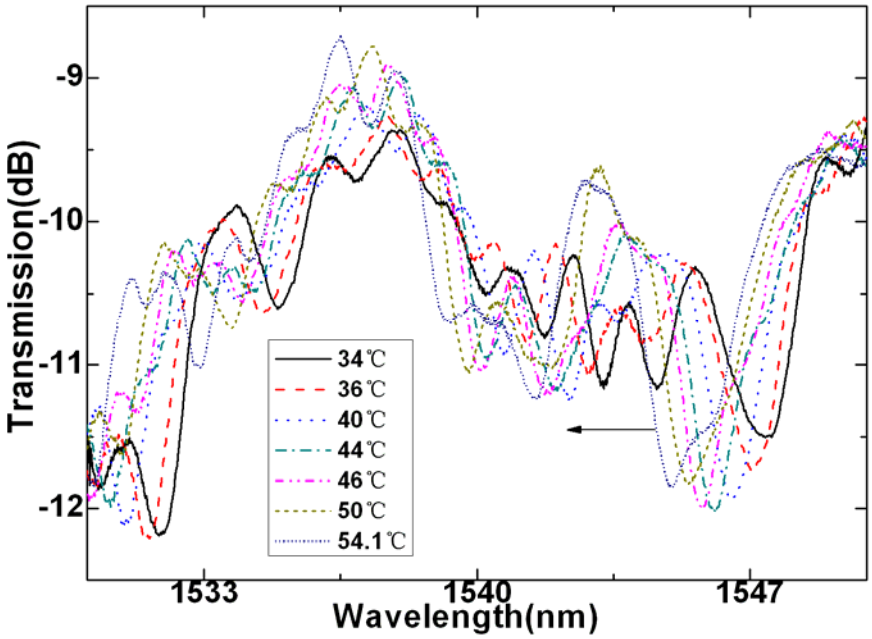


Figure 5.11 Transmission spectral responses to the temperature of the partially ethanol-filled PBF based MMI

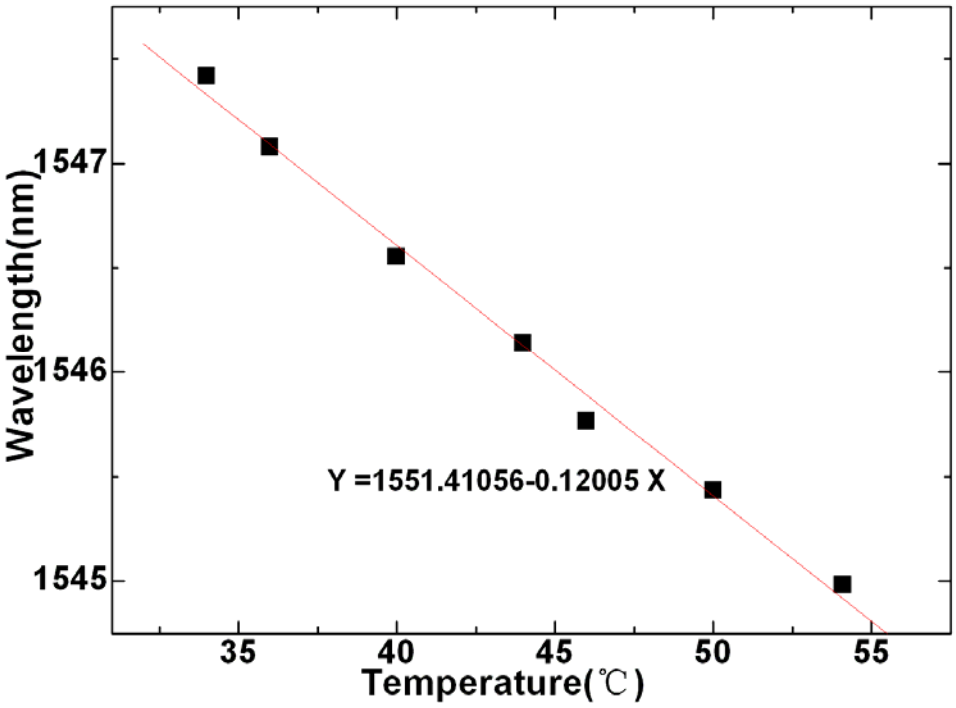


Figure 5.12 Wavelength versus temperature of the partially ethanol-filled PBF based MMI

Figure 5.12 shows the measured relationship between the temperature and wavelength shift. For the monitored initial resonance dip at 1547.46 nm, the wavelength shift shows a linear response to temperature with a linear R-square of 0.992, and its sensitivity reaches -120 pm/C°. Its sensitivity is 16.9 and 18 times bigger than those of the unfilled PBF MMIs in Refs. [93] and [36]. According to Eq.5.7, the partially ethanol-filled PBF MMI has the $(\alpha+\xi)$ value of -7.8×10$^{-5}$/°C. Based on the above experimental results, as can be seen, the thermal sensitivity of the PBF based MMI can be adjusted by selectively filling the air core and/or claddings of the PBF with ethanol solution since the $\xi$ can be changed accordingly due to the effective RI

change of the high order interference modes.

## 5.6 Conclusions

In conclusion, the light guidance characteristics of the fully and partially ethanol-filled PBFs and their applications as MMIs for temperature sensing have been investigated theoretically and experimentally. The ethanol-filled PBFs are much easier to excite more high order cladding modes for constructing the MMIs without using the other special splicing techniques, and the effective RI difference between the interference modes can reach 26.6 times bigger than that of the ethanol-filled solid core PCF. Moreover, the thermal sensitivity of the PBF based MMI could be effectively improved and adjusted by selectively filling the air core and/or air claddings of the PBF with ethanol. Since they have exhibited the inherent advantages of low cost, small size, compact structure, easy fabrication, and high thermal sensitivity, they are expected to have potential applications in thermal sensing.

# Chapter 6

# Conclusions and Future Work

## 6.1 Conclusions

In this thesis, four types of MMIs based on dual SMF down-tapers, dual SMF up-tapers, dual EYPF down-tapers, and ethanol-filled PBF have been proposed and investigated. The novelties of this thesis are summarized as follows:

1. A high ER SMF based down-taper MMI fabricated by arc-discharging method is proposed. It is highly sensitive to temperature but has a limited sensitivity to RI. By serious connecting it to an FBG, dual parameters (temperature and RI) measurement with better measurement resolutions can be achieved.
2. A novel high ER SMF based DCMs MMI is proposed. It is fabricated automatically by a commercial fiber splicer. This type of MMI can be

used for dual parameters (strain and temperature), micro-displacement and ultrasound measurements with high performances.

3. The particular thermal characteristics of the EYPF based MMI are found theoretically and experimentally. Without an additional pump, it can be used as a high sensitivity temperature sensor. However, once the additional pump is introduced, its thermal sensitivity is reduced. This shows that with an additional pump, its thermal sensitivity can be adjusted and its stability can be improved.
4. The fully and partially ethanol-filled PBF based MMIs are proposed. This type of device can be used as a high thermal sensitivity sensor. Moreover, its thermal sensitivity can be adjusted by selectively filling the air core and/or air claddings of the PBF with ethanol.

The detail achievements in this thesis are summarized as follows:

Firstly, a high ER SMF based down-taper MMI has been proposed and demonstrated. With the arc discharge method, it could be fabricated by using the optimized splicing parameters of a commercial splicer and a simple mechanical taper setup. The MMI with about 24-dB ER could be achieved if fabricating two adjacent fiber down-tapers with 20-μm waist diameter on one same SMF. It is highly sensitive to temperature while its RI sensitivity is limited since the propagation position of cladding mode is more close to that of the core mode in the MMI. Its thermal sensitivity is -72.8 pm/°C while its RI sensitivity is 10.299 nm/RIU. If serially connecting it to an FBG,

simultaneous measurement of temperature and strain could be realized by building a dual parameter measurement matrix. Its temperature and RI resolutions reach ±1.1°C and ± 0.009, and they are bigger than those of the other measurement method. Due to its high ER, it can be used as a quasi-liner filter for low cost intensity-referenced sensors. It has exhibited the advantages of simple and compact structure, high ER, small size, low cost, and easy fabrication. It has potential to have more applications as fiber filters and fiber sensors.

Secondly, a novel DCMs fiber up-taper MMI, with a high ER and good fabrication reproducibility, has been proposed and demonstrated. It is almost like an LPG-type device, also with a deep resonance dip within C and L bands. It could be fabricated automatically by setting an enlarged "overlap" parameter of a commercial splicer. The ER of this MMI can reach 27.7 dB. As a fiber sensor, it could be used for temperature, strain, RI, micro-displacement, ultrasound, and dual-parameters (strain and temperature) measurements. Its sensing performances are summarized as follows:

1. The MMIs with the 2-cm and 1-cm lengths have almost the same temperature and strain sensitivities for the deep resonance dip, and the thermal sensitivity reaches around 57.5 pm/ C while its strain sensitivity is around -1.02 pm/με.
2. The DCMs MMI has one deep resonance dip and the other shallow one. This is helpful to improve the dual parameter measurement

resolutions for the wavelength-referenced method. Based on a wavelength-referenced method, simultaneous measurement of the temperature and strain, with the measurement resolutions of ±1.1 C° and ±54.4 με, could be achieved by monitoring the two resonance dips in wavelength shift responses to temperature and strain. However, the wavelength-reference method cannot discriminate the thermal and strain sensitivity difference of the two cladding modes.

3. With the MDM method, the two cladding modes could be discriminated in spatial frequency domain. Simultaneous measurement of temperature and strain could be achieved by monitoring two spatial frequencies in normalized power variations to strain and temperature. The measurement resolutions reach ±0.05 C° and ±3.14 με, and are much higher than those of the other proposed dual parameters (temperature and strain) measurement solutions.
4. As the RI sensor, its deep resonance dip shows a lower RI sensitivity of about -16.448 nm/RIU while the other shallow resonance dip has a high RI sensitivity of about -62.89 nm/RIU, and 3.8 times higher than that of the deep resonance dip. This is due to the modulation function of the other high order cladding mode.
5. By embedding the DCMs MMI into a CCFC based beam, it could be used as an intensity-modulated micro-displacement sensor with a high sensitivity. Experimental results show that its measurement resolution

reaches 4.67 μm, and its dynamic measurement range is within 0~200 Hz. Its temperature cross-sensitivity issue can be solved by applying a corresponding pre-displacement since it has opposite ER variation trends in responses to displacement and temperature, and a 2.5-μm pre-displacement can compensate 1-C° temperature variation.

6. The DCMs MMI could be used as an intensity-modulated FAS with an ultrahigh sensitivity. This is due to to its high ER and simultaneous responses to the acoustic pressure in wavelength shift and intermodal power coupling change. Its sensitivity reaches about 2.65 V/ μPa and is 33.5 times larger than that of the PZT acoustic sensor. Its temperature-cross issue can be solved by applying a corresponding pre-strain since it has opposite wavelength shift trends in response to strain and temperature.

In addition, compared to the fiber down-taper MMI, this type of MMI is more robust since the fiber down-taper MMI is more fragile. Since the fabrication of this MMI only involves cleaving and splicing with a low cost standard SMF, it can be easily fabricated and integrated with the other fiber components. Moreover, as fiber sensors, the miniaturized and compact size, linearity and high sensitivity would enable this type of MMIs to have wide applications in fiber filters and fiber sensors.

Thirdly, the intensity and wavelength dependent thermal characteristics of the EYPF down-taper MMI have been investigated. Without the additional

optical pump, it could be used as a high sensitivity temperature sensor, with two resonance dips within the short and long wavelength ranges having thermal sensitivities of -33.8 and -35.2 pm/°, respectively. After introducing into the additional optical pump, their thermal sensitivities are reduced to -30.7 and -24.9 pm/°C, and thermal sensitivities of 3.1 pm/°C and 10.3 pm/°C are reduced. This suggests that an additional optical pump can be used to control its thermal sensitivity and improve its stability.

Fourthly, the fully and partially ethanol-filled PBF based MMIs have been proposed and demonstrated. The fully and partially ethanol-filled PBFs could support more high order cladding modes. The effective RI differences between the core mode and higher order cladding mode could be improved to $1.02\times10^{-1}$ and $9.5\times10^{-2}$ for the fully and partially ethanol-filled PBFs, and 26.6 and 24.8 times bigger than that of the ethanol-filled solid core PCF. The ethanol-filled PBF based MMIs could be constructed by splicing a short section of the fully or partially ethanol-filled PBF between the SMFs without using the other special splicing techniques. Experimental results show that the thermal sensitivities of the fully and partially ethanol-filled PBF based MMIs reach -292 pm/°C and -120 pm/°C, respectively, and are 43.8 and 18 times bigger than that of the unfilled PBF based MMIs. This suggests that the thermal sensitivity of the PBF based MMI can be effectively improved and adjusted by selectively filling the air core and/or air claddings of the PBF with ethanol.

As can be seen, the proposed four types of MMIs have their own advantages and limitations. The high ER SMF based down-taper MMI is a good candidate as a high-sensitivity temperature sensor but it has a limited RI sensitivity when it is used as an RI sensor. The DCMs MMI is a good candidate for dual parameters (temperature and strain), micro-displacement, and acoustic pressure measurements but it has a limited RI sensitivity when it is used as an RI sensor. Compared to the fragile thin-taper MMI, the robust up-taper MMI is more suitable for industry application. The EYPF down-taper MMI has the specific thermal characteristics. It can be used as a high sensitivity temperature sensor. However, once introducing an additional optical pump, its thermal sensitivity is reduced. Hence, its stability can be improved by introducing an additional pump when it is used as a fiber filter. The ethanol-filled PBF based MMI is a good candidate as a high-sensitivity temperature sensor. Moreover, its thermal sensitivity can be adjusted by selectively filling the air core and/or air claddings of the PBF with ethanol. However, the fabrication of such PBF based devices is complicated.

## 6.2 Future Work

Compared to the common MZI, MCI and SI, the MMIs have attracted much attention due to their inherent advantages of simple and compact structure, low cost, small size and easy fabrication, especially, they have wide applications in fiber filters and fiber sensors. For the proposed four types of MMIs, the high

ER down-taper MMI has potential to be packaged as a practical temperature sensor with high performance. The high ER DCMs up-taper MMI shows its higher performance in dual parameters, micro-displacement and ultrasound measurements, and it will have great impact on the future measurement industry. The EYPF based MMI shows its particular thermal characteristics. With an additional optical pump, its thermal sensitivity can be adjusted and its stability can be improved. This will give us much inspiration in active fiber thermal sensor development and reliable active fiber filter design. The ethanol-filled PBF based MMI shows its wide thermal sensitivity adjustability. This provides us a new solution in fiber thermal sensor development. Based on the proposed four types of MMIs in this thesis, some recommendations for future research work are proposed as follows:

Firstly, for the SMF based down-taper MMI, there are two recommendations for the future work. Firstly, when it is used for RI measurement, the temperature-cross issue has to be considered. Although this issue can be solved by serially connecting an FBG as a temperature reference, but the MMI-FBG structure has a large footprint. This limits its practical applications. The good solution is only using one MMI to realize simultaneous temperature and RI measurement. This can be achieved by adopting the MMI with two resonance dips. Moreover, to obtain high measurement resolutions, the two resonance dips should have a big power difference since the resonance dips, with the same power levels, have almost the same temperature and RI

sensitivities, which leads to the lower measurement resolutions. Secondly, the waist diameter of the dual fiber down-tapers is around 20 μm, hence it should have a high sensitivity to vibration, but to use it as a vibration or sensor, it has to be packaged reliably since it is fragile and easily influenced by outer disturbance.

Secondly, for the DCMs fiber up-taper MMI, it is more robust than the fiber down-taper MMI. Hence, it is more suitable for practical applications. There are also two recommendations: firstly, when it is used as an FAS, it has shown the ultrahigh sensitivity. But for practical applications, it has to be packaged reliably to eliminate the temperature influence. Hence, a mechanical pre-strain structure needs to be designed to realize the temperature compensation. Secondly, based on its sensing performance to RI, the two resonance dips show big RI sensitivities, and they have thermal sensitivity difference. Hence, it has potential to realize simultaneous measurement of temperature and RI.

Thirdly, for the EYPF based MMI, since this MMI contains the Er-Yb materials, this device should have response to outer magnetic field. Hence, it can be used as a fiber magnetic sensor. Moreover, under the magnetic field, if an additional optical power is introduced, the thermal characteristics of the MMI become more complicated.

Fourthly, for the ethanol-filled PBF based MMIs, there are two recommendations. Firstly, in this study, just the ethanol is filled into the PBF

to construct MMIs for temperature sensing. If the other material, such as the magnetic material, is filled into the PBF to construct the MMI, the light propagating along the PBF can be modulated by an external magnetic field. Secondly, the partially ethanol-filled PBF shows the strong polarization dependent characteristics, it can be developed as a PBF based polarizer.

Fifthly, the sensing signal interrogation for the MMI sensors is very important, which determines the performance of the sensor system. In this thesis, the DCMs MMI can be designed as low-cost intensity-modulated micro-displacement sensor and FAS with high sensitivities, but the other wavelength-referenced sensors are with a high cost. For practical applications, they have to be developed as low cost wavelength-modulated or intensity modulated sensors.

# List of Publications

## Journal papers


1. **B. Dong**, N. Chen, G. Cheng, C. Yu, and Y. Gong, "Optical pump induced thermal sensitivity reduction in a minimized Er/Yb-codoped-fiber Mach–Zehnder interferometer," *IEEE/OSA Journal of Lightwave Technology*, vol. 32, no. 5, pp. 917-921, 2014
2. **B.Dong**, B.Zhang, J.Ng,Y.Wang, and C.Yu, "Ultrahigh-sensitivity fiber acoustic sensor with a dual cladding modes fiber up-taper interferometer," *IEEE Photonics Technology Letters*, vol.27, pp.2234 – 2237,2015
3. **B.Dong**, Y.Ge, Y.Wang, C. Yu, "High extinction-ratio dual thin-taper fiber interferometer fabricated by arc-discharge and its performance as sensors," *Optics Communications*, vol.355, pp.225-229, 2015
4. Y.Yu, **B.Dong**, and C.Yu, "Optical signal to noise ratio monitoring using Sagnac interferometer based on fiber birefringence," *IEEE Photonics Technology Letters*, vol.27,pp.1899 -1902,2015.
5. **B.Dong**,Y.Peng,Y.Wang, C. Yu, "Mode division multiplexing in a fiber modal interferometer for dual parameters measurement," *IEEE Photonics Technology Letters*, 2015 (Accepted)
6. **B.Dong**, C.Yu, Y.Wang, "Intensity-modulated micro-displacement sensor with an embedded fiber dual cladding modes interferometer", *Sensors and*

*Actuators A*, 2015 (Accepted)

7. **B.Dong**, Z.Shen, C.Yu, Y.Wang, "Modal excitations in fully and partially ethanol-filled photonic bandgap fibers and their applications as fiber sensors," submitted to *IEEE/OSA Journal of Lightwave Technology*, 2015(Pending Acceptance)

# Conference Papers

1. **B.Dong**, "Miniaturized fiber interferometers and their applications as fiber sensors," *PIERS Proceedings*, pp. 353-356, Aug 2014 (Invited Talk)
2. **B.Dong**, C.Yu, and Y.Wang, "Thermal characteristics of the ethanol-filled hollow-core photonic-crystal-fiber modal interferometer," *ICOCN 2015* (Invited Talk)

# References

[1] J.S Sirkis, D.D Brennan, M.A. Putman, T.A Berkoff, A.D. Kersey, E.J. Friebele, "In-line fiber étalon for strain measurement," *Opt. Lett*.vol.18, pp. 1973–1975,1993.

[2] J. Sirkis, T.A. Berkoff, R.T. Jones, H. Singh, A.D. Kersey, E.J. Friebele, M.A Putnam, "In-line fiber etalon (ILFE) fiber-optic strain sensors," *J. Lightw. Technol*. vol.13, pp.1256–1263,1995.

[3] H. Singh, J.S. Sirkis, "Simultaneously measuring temperature and strain using optical fiber microcavities.," J. *Lightw. Technol*. vol.15,pp. 647–653,1997.

[4] Y.J. Rao, T. Zhu, X.C. Yang, D.W. Duan, "In-line fiber-optic etalon formed by hollow-core photonic crystal fiber," *Opt. Lett*. vol.32, pp.2662–2664,2007.

[5] Q. Shi, F. Lv, Z. Wang, L. Jin, J. Hu, Z. Liu, G. Kai, X. Dong, "Environmentally stable Fabry–Pérot-type strain sensor based on hollow-core photonic bandgap fiber, " *IEEE Photon. Technol. Lett*. vol.20, pp.237–239,2008.

[6] D.W Duan, Y.J Rao, L.C. Xu, T. Zhu, M. Deng,D. Wu, J. Yao, "In-fiber Fabry-Perot and Mach-Zehnder interferometers based on hollow optical fiber fabricated by arc fusion splicing with small lateral offsets," *Opt. Commun*.vol.284, pp.5311–5314, 2011.

[7] C.L Lee, L.H. Lee, H.E. Hwang, J.M. Hsu, "Highly sensitive air-gap fiber Fabry-Perot interferometers based on polymer-filled hollow core fibers," *IEEE Photon. Technol. Lett*. vol.24, pp.149–151,2012.

[8] H.Y. Choi, G. Mudhana,K.S. Park, U.C. Paek, B.H. Lee, "Cross-talk free and ultra-compact fiber optic sensor for simultaneous measurement of

temperature and refractive index," *Opt. Express*, vol.18, pp.141–149, 2010.

[9] M. Deng, C.P Tang,T. Zhu, Y.J. Rao,L.C. Xu, M. Han, "Refractive index measurement using photonic crystal fiber-based Fabry-Perot interferometer," *Appl. Opt.*, vol.49, pp.1593–1598,2010.

[10] H. Porte, V. Gorel, S. Kiryenko, J.-P. Goedgebuer,W. Daniau, P. Blind, "Imbalanced Mach-Zehnder interferometer integrated in micromachined silicon substrate for pressure sensor," *J. Lightw. Technol*. vol.7, pp. 229–233,1999.

[11] R. Kashyap, B. Nayar, "An all single-mode fiber Michelson interferometer sensor," *J. Lightw. Technol.* vol.1, pp.619–624,1983.

[12] Y. Liu, B. Liu, X. Feng, W. Zhang, G. Zhou, S. Yuan, G. Kai, andX. Dong, "High-birefringence fiber loop mirrors and their applications as sensors," *Appl. Opt*. vol.44, pp.2382–2390 ,2005.

[13] B.Dong and D-P. Zhou, "Space division multiplexing high birefringence fiber loop mirrors to realize discriminative measurement of temperature and strain," *Appl. Opt*.vol.48,no.20,pp. 3994-3997, 2009.

[14] H.Y. Fu, H.Y. Tam,L.Y. Shao,X. Dong, P.K.A. Wai, C. Lu, S.K. Khijwania, "Pressure sensor realized with polarization-maintaining photonic crystal fiber-based Sagnac interferometer," *Appl. Opt*.,vol.47, pp.2835–2839. 2008

[15] D.S. Moon, B.H. Kim, A. Lin, G. Sun, T.G. Han, W.T. Han, Y. Chung, "The temperature sensitivity of Sagnac loop interferometer based on polarization maintaining side-hole fiber," *Opt. Express*. vol.15, pp.7962–7967,2007

[16] L.V. Nguyen,D. Hwang, S. Moon, D.S. Moon,Y. Chung, "High temperature fiber sensor with high sensitivity based on core diameter mismatch," *Opt. Express*. vol.16, pp.11369–11375,2008.

[17] F. Pang, H. Liu, H. Guo, Y. Liu, X. Zeng, N. Chen, Z. Chen, T. Wang, "In-fiber Mach-Zehnder interferometer based on double cladding fibers for refractive index sensor," *IEEE Sens. J*. vol.11, pp.2395–2400, 2011.

[18] J.J. Zhu, A.P. Zhang, T.H. Xia, S.L. He, W. Xue, "Fiber-optic high-temperature sensor based on thin -core fiber modal interferometer," *IEEE Sens. J.* vol.10, pp.1415–1418, 2010,

[19] O. Frazao, S.F.O. Silva, J. Viegas, J.M. Baptista, J.L. SantosKobelke, K. Schuster, "All fiber Mach-Zehnder interferometer based on suspended twin-core fiber," *IEEE Photon. Technol. Lett.* vol. 22, pp.1300–1302, 2010.

[20] L. Yuan, J. Yang, Z. Liu, "A compact fiber-optic flow velocity sensor based on a twin-core fiber Michelson interferometer," *IEEE Sens. J*.vol. 8, pp.1114–1117, 2008.

[21] B.Y Li,L. Jiang, S.M. Wang, L.Y. Zhou, H. Xiao, H.L. Tsai, "Ultra-abrupt tapered fiber Mach-Zehnder interferometer sensors.," *Sensors*,vol.11, pp.5729–5739, 2011.

[22] Z.B. Tian, S.S.H. Yam, "In-line abrupt taper optical fiber Mach-Zehnder interferometric strain sensor," *IEEE Photon. Technol. Lett*.vol. 21, pp.161–163, 2009.

[23] Z.B. Tian, S.S.H. Yam,J. Barnes, W. Bock,P. Greig, J.M. Fraser, H.P. Loock, R.D. Oleschuk, "Refractive index sensing with Mach-Zehnder interferometer based on concatenating two single mode fiber tapers," *IEEE Photonics Technol. Lett.* vol.20, pp.626–628, 2008.

[24] P. Lu, L. Men, K. Sooley, K.,Q.Chen, "Tapered fiber Mach-Zehnder interferometer for simultaneous measurement of refractive index and temperature," *Appl. Phys. Lett*.vol.94, pp.131110:1–131110:4,2009

[25] N.-K. Chen, Y.-H. Hsieh, and Y.-K. Lee, "Tapered fiber Mach–Zehnder interferometers for vibration and elasticity sensing applications," *Opt.Express* vol.21,pp.11209–11214,2013.

[26] N-K. Chen, and Z-Z. Feng, "Effect of gain-dependent phase shift for tunable abrupt-tapered Mach–Zehnder interferometers," *Opt. Lett*, vol. 35, no. 12 , pp.2109-2111,2010.

[27] J. An,Y. Jin,M. Sun,X.Dong, "Relative Humidity Sensor Based on SMS Fiber Structure With Two Waist-Enlarged Tapers," *IEEE Sens. J*. vol.14, pp.2683-2686,2012.

[28] K. Ni, X. Dong, C. C. Chan, T. Li, L. Hu, and W. Qian, "Miniature refractometer based on Mach–Zehnder interferometer with waist-enlarged fusion bitaper," *Opt. Commun* . vol.292,pp.84–86,2013.

[29] D.Wu, T. Zhu, K.-S. Chiang, M. Deng, "All single-mode fiber Mach-Zehnder interferometer based on two peanut-shape structures," *IEEE J. Lightw. Technol*. vol.30, pp.805–810,2012.

[30] H.Gong,X.Yang. K. Ni, C-L. Zhao,and X. Dong, "An optical fiber curvature sensor based on two peanut-shape structures modal interferometer," *IEEE Photon. Technol. Lett* .vol.26,pp.22-24,2014.

[31] Z.B Tian, S.S.H. Yam,H.P. Loock, "Single mode fiber refractive index sensor based on core-offset attenuators," *IEEE Photon. Technol. Lett*. vol.20, pp. 1387–1389, 2008

[32] D.W. Duan, Y.J. Rao, L.C. Xu, T. Zhu, D. Wu, J. Yao, "In-fiber Mach-Zehnder interferometer formed by large lateral offset fusion splicing for gases refractive index measurement with high sensitivity," *Sens. Actuat. B* .vol.160, pp.1198–1202. 2011.

[33] B. Dong, D.-P. Zhou, L. Wei, W.-K. Liu, J. W. Y. Lit,Temperature and phase-independent lateral force sensor based on a core-offset multimode fiber interferometer, *Opt. Express*, vol.16,pp.19291–19296,2008.

[34] B.Dong, D-P. Zhou, L.Wei,“ Temperature insensitive all fiber compact polarization maintaining photonic crystal fiber based interferometer and its applications in fiber sensors,” *J. Lightw. Technol*., vol. 28, no.7, pp.1011-1015, 2010.

[35] B.Dong, and J. Hao, “Temperature-insensitive and intensity-modulated embedded photonic-crystal-fiber modal interferometer based microdisplacement sensor,” *J. Opt. Soc. Am. B*,.vol. 28, no. 10, pp. 2332-2336,2011.

[36] B.Dong, and E. Hao, “Core-offset hollow core photonic bandgap fiber based inter-modal interferometer for strain and temperature measurements,” *Appl. Opt*. vol. 50, pp. 2949–2957, 2011

[37] T. We,X.W. Lan, H. Xiao, “Fiber inline core–cladding-mode Mach-Zehnder interferometer fabricated by two-point CO2 laser irradiations,” *IEEE Photon. Technol. Lett*.vol. 21,pp. 669–671,2009.

[38] L.J. Zhao, S.M. Wang, H. Xiao, Y.F. Lu, H.L. Tsai, “A high-quality Mach-Zehnder interferometer fiber sensor by femtosecond laser one-step processing,” *Sensors*, vol.11,pp. 54–61,2011.

[39] Y. Wang, M.W. Yang, D.N. Wang, S.J. Liu, P.X. Lu, “Fiber in-line Mach-Zehnder interferometer fabricated by femtosecond laser micromachining for refractive index measurement with high sensitivity,” *J. Opt. Soc. Am. B*, vol.27,pp. 370–374, 2010.

[40] L. Jiang, J. Yang, J.,S. Wang, B. Li, M. Wang, “Fiber Mach-Zehnder interferometer based on micro cavities for high-temperature sensing with high sensitivity,” *Opt. Lett.*vol. 36,pp. 3753–3755, 2011.

[41] J. Villatoro,V.P. Minkovich, V. Pruneri, G. Badenes, “Simple all microstructured optical fiber interferometer built via fusion splicing,” *Opt. Express.* vol.15, pp.1491–1496. 2007.

[42] J. Villatoro, V. Finazzi, G. Badenes, V. Pruneri, “Highly sensitive sensors based on photonic crystal fiber modal interferometers,” *J. Sens.,* pp. 747803:1–747803:11. 2009.

[43] R. Jha, J. Villatoro, G. Badenes, V. Pruneri, “Refractometry based on a photonic crystal fiber interferometer,” *Opt. Lett*.vol.34,pp. 617–619, 2009.

[44] R. Jha, J. Villatoro, G. Badenes, G, “Ultrastable in reflection photonic crystal fiber modal interferometer for accurate refractive index sensing,” *Appl. Phys. Lett*., vol.93,pp. 191106:1–191106:3. 2008.

[45] J. Villatoro, M.P. Kreuzer, R. Jha, V.P. Minkovich, V. Finazzi, G. Badenes, G., V. Pruneri, “Photonic crystal fiber interferometer for chemical vapor detection with high sensitivity,” *Opt. Express*.vol. 17, pp.1447–1453, 2009.

[46] J.N. Wang, J.L. Tang, “Photonic crystal fiber Mach-Zehnder interferometer for refractive index sensing,” *Sensors*, vol.12,pp. 2983–2995, 2012.

[47] Dong B,Zhao Q,Lv F,Guo T,Xue L,Li S,Gu H,“Liquid-level sensor with a high-birefringence-fiber loop mirror,” *Appl. Opt.* vol.45, pp.7767-7771,2006.

[48] B.Dong, J. Hao, C. Liaw, B. Lin, and S. C. Tjin, “Simultaneous strain and temperature measurement using a compact photonic crystal fiber inter-modal interferometer and a fiber Bragg grating, ”*Appl. Opt*. vol.49,pp.6232-6235,2010.

[49] C. Thirstrup, Y. Shi, and B. Palsdottir, “Pump-induced refractive index modulation and dispersions in Er3+-doped fibers,” *J. Lightwave Technol*., vol.14, pp. 732-738, 1996.

[50] H.Garcia, A. M. Johnson,Sudhir Trivedi,"Pump Induced nonlinear refractive index change in Erbium and Ytterbium doped fibers-theory and experiments," *CLEO/QELS* 2001, pp. 351,2001.

[51] Y. O. Barmenkov, A. V. Kir'yanov, and M. V. Andres, "Resonant and thermal changes of refractive index in a heavily doped erbium fiber pumped at wavelength 980nm" *Appl.Phys. Lett*., vol.85, pp. 2466, 2004.

[52] R. A. Betts, T. Tjugiarto, Y. L. Xue, and P. L. Chu, "Nonlinear refractive index in erbium doped optical fiber: theory and experiment," *IEEE J. Quantum Electron*, vol.27, pp.908-913,1991

[53] S. W. James, M. L. Dockney, and R. P. Tatam, "Simultaneous independent temperature and strain measurement using in-fibre Bragg grating sensors," *Electron. Lett.* vol. 32,pp.1133–1134,1996.

[54] X. W. Shu, D. H. Zhao, L. Zhang, and I. Bennion, "Use of dual grating sensors formed by different types of fiber Bragg gratings for simultaneous temperature and strain measurements,"*Appl. Opt*. vol.43, pp.2006–2012, 2004.

[55] H. J. Patrick, G. M. Williams, A. D. Kersey, J. R. Pedrazzani, and A. M. Vengsarkar, "Hybrid fiber Bragg grating/long period fiber grating sensor for strain/temperature discrimination,"*IEEE Photon. Technol. Lett.* vol.8, pp.1223–1225,1996.

[56] D.-P. Zhou, L. Wei, W.-K. Liu, and J. W. Y. Lit, "Simultaneous measurement of strain and temperature based on a fiber Bragg grating combined with a high-birefringence fiber loop mirror," *Opt. Commun*. vol.281, pp.4640–4643,2008.

[57] D.-P. Zhou, L. Wei, W.-K. Liu, Y. Liu, and J. W. Y. Lit, "Simultaneous measurement for strain and temperature using fiber Bragg gratings and multimode fibers," *Appl. Opt*. vol.47, pp.1668–1672, 2008.

[58] O. Frazão, L. M. Marques, S. Santos, J. M. Baptista, and J. L.Santos, "Simultaneous measurement for strain and temperature based on a long period grating combined with a high birefringence fiber loop mirror," *IEEE Photon. Technol. Lett*.vol.18, pp.2407–2409,2006.

[59] O. Frazão, J. L. Santos, and J. M. Baptista, "Strain and temperature discrimination using concatenated high birefringence fiber loop mirrors," *IEEE Photon. Technol. Lett*.vol.19, pp.1260–1262,2007.

[60] O. Frazão, E. Diogo, A. B. Lucas, T. M. R. G. Maria, and B. M.Manuel, "Strain and temperature discrimination using high birefringence erbium-doped fiber loop mirror with high pump power laser," *IEEE Photon. Technol. Lett*. vol.20, pp.1033–1035,2008.

[61] B.Dong,"Polarization maintaining fiber interferometer based on superimposed Mach-Zehnder and Sagnac interferences and its application," Opt. Commun,vol. 291, pp.219-221,2013.

[62] B.Dong, J. Hao, C. Liaw,and Z.Xu, "Cladding-mode-resonance in polarization maintaining photonics crystal fiber based Sagnac interferometer and its application for fiber sensor," *J.Lightwave.Technol*.vol.29,pp.1759-1762, 2011.

[63] B. O. Guan, H. Y. Tam, H. L. W. Chan, C. L. Choy, and M. S.Demokan, "Discrimination between strain and temperature with a single fiber Bragg grating," *Microw. Opt. Technol. Lett*.vol.33,pp. 200–202, 2002.

[64] O. Frazão and J. L. Santos, "Simultaneous measurement of strain and temperature using a Bragg grating structure written in germanosilicate fibres," *J. Opt. A Pure Appl. Opt*.vol.6, pp.553–556, 2004.

[65] E. Chehura, S. W. James, and R. P. Tatam, "Temperature and strain discrimination using a single tilted fibre Bragg grating,"Opt. Commun. vol.275, pp.344–347 ,2007.

[66] B. O. Guan, H. W. Tam, X. M. Tao, and X. Y. Dong, "Simultaneous strain and temperature measurement using a superstructure fiber Bragg grating," *IEEE Photon. Technol. Lett.*vol.12, pp.675–677,2000.

[67] B.Dong, L.Xiao, Y. Gong, Y.Wang, Cross-layerly embedded FBG in carbon fiber composites for self-modulated, intensity referenced and

temperature insensitive microdisplacement measurement, *Sens. Actuators A*,, vol.199,pp.250-253. 2013.

[68] X.Dong,B-O. Guan, S.Yuan, X.Y. Dong,H-Y. Tam,"Strain gradient chirp of uniform fiber Bragg grating without shift of central Bragg wavelength," *Opt. Commun*.vol.202, pp.91–95, 2002.

[69] J.M. Baptista, S.F. Santos, G. Rego, O. Frazao, J.L. Santos, "Micro-displacement or bending measurement using a long period fibre grating in a self-referenced fibre optic intensity sensor," *Opt. Commun*, vol. 260,pp. 8–11,2006.

[70] B. Dong, E.J. Hao, "Temperature-insensitive and intensity-modulated embeddedphotonic-crystal-fiber modal-interferometer-based microdisplacement sensor," *J Opt Soc Am B*. vol.28, pp.2332–2336,2011.

[71] C. Zhong, C. Shen, Y. You, J. Chu, X. Zou, X. Dong, Y. Jin, and J. Wang, "Temperature-insensitive optical fiber two-dimensional micrometric displacement sensor based on an in-line Mach–Zehnder interferometer," *J. Opt. Soc. Am. B*. vol.29, pp.1136–1140,2012.

[72] C. Shen, J. Chu, Y. Lu, D. Chen, C. Zhong, Y. Li, X. Dong, and S. Jin, "High Sensitive Micro-Displacement Sensor Based on M-Z Interferometer by a Bowknot Type Taper," *IEEE Photon. Technol. Lett*. vol.26, pp.62–65,2014.

[73] C.Shen, Y.Wang, J.Chu, Y. Lu, Y.Li, and X. Dong, "Optical fiber axial micro-displacement sensor based on Mach-Zehnder interferometer," *Opt. Express*.vol.22, pp.31984-31992,2014.

[74] Q. Wu, A. M. Hatta, P. Wang, Y. Semenova, and G. Farrell, "Use of a bent single SMS fiber structure for simultaneous measurement of displacement and temperature sensing," *IEEE Photon. Technol. Lett*. vol.23, pp.130–132,2011.

[75] HannahF J., M.J. Hillier, Applied Mechanics, 3rd ed., Longmans, New York, pp.310–312,1995.

[76] J. A. Bucaro, H. D. Dardy, and E. F. Carome, "Optical fiber acoustic sensor," *Appl. Opt*. .vol.16, pp.1761–1762,1977.

[77] J. A. Bucaro, H. D. Dardy, and E. F. Carome, "Fiber-optic hydrophone," *J. Acoust. Soc. Am*. vol.62,pp.1302–1304,1977.

[78] J. H. Cole, R. L. Johnson, and P. G. Bhuta, "Fiber-optic detection of sound," *J. Acoust. Soc. Am*. Vol.62, pp.1136–1138,1977

[79] Y.Li, X. Wang, and X. Bao, "Sensitive acoustic vibration sensor using single-mode fiber tapers," *Appl. Opt*. vol.50, pp.1873-1878,2011.

[80] X. Hong, J. Wu, C. Zuo, F. Liu, H. Guo, and K. Xu, "Dual Michelson interferometers for distributed vibration detection," *Appl. Opt.* vol.50, pp.4333–4338,2011.

[81] S. Hu, B. Dong, K.Yu, J. Zhou, and L. Wang, "A hydrophone based on high birefringence fiber loop mirror," *Proc. SPIE*. vol.7659, pp.76590W,2010

[82] J. L. Rivera, M. P. Sánchez, A. Miridonov, and S. Stepanov, "Adaptive Sagnac interferometer with dynamic population grating in saturable rare-earth-doped fiber," *Opt. Express*. vol.21,pp.4280–4290,2013.

[83] J. Xu, X.Wang, K.L. Cooper, and A. Wang "Miniature all-silica fiber optic pressure and acoustic sensors," *Opt. Lett.* vol.30, pp.3269-3271 2005 .

[84] F.Xu, D. Ren, X. Shi, C.Li, W.Lu, L.Lu, L. Lu, and B.Yu, "High sensitivity Fabry–Perot interfereome- tric pressure sensor based on a nanothick silver diaphragm," *Opt. Lett.* vol.37, pp.133-135,2012

[85] J. Ma, W. Jin, H. L. Ho, and J. Y. Dai, "High-sensitivity fiber-tip pressure sensor with graphene diaphragm", *Opt. Lett.* vol.37, pp.2493–2495,2012.

[86] D. C. Seo, D. J. Yoon, I. B. Kwon, and S. S. Lee, "Sensitivity enhancement of fiber optic FBG sensor for acoustic emission," *Proc. of SPIE*.vol.7294, pp.729415,2009.

[87] B. O. Guan, Y. N. Tan, and H. Y. Tam, "Dual polarization fiber grating laser hydrophone," *Opt. Express*.vol.17, pp.19544–19550 ,2009.

[88] T. Guo, A. C. L. Wong, W-S. Liu, B-O. Guan, C. Lu, and H-Y. Tam, "Beat-frequency adjustable Er3+-doped DBR fiber laser for ultrasound detection," *Opt. Express*.vol.19, pp.2485-2492 ,2011

[89] F. Benabid, F. Couny, J. C. Knight, T. A. Birks, and P. S. J. Russell, "Compact, stable and efficient all-fibre gas cells using hollow-core photonic crystal fibres," *Nature*,vol.434, pp.488–491,2005.

[90] Y. Rao, M. Deng, D. Duan, and T. Zhu, "In-line fiber Fabry–Perotrefractive index tip sensor based on endlessly photonic crystal fiber,"*Sens. Actuators A*, vol. 148, pp. 33–38, 2008

[91] B.Dong, J. Hao,T.Zhang, J. Lim, "High sensitive fiber-optic liquid refractive index tip sensor based on a simple inline hollow glass micro-sphere," *Sens. Actuat. B*, vol.171-172,pp.405-408,2012

[92] D. J. Hu, Y.Wang, J. Lim, T. Zhang, K. B. Milenko,Z. Chen, M. Jiang, G.Wang, F. Luan, P. Shum, Q. Sun, H.Wei,W.Tong, and T. R. Wolin´ski, "Novel Miniaturized Fabry–Perot Refractometer Based on a Simplified Hollow-Core Fiber With a Hollow Silica Sphere Tip," *IEEE Sens. J*., vol.12, no. 5,pp.1239-1244,2012

[93] S. H. Aref, R. Amezcua-Correa, J. P. Carvalho, O. Frazão, P. Caldas, J. L. Santos, F. M. Araújo, H. Latifi, F. Farahi, L. A. Ferreira, and J. C. Knight, "Modal interferometer based on hollow-core photonic crystal fiber for strain and temperature measurement, " *Opt. Express*, vol.17, pp.18669-18675,2009.

[94] H Gong,C.C. Chan CC,Y.F Zhang,W.C. Wong, X.Y. Dong."Miniature refractometer based on modal interference in a hollow core photonic crystal fiber with collapsed splicing," *J Biomed Opt*., vol.16,pp.017004,2011.

[95] W.Qian, CL Zhao, CC Chan, L Hu, T Li, WC Wong, P Zu, X Dong, "Temperature sensing based on ethanol-filled photonic crystal fiber modal interferometer, " *IEEE Sens. J*., vol.12.pp.2593-2597,2012.

[96] X. Y. Dong, H. Y. Tam and P. Shum, "Temperature-insensitive strain sensor with polarization-maintaining photonic crystal fiber based Sagnac interferometer," *Appl. Phys. Lett*. vol.90,pp.151113.2007.

[97] W. Qian, CL Zhao, S He, X.Y. Dong, S Zhang, Z Zhang, S Jin, J Guo, H Wei, "High-sensitivity temperature sensor based on an ethanol-filled photonic crystal fiber loop mirror, " *Opt. Lett*. vol.36.pp.1548-1550,2011.

[98] S. Liu, W. Gao, H. Li, Y. Dong and H. Zhang, "Liquid-filled simplified hollow-core photonic crystal fiber," *Optics Laser Tech*, vol.12, pp.140–144, 2014.